The Dissertation Committee for Bowen Ma
certifies that this is the approved version of the following dissertation:

Thermal Transport and Topological Aspects of Magnons

Committee:

Allan H. MacDonald, Supervisor

Gregory A. Fiete, Co-supervisor

Qian Niu

Jianshi Zhou

Xiaoqin Li

Thermal Transport and Topological Aspects of Magnons

by

Bowen Ma

DISSERTATION

Presented to the Faculty of the Graduate School of

The University of Texas at Austin

in Partial Fulfillment

of the Requirements

for the Degree of

DOCTOR OF PHILOSOPHY

THE UNIVERSITY OF TEXAS AT AUSTIN

August 2021

I pod lichinoy veshchestva besstrastony, vezde ogon' bozhestvennyy gorit.

(Beneath the mask of matter's calm, the fire divine burns on and on.)

— Vladimir Solovyov

Acknowledgments

Throughout my graduate study and the writing of this dissertation, I have received a great deal of support and assistance.

First of all, I would like to express my sincere gratitude to my supervisor Prof. Gregory A. Fiete, whose insightful feedback pushed me to sharpen my thoughts and raise the quality of my work. His pleasant and open demeanor, as well as his exceptional patience and knowledge of current research trends in the field, were invaluable to me during my Ph.D. studies. He also offered me the opportunity to visit Northeastern University in Boston, where I met many nice people. I am more than grateful for the freedom he gave me to work on a variety of projects, the suggestion from him leading me to the right directions in achieving my objectives, and the advice he made to me for my future career plan.

I would like to express my special appreciation to Prof. Allan H. MacDonald for holding my status in UT–Austin and allowing me to participate in his group seminars where I learned lots of physics outside of my field. I am also grateful to other committee members Prof. Jianshi Zhou, Prof. Qian Niu, and Prof. Xiaoqin Li for taking time out of their busy schedules to be on my committee, and for timely answering my emails. In particular, I would like to thank Prof. Jianshi Zhou for explaining material details to me in our

collaborated project and sending recommendations during my job search.

I would like to thank my former group members Qi Chen, Liang Du, Pontus Laurell, Michal Vogl for group orientation and useful suggestions on research, and current colleagues Ze-xun Lin and Martin Rodriguez-Vega in Fiete's group for inspiring me from a perspective of group theory, and Naichao Hu and Nemin Wei in MacDonald's group for helpful discussions on band topology. I am especially grateful to Benedetta Flebus, with whom I collaborated on one of the projects presented in this dissertation, and other current collaborators. They have been reliable partners and collaborators, and I have been enjoying discussing and working with them in person or online through my study in Austin and Boston. Besides, I would like to thank Matt Ervin for his administrative assistance at UT and Sheila Magee for helping me settle into Northeastern physics department.

I would also like to thank all my friends who have brought freshness and color to my Ph.D. life, including Wente Li, Yi Xu, Liwen Tian, Qiyuan Ruan, Guohao Hao, Nihang Fu, Hongwei Chen and many others in both Austin and Boston. Especially, I could not have completed this dissertation without the support of Jie Yu, who provided constant encourages as well as happy distractions to rest my mind outside of my research.

Finally, I would like to thank my parents for their wise counsel and sympathetic ear. You are always there for me and words are never enough.

Thermal Transport and Topological Aspects of Magnons

Publication No. _____

Bowen Ma, Ph.D.
The University of Texas at Austin, 2021

Supervisors: Allan H. MacDonald
Gregory A. Fiete

In this dissertation, we investigate the thermal transport properties of magnons in several antiferromagnetic systems, focusing on their topological nature and their interplay with electrons and phonons. In the second chapter, we study magnon spin thermal transport using a strong coupling approach in pyrochlore iridate trilayer thin films grown along the [111] direction. As a result of the Dzyaloshinskii–Moriya interaction (DMI), the spin configuration of the ground state is an all-in/all-out (AIAO) ordering on neighboring tetrahedra of the pyrochlore lattice. In such a state, the system has an inversion symmetry and a Nernst-type thermal spin current response is well defined. We calculate the temperature dependence of the magnon Nernst response concerning the magnon band topology controlled by spin-orbit coupling parameters and observe topologically protected chiral edge modes. Our study suggests that the [111] grown thin-film pyrochlore iridates are a promising candidate for thermal spin transport and spin caloritronic devices. In the third chapter,

we present a general theory of the longitudinal spin Seebeck effects in the case that the anti-symmetric DMI is considered at the interface. By using an AIAO spin-ordered pyrochlore iridate as the magnetic insulator with a large DMI, we conduct a systematic study of the dependence of the thermally-driven interfacial spin current on the temperature gradient, the interfacial DMI interaction and the crystalline orientation along the interface. Our results show that the spin current injected in the metal is surprisingly sensitive to the orientation of the interface and the direction of the Dzyaloshinskii–Moriya (DM) vectors, offering a route for both probing magnetic properties via a spin-transport measurement and engineering efficient heterostructures. In the fourth chapter, we theoretically study magnon-phonon hybridization in a two-dimensional antiferromagnet on a honeycomb lattice. With an in-plane DMI from mirror symmetry breaking, we find non-trivial Berry curvature around the anti-crossing regions among magnon and both optical and acoustic phonon bands, which gives rise to well-defined Chern numbers. We also show that the Chern numbers of this hybridized system are highly tunable by an external magnetic field. For experiments, we evaluate the thermal Hall conductivity reflecting the non-trivial Berry curvatures of the excitations and propose the possibility of observing valley Hall effects resulted from spin-induced chiral phonons. Our study complements prior work in magnon-phonon hybridized systems without optical phonons and suggests possible applications in spin caloritronics with topological magnons and chiral phonons.

Table of Contents

List of Tables

List of Figures

Chapter 1

Introduction

Heat is one of the most basic concepts in physics, and the transfer of heat has been studied in condensed matter for centuries. In 1822, based on experiments, Fourier [15] wrote down the famous differential equation of thermal conduction, also known as Fourier's law,

$$\mathbf{j}_Q = -\kappa \nabla T, \tag{1.1}$$

providing a definition of thermal conductivity (tensor) κ, where $\mathbf{j}_Q$ is the heat flux (in units of $\mathrm{W/m^2}$) and ∇T is the temperature gradient (K/m). From then on, large efforts have been made on developing a theoretical model for thermal conductivity, such as kinetic theory for dilute gases [35] and the Wiedemann-Franz Law [54] for metals. Among them, Debye model [37] is one of the most remarkable theoretical predictions on thermal conductivity for non-metallic solids, where the heat is transferred via lattice vibrations, or phonons in the quasi-particle language of condensed matter physics. With the development of quantum mechanics, the concepts of quasi-particles generalize the study of thermal conductivity to other bosonic excitations, e.g., magnons [21]. As collective modes of spin waves, magnons attract particular attention in the community [103, 12], since they do not only carry energies but also possess spin

angular momenta which can be utilized for information processing [83, 109, 33]. Moreover, similar to fermionic excitations, magnons can also develop a non-trivial bosonic geometric phase, from which interesting topological phases of matter can emerge. This further enriches the phenomena of magnon thermal transport. Motivated by these, we will present three theoretical works related to thermal transport and topological aspects of magnons in this dissertation. In Chapter 2, we will study transverse magnon spin current thermal response arising from bosonic Berry curvature, i.e, magnon Nernst effects, in an all-in/all-out (AIAO) pyrochlore iridates. In Chapter 3, with an asymmetric exchange coupling at the interface of magnetic insulator|non-magnetic metal heterostructure, we will present a general theory on the interfacial thermal spin transfer between magnons in the insulators and metallic electrons, which is also known as the longitudinal spin Seebeck effect, and provide a numerical study with an AIAO pyrochlore iridate as the insulator. The last work will be presented in Chapter 4, where we investigate the topological magnon-phonon hybridization with the asymmetric Dzyaloshinskii–Moriya interaction in a two-dimensional antiferromagnet. Before going into the details of our work, let us briefly review some backgrounds on spin calritronics and topological aspects in particle transport.

1.1 Spin Caloritronics

Spin caloritronics[1] [183, 16, 200] is an emerging field of spintronics, which is involved with non-equilibrium phenomena related to spin, charge, entropy, energy transport and their interplay in magnetic materials. The study of spin caloritronics can be tracked to 1987, when Johnson and Silsbee [78] first theoretically proposed a spin transport analog to Seebeck effects originated from an interfacial thermoelectric effect. As the spin current in their discussions is carried by spin-polarized conduction electrons, their work nowadays is classified as a "spin-dependent" Seebeck effect, where the spin current $\mathbf{J}_s$ is defined as the difference between the contribution of spin-up and spin-down channels,

$$\mathbf{J}_s = \mathbf{J}_\uparrow - \mathbf{J}_\downarrow. \tag{1.2}$$

At a ferromagnet|non-magnetic metal interface, because the two polarized spin-transport channels have different thermoelectric properties, the individual Seebeck coefficients for the two spin channels are not equal. A spin current can be injected from ferromagnet to non-magnetic metal by a thermal gradient across the junction, reflecting the conservation of spin currents at the contact. The spin current of this kind has been observed in lateral spin-valve structures [171] and the length scale is in the same order as the spin-flip diffusion length of conduction electrons which is around 100–1500 nm [76, 75, 178].

[1] From 'calor', the Latin word for heat.

However, in 2008, Uchida *et al* [182] demonstrated a thermally-driven spin current is injected from a ferromagnetic film into the attached non-magnetic metal by observing a thermal voltage from an inverse spin Hall charge current [170] $\mathbf{J}_c$ as

$$\mathbf{J}_c = e\theta_H \hat{\sigma} \times \mathbf{J}_s, \tag{1.3}$$

where e is the elementary charge, θ_H is the Hall angle, $\mathbf{J}_s$ and $\hat{\sigma}$ is the spin current and its polarization. They further found the signal is over a macroscopic scale of several millimeters, which is surprisingly longer than the spin-flip diffusion length of conduction electrons. It suggests that it is not the conduction electrons but the collective mode of spin waves leading to the thermal spin current. Because of its difference with 'spin-dependent' Seebeck effect, this phenomenon is termed as spin Seebeck effect or magnonic Seebeck effect. This collective effect has aroused many intriguing proposals and realizations to utilize magnons in spin caloritronics [74, 34] as magnons have low dissipation [134] and can provide a pure spin current in insulating systems. In addition, the topological properties of magnon can lead to interesting transport phenomena which are similar to those in topological electronic systems, and we will introduce them in next section.

1.2 Topological Transport

One of the most famous examples of topological effects on transport phenomena is the integer Hall effect [102], also known as the quantum Hall

effect, where a quantized Hall conductivity σ_{xy} is observed in two-dimensional (2D) electron gas subjected to strong magnetic fields and low temperatures

$$\sigma_{xy} = \nu \frac{e^2}{h}, \quad \nu = 1, 2, 3, ... \tag{1.4}$$

where e is the elementary charge and h is Planck's constant, and ν is exactly an integer known as the (first) Chern number, given by the integral of Berry curvature [203, 20] $\Omega^z_{n\mathbf{k}}$ along the Brillouin zone (BZ) as [152]

$$\begin{aligned} \nu = C_n &= \frac{1}{2\pi} \int_{BZ} d^2\mathbf{k}\, \Omega^z_{n\mathbf{k}}, \\ \mathbf{\Omega}_{n\mathbf{k}} &= i \left\langle \nabla_{\mathbf{k}} u_{n\mathbf{k}} \right| \times \left| \nabla_{\mathbf{k}} u_{n\mathbf{k}} \right\rangle \end{aligned} \tag{1.5}$$

where n is a band index, and $|u_{n\mathbf{k}}\rangle$ is the Bloch wavefunction for n-th band. Later, Haldane [61] introduced a model on graphene to exhibit integer Chern numbers without magnetic fields, where the Chern number can be understood as a winding number of the map from the 2D BZ manifold T^2 torus to a two-band manifold S^2 sphere[2] [9]. As long as the gap between the bands is not closing, the topology of the bands can not change and thus guarantee that the Chern number, as well as the Hall conductance, is topologically protected and robust under perturbation. While the integer quantum Hall state is insulating in the bulk, it changes the Chern number at the boundary in contact with the topologically trivial vacuum, producing topologically protected edge modes across the gap [65, 66]. That is also these edge modes that give rise to the integer Hall conductance, connecting topology to transport properties.

[2]More generally, SU(N) for N bands

From a geometric perspective, topology is not unique for fermionic systems, and indeed, it has been realized in bosonic systems [13], such as photonic systems [93, 210], ultracold bosonic atoms [3, 116], polaritonic systems [101, 173, 89], and also magnonic systems [133, 195, 168]. Though the Hilbert space of bosons is different from the space of fermions and needs extra care[3], the topological properties of bosonic bands are also encoded in the Berry phase and Berry curvature. Thus, similar to electronic cases, topological properties of the bands can induce Hall-like effects in magnonic systems, such as thermal Hall effects [91, 139] and magnon Nernst effects [30, 223, 169], where a transverse thermal conductivity or a spin current is presented with a thermal gradient. These effect has been theoretically studied and experimentally observed in a variety of magnetic ordered [105, 106, 161] and frustrated systems [70, 90, 144, 44, 212]. In addition, many other topological phases of matter with magnonic bands attract great interest in the community, such as the Kane-Mele model [98], topological insulators [69, 218], Dirac [142, 140, 148] and Weyl magnons [113, 145].

In the following chapters, we will show an asymmetric exchange coupling that developed from spin-orbital couplings (SOC) in magnetic systems, i.e., Dzyaloshinskii–Moriya interaction [47, 130],

$$H_{DM} = \mathbf{D}_{ij} \cdot (\mathbf{S}_i \times \mathbf{S}_j), \tag{1.6}$$

can play a key role in the transport of magnons and their topological properties.

[3]It will be shown in the following chapters.

1.3 Outline

This dissertation is organized as follows. In Chapter 2, a study on the magnon Nernst effects in pyrochlore iridates thin film is presented, where we first introduce a spin Hamiltonian of pyrochlore iridates thin film and find its topological band dispersions [Sec. 2.1], and then calculate the magnon Nernst response coefficients with a range of coupling parameters [Sec. 2.2].

In Chapter 3, a general theory of spin Seebeck effects with interfacial Dzyaloshinskii–Moriya interactions is provided, where the model for the insulator|metal heterostructure is introduced in the first section [Sec. 3.1], and in the second section [Sec. 3.2], a numerical calculation on an insulating pyrochlore iridate with an all-in/all-out spin ordering is conducted to evaluate the effects of temperature, interfacial coupling and crystalline orientation on spin transfer at the interface.

In Chapter 4, we investigate the topological magnon-polaron in a two-dimensional antiferromagnet with a magnon-phonon coupled model [Sec. 4.1], and explore the band topology with a magnetic field [Sec. 4.2], then discuss possible experimental observations of topological properties by thermal Hall and valley Hall effects [Sec. 4.3].

We end the dissertation with a summary and an outlook in Chapter 5, and provide three appendices with details in numerical method for topological bosonic systems and derivations on magnon-electron couplings and spin currents used in Chapter 3.

Chapter 2

Magnon Nernst Effects in Pyrochlore Iridates Thin Films

In this chapter[1] , we theoretically study the magnon spin thermal transport using a strong coupling approach in pyrochlore iridate trilayer thin films grown along the [111] direction. Over the last two decades, the pyrochlore family of iridate compounds, $A_2Ir_2O_7$, where A is a rare earth element and O is oxygen, has been subjected to intense scrutiny as the family constitutes a rare class of materials where the energy scales of spin-orbit coupling, Coulomb interaction [191, 7] and the electronic bandwidth are all comparable [198, 154, 162]. In particular, the interplay between spin-orbit coupling [153, 62, 129, 5] and electron correlations [108] makes pyrochlore iridate a promising platform for studying quantum phenomena where topology and magnetic frustration compete on the same footing [198, 118]. During a metal to insulator transition [206, 124], interesting phases of matter such as the axion insulator [207, 27, 57], fractionalized states [119, 86, 110, 158, 88, 121], and Dirac or Weyl semi-metals

[1]The results presented here are based on the research article: Bowen Ma and Gregory A. Fiete, *Intrinsic Magnon Nernst Effects in Pyrochlore Iridate Thin Films*, arXiv: 2107.09613 (2021). B. Ma suggested the project, performed the calculations and wrote the computer code. G. A. Fiete supervised the project. Both authors participated in discussions, and in writing the manuscript.

[191, 185, 199, 27, 208], emerge with increasing the electron-electron interaction strength. The properties of these phases can be detected in some cases via electrical measurements, as they can lead, e.g., to the anomalous Hall effect [208].

Besides electronic phases, in the limit of strong electron-electron interaction, pyrochlore iridates behave as a magnetic insulating system with strong spin-orbit coupling [107] giving rise to an asymmetric Dzyaloshinskii–Moriya interaction (DMI). As a result of this DMI, pyrochlore iridates are presented in a non-collinear all-in/all-out ordering on neighboring tetrahedra of the pyrochlore lattice [167], which is possible to provide arbitrarily polarized spin currents and easy to switch to other ordered ground states with different magnetic point group symmetries as well as localized spin textures with nontrivial topology, e.g. skyrmions [22]. Motivated by these interesting properties, we study the transverse spin transport of magnons induced by a longitudinal temperature gradient, i.e, magnon Nernst effects, in a pyrochlore iridate thin film. We evaluate the effect of magnon band topology on the Nernst thermal response along with varying the temperature, which suggests pyrochlore iridates are potential materials for exploring the interplay between topology and spintronics.

The chapter is organized as follows. In Sec. 2.1, we introduce the spin model and calculate the topological magnon band evolution with the DMI using a generalized Bogoliubov transformation. We also investigate the spin current chirality of the topologically protected edge modes in a strip geometry.

In Sec. 2.2, we calculate the spin Berry curvature of a thin film trilayer to study the effects of the DMI on the magnon Nernst response coefficients. We find sign changes of the coefficients by modifying the DMI or raising the temperature of the system. In Sec. 2.3, we provide a discussion on experimental realizations and summarize the main conclusions of our work.

2.1 Model

2.1.1 Spin Hamiltonian

To study the magnon thermal transport, we focus on quasi-2D pyrochlore iridate thin films with non-magnetic A site ions grown in the [111] direction [73, 72, 29, 105], as shown in Fig. 2.1.

The alternating triangular and kagome layers along the [111] axis preserves the spatial inversion symmetry of the lattice. Because of the absence of a mirror symmetry along the [111] direction, the number of atoms in the unit cell of this triangular-kagome-triangular (TKT) thin film is different from the bulk system. However, we assume that the spin Hamiltonian, which consists of only nearest-neighbor interactions, takes the same form as in the bulk case [190, 48, 107],

$$H = \sum_{ij} [J\mathbf{S}_i \cdot \mathbf{S}_j + \mathbf{D}_{ij} \cdot \mathbf{S}_i \times \mathbf{S}_j + S_i^a \Gamma_{ij}^{ab} S_j^b], \tag{2.1}$$

where $\mathbf{S}_i (S_i^a)$ is the spin moment (component) on site i, and J represents the antiferromagnetic Heisenberg coupling, $\mathbf{D}_{ij}$ is the Dzyaloshinskii–Moriya (DM) interaction on bond ij, and Γ_{ij}^{ab} is the symmetric anisotropic exchange

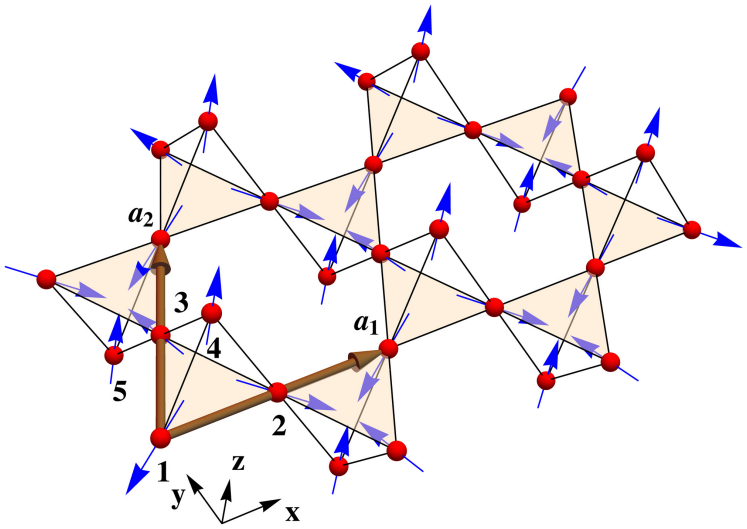

Figure 2.1: The triangular-kagome-triangular (TKT) lattice structure with an AIAO spin ordering for an [111] oriented growth. Red spheres and blue arrows are Ir atoms and the effective spins-1/2 degrees of freedom, respectively. The number of atoms in the unit cell is five (3 from the central kagome plane, and 1 each from an "up" and "down" pointing tetrahedron), in contrast to the bulk case which has 4 atoms in the unit cell: Labeled sites 4 (5) consist of a triangular plane above (below) the kagome plane. The lattice vectors are $\mathbf{a}_1 = a(1, 0, 0)$ and $\mathbf{a}_2 = a(\frac{1}{2}, \frac{\sqrt{3}}{2}, 0)$ with a lattice constant a.

coupling tensor. With a large cubic crystal field from the oxygen octahedra surrounding each Ir^{4+} ion along with a strong spin-orbit coupling (SOC), we take the magnetic moment of Ir^{4+} as an effective spin 1/2 because of the splitting of the t_{2g} orbitals into total angular momentum 1/2 (partially filled) and 3/2 (completely filled) manifolds in the strong SOC limit [96, 214].

Based on symmetry alone, the direction of the DM vectors in the TKT thin film cannot be completely determined from Moriya's rule [130, 131]. However, if we only include the DMI arising from nearest neighbors, the DM vector

of each bond is parallel to the opposite bond allowed by the mirror symmetry of the Ir^{4+} tetrahedron [92]. In our study of the magnon Nernst effects from topological magnon bands, we choose the sign of the DM vectors to obtain a stable AIAO spin ordering [48], as shown in Fig.2.1. In such a state, the couplings can be parametrized as [105] as

$$J = \frac{4t^2}{U}\left[\cos^2\left(\frac{\theta_t}{2}-\theta\right) - \frac{1}{3}\sin^2\left(\frac{\theta_t}{2}-\theta\right)\right], \tag{2.2}$$

$$\mathbf{D}_{ij} = \frac{8t^2}{U}\cos\left(\frac{\theta_t}{2}-\theta\right)\sin\left(\frac{\theta_t}{2}-\theta\right)\hat{v}_{ij}, \tag{2.3}$$

$$\Gamma^{ab}_{ij} = \frac{8t^2}{U}\sin^2\left(\frac{\theta_t}{2}-\theta\right)\left(\hat{v}^a_{ij}\hat{v}^b_{ij} - \frac{\delta^{ab}}{3}\right), \tag{2.4}$$

where $\theta_t = 2\arctan\sqrt{2}$ is the tetrahedral angle, t is the nearest-neighbor hopping energy, U is the on-site Hubbard interaction, and θ, which can vary between $\arctan\sqrt{2}$ to $\pi - \arctan\sqrt{2}$, is a parameter that controls the ratio among the couplings. The parameter θ depends on the material details [107], and is not easy to freely control by static external parameters. However, out-of-equilibrium, with Floquet engineering, it is possible to control the interactions by using circularly polarized light. In such a periodically driven system, the Hubbard interaction U can be renormalized into an effective term $U(\omega)$ that depends on the frequency ω and polarization of the light [24, 68]. In addition, laser illumination can modify the hopping terms and Hubbard terms indirectly with lattice vibrations and distortions [53, 137]. With these two methods, the coupling strengths can be experimentally tuned in principle, in addition to the application of static substrate strain and hydrostatic pressure which provide a more limited control route.

2.1.2 Spin-Wave Analysis

To study the magnon Nernst effect, a spin-wave analysis is necessary to obtain magnon dispersions. Because of the non-collinearity of the system, there is no global S_z direction, so one must orient the Cartesian coordinate system for each sublattice such that the $\hat{\mathbf{z}}$-axis locally lies along the classical ground-state orientation of the onsite macro-spins [143, 52, 117]. In other words, the spin $\mathbf{S}_i(\theta_i, \phi_i)$ is related to the one in the local frame of reference, $\mathbf{S}'_i$, as $\mathbf{S}'_i = \mathcal{R}_i \mathbf{S}_i$ with

$$\begin{aligned} \mathcal{R}_i &= \mathcal{R}_y(-\theta_i)\mathcal{R}_z(-\phi_i) \\ &= \begin{bmatrix} \cos\theta_i & 0 & -\sin\theta_i \\ 0 & 1 & 0 \\ \sin\theta_i & 0 & \cos\theta_i \end{bmatrix} \begin{bmatrix} \cos\phi_i & \sin\phi_i & 0 \\ -\sin\phi_i & \cos\phi_i & 0 \\ 0 & 0 & 1 \end{bmatrix}, \end{aligned} \tag{2.5}$$

where the matrix $\mathcal{R}_{z(y)}(\theta)$ is a right-handed rotational matrix of angle θ about the $\hat{\mathbf{z}}(\hat{\mathbf{y}})$ axis, and $\theta_i(\phi_i)$ is the polar (azimuthal) angle of the classical ground-state orientation of $\mathbf{S}_i$.

In the local reference frame of each sublattice, a local $\hat{\mathbf{z}}$ direction is well-defined and the sublattice spin can then be expressed with a Holstein-Primakoff representation [71] as

$$\begin{cases} S'^{+}_i = \sqrt{2S - {a_i}^\dagger a_i}\, a_i \\ S'^{z}_i = \left(S - {a_i}^\dagger a_i\right), \end{cases} \tag{2.6}$$

where $S = \frac{1}{2}$ is the magnitude of the local spin.

If we ignore the higher-order terms leading to magnon-magnon interactions, the spin Hamiltonian can then be truncated to quadratic order as,

$$H = \frac{1}{2} {\mathbf{X}_\mathbf{k}}^\dagger H_\mathbf{k} \mathbf{X}_\mathbf{k}, \tag{2.7}$$

where $\mathbf{X_k} = (a_1(\mathbf{k}), \ldots, a_5(\mathbf{k}), a_1^\dagger(-\mathbf{k}), \ldots, a_5^\dagger(-\mathbf{k}))^T$ expands the Hilbert space into a particle-hole space (PHS) and $H_\mathbf{k}$ stands for a bosonic Bogoliubov-de Gennes (BdG) Hamiltonian [168] also in a particle-hole symmetric form as

$$H_\mathbf{k} = \begin{bmatrix} A(\mathbf{k}) & B(\mathbf{k}) \\ B^*(-\mathbf{k}) & A^*(-\mathbf{k}) \end{bmatrix}. \tag{2.8}$$

To diagonalize this BdG Hamiltonian[2], one needs to use a paraunitary matrix $Q_\mathbf{k}$ which satisfies

$$Q_\mathbf{k}^\dagger \sigma_3 Q_\mathbf{k} = \sigma_3,\ Q_\mathbf{k}^\dagger H_\mathbf{k} Q_\mathbf{k} = \begin{bmatrix} E_\mathbf{k} & \\ & E_{-\mathbf{k}} \end{bmatrix}, \tag{2.9}$$

where $\sigma_3 = \mathrm{Diag}(1, -1) \bigotimes \mathcal{I}_5$ denotes the bosonic commutator in particle-hole space, and $E_\mathbf{k}$ are the eigenenergies. Here, $Q_\mathbf{k}$ can be regarded as a general Bogoliubov transformation [168, 38] similar to the case in collinear antiferromagnets [100].

With Eq. (2.5)–(2.9), we obtain the magnon dispersions along a high symmetry point path (see Fig. 2.2) in Fig. 2.3, and study band evolutions by varying the ratio control parameter θ. In Fig. 2.4, we observe several gap closings and reopenings among the five bands which changes the band topology, and we list the Chern numbers in the phase between touchings in Table 2.1.

As the Chern numbers are different below and above the band gap, we expect magnon edge currents to carry spin angular momenta producing a magnon Nernst spin current in the presence of a temperature gradient [127, 157].

[2]More details can be found in Appendix A.

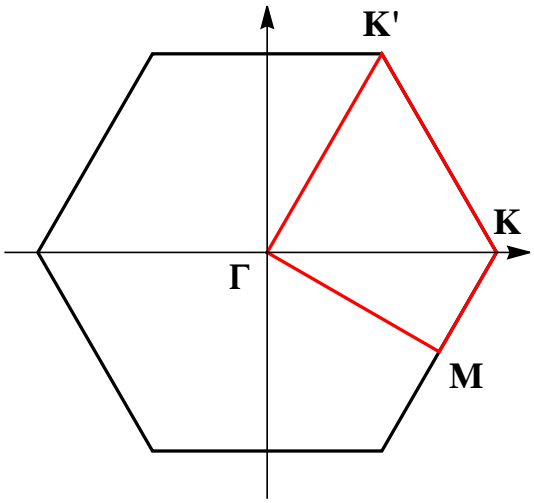

Figure 2.2: The hexgonal Brillouin zone of the TKT thin film. High symmetry points denote as $\Gamma = (0,\ 0),\ M = (\frac{\pi}{a},\ -\frac{\pi}{\sqrt{3}a}),\ K = (\frac{4\pi}{3a},\ 0),\ K' = (\frac{2\pi}{3a}, \frac{2\pi}{\sqrt{3}a})$. The red line is the path along high symmetry points.

2.1.3 Edge States

In contrast to previously studied systems with magnon Nernst effects [30, 223, 112], in our TKT thin films there is a direct gap above the lowest band. Since the sum of Chern numbers below a gap defines a winding number that is in direct correspondence with the number of edge modes [98, 127], we further study the spin current at the edges in a strip geometry. In Fig. 2.5, there are two opposite edge modes (i.e., one on each edge but one being a continuation of the other in a finite area strip/system) within the gap as the lowest band has Chern number $+1(-1)$ for $\theta < (>)1.26$. The $\mathbf{k}$-dependence of the spin of these two edges is plotted in Fig. 2.6 which shows that the chiral edge modes propagating along the two edges have the same y and z spin components due

Table 2.1: Chern numbers in the phases between touchings. We calculate the Chern numbers with the Fukui lattice discretization method [179] for momentum space grids of 1001 × 1001 sites.

θ	< 1.003	1.003-1.04	1.04-1.103	1.103-1.108	1.108-1.18	1.18-1.20	1.20-1.26	> 1.26
D/J	< 0.096	0.096-0.17	0.17-0.3	0.3-0.31	0.31-0.47	0.47-0.51	0.51-0.65	> 0.65
Bottom band	+1	+1	+1	+1	+1	+1	+1	-1
	+2	+2	-1	-1	-1	-1	-1	+1
	-3	-4	-1	-1	-3	+3	+3	+3
	+1	+2	+2	-1	+1	-3	-1	-1
Top band	-1	-1	-1	+2	+2	0	-2	-2

to the inversion symmetry between the pairs, and thus contribute opposite spin currents, while there is no x-component, which vanished due to the $M_{yz}\mathcal{T}$ symmetry of the system.

2.2 Magnon Nernst Effect

In this section, we study a magnon Nernst effect, which can generate a transverse magnon spin current $\mathbf{J}^s$ in the TKT thin film from a longitudinal temperature gradient ∇T. Here we only focus on the intrinsic effect of magnon Berry curvature, which induces an anomalous velocity and a transverse motion of magnons [125]. Generally, the spin angular momentum in a non-collinear system with SOC is not conserved [165, 135]. In this case, one cannot denote a good spin quantum number for each magnon band and the definition of a conserved spin current needs to include a torque term [202]. In our case, the non-collinearity arises from the DMI, which breaks the conservation of a spin

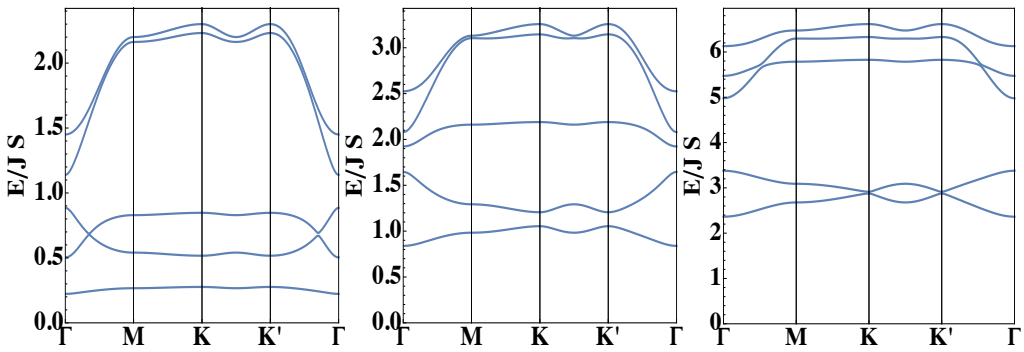

(a) $\theta = 0.98,\ D/J = 0.049$ (b) $\theta = 1.07,\ D/J = 0.23$ (c) $\theta = 1.35,\ D/J = 0.88$

Figure 2.3: Spin-wave spectra for different θ values. Energies are given in units of JS. The Chern numbers from bottom are (a)$(+1, +2, -3, +1, -1)$, (b)$(+1, -1, -1, +2, -1)$ and (c)$(-1, +1, +3, -1, -2)$.

angular momentum. However, with spatial inversion symmetry, the average torque response is zero and a total s-polarized spin current contribution from the MNE, $J_i^s = \alpha_{ij}^s \nabla_j T$ is well-defined [112] and the magnon Nernst coefficient (MNC) α_{ij}^s can be obtained as,

$$\alpha_{ij}^s = \frac{2k_B}{V} \sum_{n=1}^{5} \sum_{\mathbf{k}} (\Omega_{n,\mathbf{k}}^s)_{ij} c_1[g(E_{n\mathbf{k}})], \tag{2.10}$$

where $c_1(x) = (1+x)\ln(1+x) - x\ln x$, $g(x) = (e^{x/k_BT} - 1)^{-1}$ is the Bose-Einstein distribution, and a spin Berry curvature is defined as [223, 112],

$$(\Omega_{n,\mathbf{k}}^s)_{ij} = \sum_{m \neq n} (\sigma_3)_{nn} \frac{2\mathrm{Im}[(j_{i\mathbf{k}}^s)_{nm}(\sigma_3)_{mm}(v_{j\mathbf{k}})_{mn}]}{\left[(\sigma_3)_{nn}E_{n\mathbf{k}} - (\sigma_3)_{mm}E_{m\mathbf{k}}\right]^2}, \tag{2.11}$$

where $v_{\beta\mathbf{k}} = \nabla_\beta H_{\mathbf{k}}$, $j_{i\mathbf{k}}^s = \frac{1}{4}(v_{i\mathbf{k}}\sigma_3\hat{S}^s + \hat{S}^s\sigma_3 v_{i\mathbf{k}})$ is the s-polarized spin current operator in PHS, and $(\dots)_{nm}$ stands for $Q_{n\mathbf{k}}^\dagger(...)Q_{m\mathbf{k}}$ as matrix elements under Bogoliubov representation.

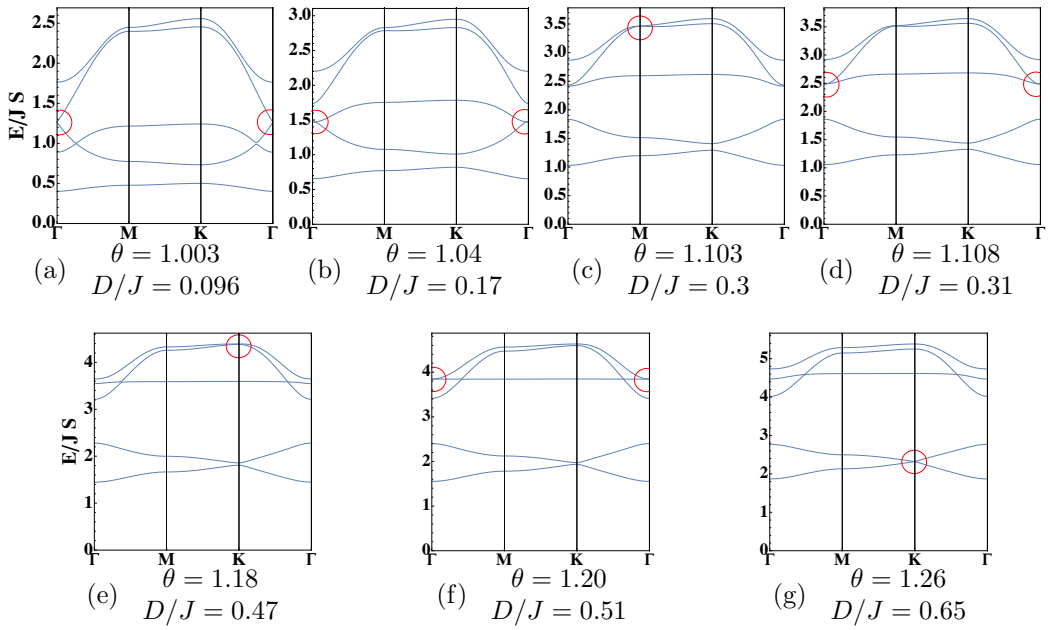

Figure 2.4: Magnon band touching points, at which there occur topological phase transitions. Red circles identify the touching points.

Our TKT thin films are inversion symmetric so we can use Eq. (2.11) for calculating the spin current. More precisely, the thin film has a spatial point group D_{3d} with generators $\{\mathcal{I}, M_{yz}, C_{3z}\}$, and a magnetic point group $\bar{3}m'$ with the AIAO spin ordering. From a symmetry point of view, this magnetic point group is compatible with ferromagnetism, and thus a thermal Hall current is expected [128, 174]. Similarly, by considering the magnetic point group acting on the MNC tensor, one can find that there are only 4 individual response coefficients [8],

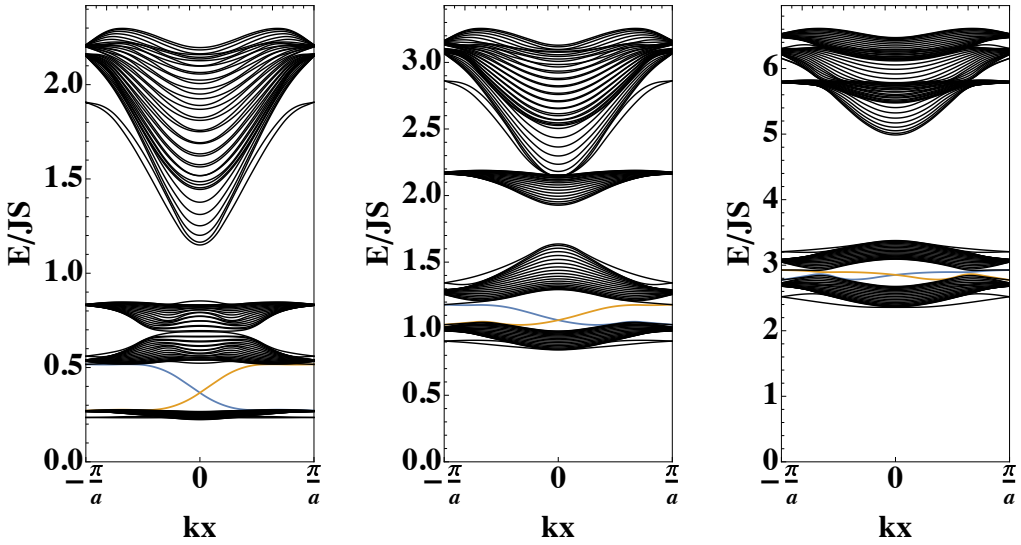

(a) θ=0.98, D/J=0.049 (b) θ=1.07, D/J=0.23 (c) θ=1.35, D/J=0.88

Figure 2.5: Magnon spectra of a 40 atom wide TKT thin film strip. The strip is oriented along the x-direction with finite width in the y-direction. It is periodic along x ($\mathbf{a}_1$)-direction, following the convention in Fig. 2.1. Blue and orange dispersions are the topologically protected magnon edge states spatially separated by the bulk (i.e., they are localized on different edges). Orange states are localized on the right, and blue states are localized on the left of the strip. Note the change in edge state direction in (c) relative to (a), (b).

$$\alpha^x = \begin{bmatrix} -\alpha_1 & 0 & 0 \\ 0 & \alpha_1 & -\alpha_4 \\ 0 & -\alpha_3 & 0 \end{bmatrix}, \; \alpha^y = \begin{bmatrix} 0 & \alpha_1 & \alpha_4 \\ \alpha_1 & 0 & 0 \\ \alpha_3 & 0 & 0 \end{bmatrix},$$
$$\alpha^z = \begin{bmatrix} 0 & \alpha_2 & 0 \\ -\alpha_2 & 0 & 0 \\ 0 & 0 & 0 \end{bmatrix} \tag{2.12}$$

The structure of these tensors is consistent with our results for the edge states (Fig. 2.6), as α^x has no transverse coefficients while y and z-polarized

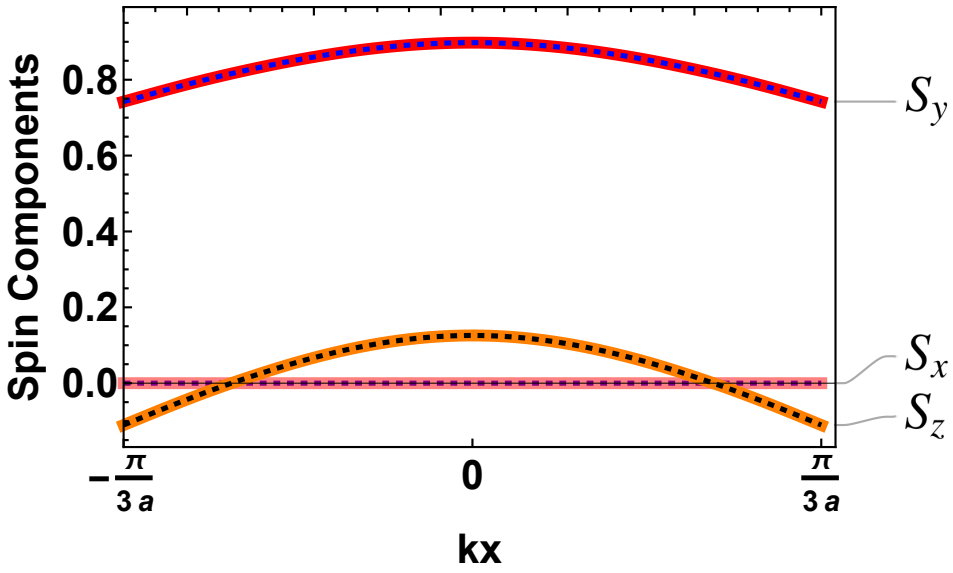

Figure 2.6: Spin components of the edge modes using a strip of 40 atoms width and $\theta = 1.07$. Solid (dashed) lines are for left (right) movers as shown in Fig.2.5. Only the y and z-components are non-zero.

spin components can transport along edges transversely for a temperature gradient along the y-direction. From a more simple picture, since the total net moment within one unit cell is only along the out-of-plane direction, i.e. z-direction, α^x and α^y with in-plane polarizations should have similar independent coefficients, α_i for $i = 1, 3, 4$, while α^z is different from them (containing only α_2).

The typical lattice constant between iridium ions of bulk pyrochlore iridates is on the order of 10Å [163], and thus in our thin film case, we focus on the magnon Nernst response induced by a temperature gradient within the plane, e.g coefficient α_1 and α_2 corresponding to the magnon Nernst response

α^y_{xy} and α^z_{xy}. The temperature and coupling dependence of these coefficients are shown in Fig. 2.7 and Fig. 2.8 respectively.

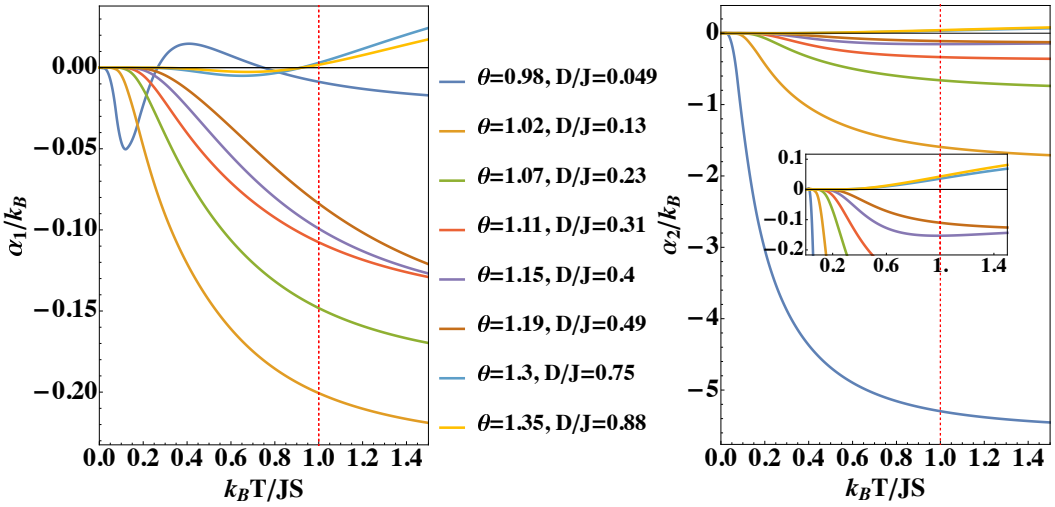

(a) (b)

Figure 2.7: The temperature dependence of (a) α_1 (α^y_{xy}) and (b) α_2 (α^z_{xy}). The inset in (b) is a zoom-in to show the sign change of α_2 for $\theta > 1.26$.

From Fig. 2.8, we can see that the DMI in general suppresses the response coefficients. On one hand, from Fig. 2.3, we have a higher excitation energy of the system with a larger DMI. Then the magnon bands can be accessed only with higher temperature as $c_1(g(E_{n\mathbf{k}}))$ decreases exponentially with increasing energy. On the other hand, most contributions to the MNE are from the lowest two bands, and as shown in Fig. 2.9 the spin Berry curvature of these two bands concentrates at $\mathbf{K}$ and $\mathbf{K}'$ point with opposite signs because of the DMI. When the DMI increases, the two bands move towards one another, and thus $\alpha^s \propto \Omega^s_1(\mathbf{K})(E_{1\mathbf{K}} - E_{2\mathbf{K}})$ is getting smaller. After the

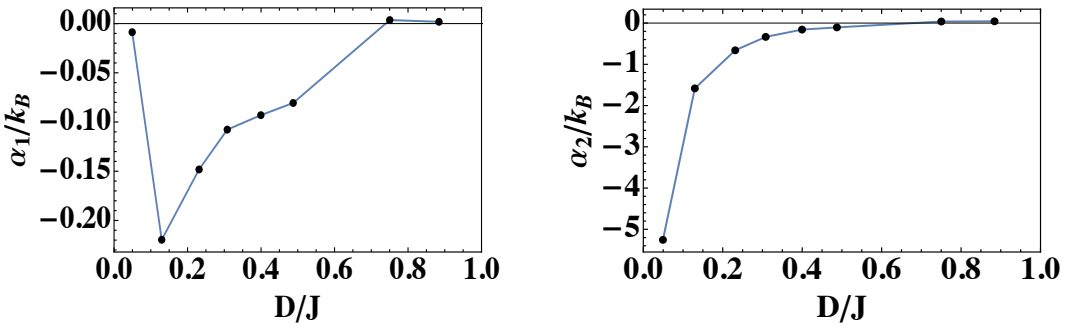

(a) (b)

Figure 2.8: The coupling dependence of (a) α_1 (α^y_{xy}) and (b) α_2 (α^z_{xy}) plotted along the red dashed line in Fig. 2.7(a) and (b) respectively.

two bands touch each other, the MNCs increase again as the gap reopens when $\theta > 1.26$.

In the high temperature limit, the MNE changes sign when $\theta \gtrsim 1.26$, due to the sign change of Chern numbers in the bottom two bands after a topological phase transition. However, since the net moment is along z-direction, $\alpha_2(\alpha^z_{xy})$ results from the spin angular momentum carried by a total thermal Hall magnon current, while $\alpha_1(\alpha^y_{xy})$ comes from the imbalance among magnon modes similar to magnon Nernst effects in collinear antiferromagnets [30]. Because of this, α_1 is more sensitive to the band topology and change of DMI.

For $\theta = 0.98$, the DMI is small compared to the exchange coupling and the system approaches the Heisenberg limit. The low energy scale of this limit supports the contributions to MNE from higher bands when the temperature increases. Thus, instead of a monotonic change respect to the temperature,

α_1 changes sign at $k_BT \approx 0.27JS$ and $k_BT \approx 0.74JS$ reflecting the Chern numbers with alternative sign from the bottom to top as (+1, +2, -3, +1, -1).

For $\theta > 1.26$, although the Chern number of the lowest band changes sign to +1, the spin Berry curvature around M-point with lower energy dominates at low temperature [see Fig. 2.9(c)] and thus gives rise to a response with a negative sign. When temperature increases, the sign of response coefficient will change to positive as the change of Chern number during the phase transition, which is determined by the (spin) Berry curvature at two concentrated point K and K'.

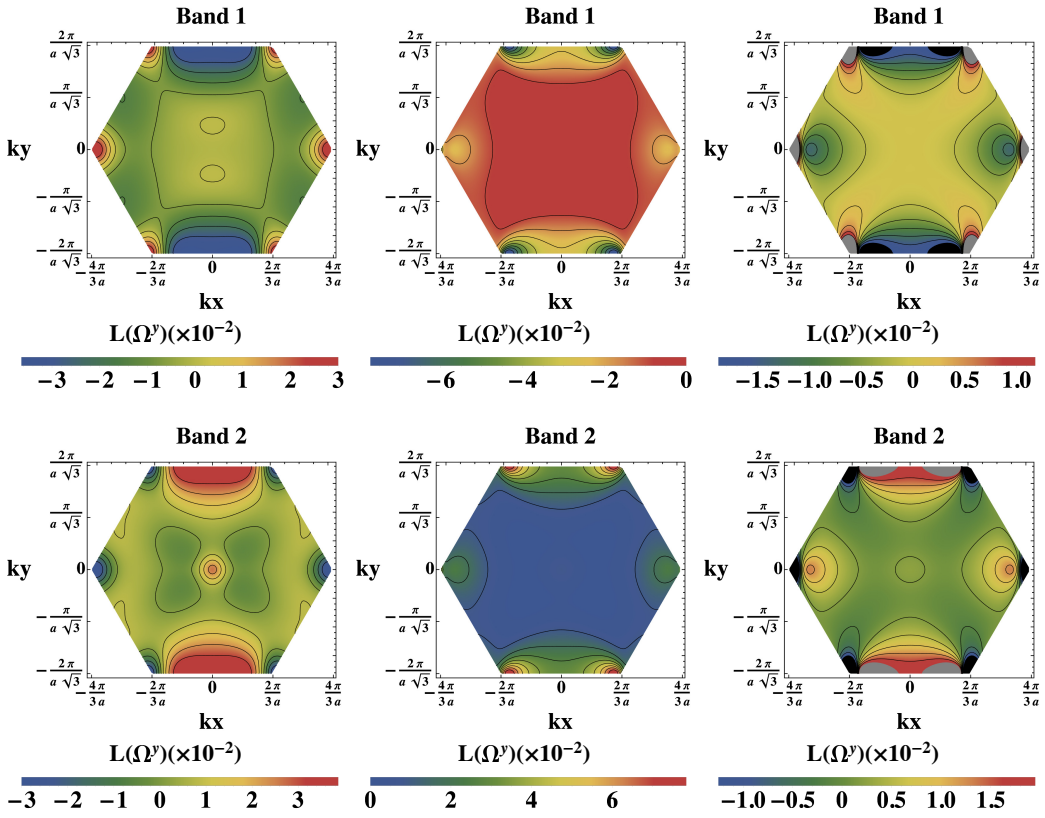

(a) θ=1.07, D/J=0.23 (b) θ=1.15, D/J=0.4 (c) θ=1.35, D/J=0.88

Figure 2.9: Density plots of spin Berry curvatures in log scale $L(\Omega^s) = \text{sign}(\Omega^s)\log(1+|\Omega^s|)$ for lowest two bands (Band 1 is the lowest band). (a-c) are y-polarized spin Berry curvatures for different θ values before and after gap closing. (Continue on next page.)

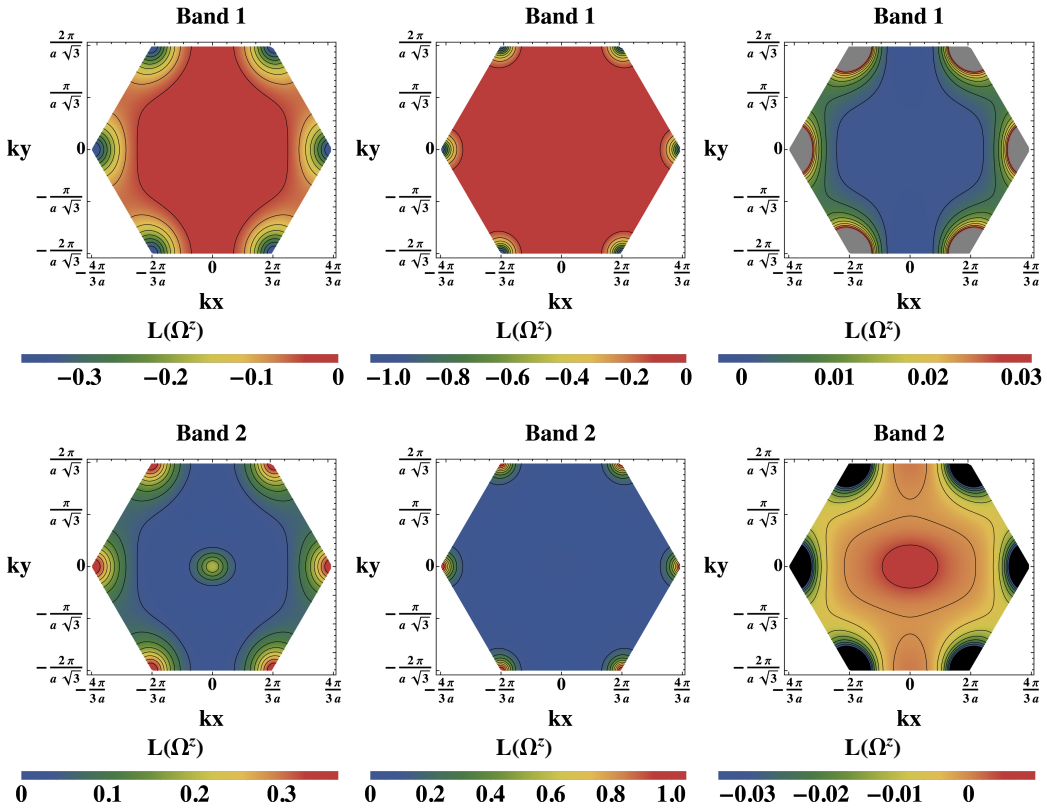

(d) θ=1.07, D/J=0.23 (e) θ=1.15, D/J=0.4 (f) θ=1.35, D/J=0.88

Figure 2.9 (cont.): (d-f) are for z-polarized spin Berry curvatures. Both spin Berry curvatures concentrate mostly at **K** and **K**′ point with opposite signs. Detailed plots of the spin Berry curvature in the vicinity of the gray and black regions, corresponding to the values outside of the range of the scale bar, can be found in Fig. 2.10.

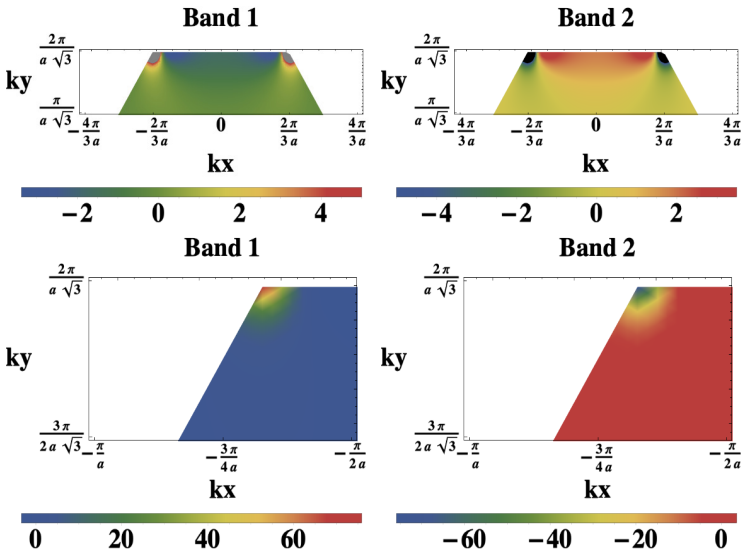

(a)L(Ω^y)($\times 10^{-2}$) for θ=1.35

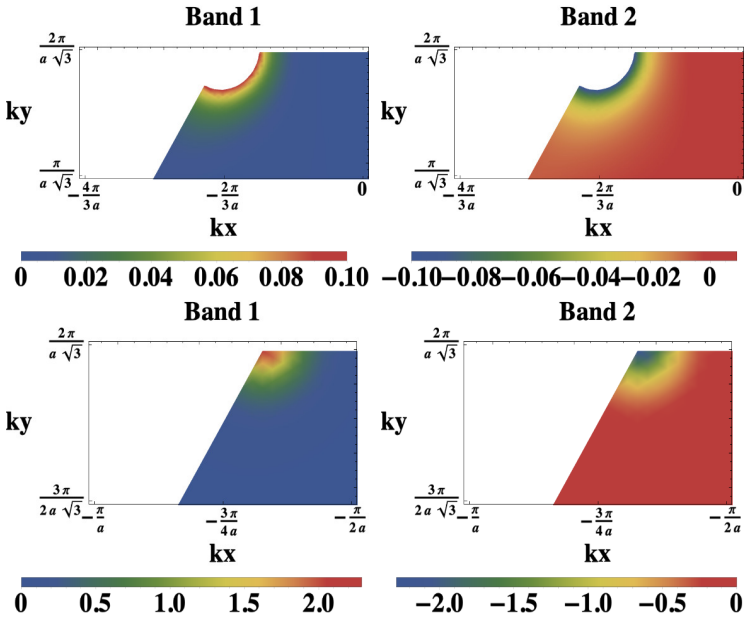

(b)L(Ω^z) for θ=1.35

Figure 2.10: Spin Berry curvature in different ranges around **K**, **K**′ and **M** points.

2.3 Discussion and Conclusion

We have calculated the magnon Nernst response coefficients in the TKT pyrochlore iridates thin film with an all-in/all-out spin ordering. In contrast with the magnon Nernst effect in collinear systems, we found transverse spin currents with both y- and z-polarization (for a thermal gradient applied along the x-direction). As an experimental estimate, if we assume a thickness of 20 Å (for a trilayer, taken from the lattice constant of a material [163, 166] such as $Y_2Ir_2O_7$) with a 20 K/mm temperature gradient, we expect a y-polarized (z-polarized) spin current on the order of $10^{-11}(10^{-10})$ J/m^2, which makes pyrochlore iridates a promising experimental candidate for observing the magnon Nernst effect in non-collinear systems.

In addition, we found the TKT trilayer film has a direct gap that supports two topological nontrivial edge modes. These edge modes have not been discussed in the context of the magnon Nernst effect before. They provide a spin current channel at each edge with opposite signs, and may be detected separately at the edge by local measurements [46]. Since these edge modes are topologically protected, it is possible to realize a spin current only weakly affected by disorders in the bulk [204].

Our results also show that the DMI can significantly impact the response coefficients, as it can modify the nontrivial geometric aspect of magnon bands, including topological transitions. The sign change of the coefficients is due to the distribution of spin Berry curvature throughout the Brillouin zone and the thermal population of bands with different Chern numbers. In order

to observe the sign change of α_1 for $\theta = 0.98$ (1.30), one must have an experimental resolution of the order of 10^{-11} (10^{-12}) J/m^2, which can be converted into and measured by an inverse spin Hall current on the order of 10^4 (10^3) A/m^2 [170]. Therefore, the magnon Nernst effect can also be used as a probe to study the topological properties of magnons in magnetic insulators. In addition, the magnon spin transport can be tuned with an external magnetic field, either by a spin ground state phase transition in the strong-field limit or a Zeeman energy splitting in the weak-field limit [186, 113].

Chapter 3

Spin Seebeck Effects with Interfacial Dzyaloshinskii-Moriya Interactions

In this chapter[1] , we study another type of thermally-driven spin transport, i.e., the longitudinal spin-Seebeck effect (LSSE) [182, 16] at the interface of a magnetic insulator|non-magnetic metal heterostructure, where a spin current originating in the magnetic insulating system is driven by a temperature gradient and injected longitudinally into the metallic system which then converts the spin current to an electrical current (via spin-orbit coupling) that generates a voltage via the inverse spin Hall effect [170].

As the spin transfer length of LSSE observed in experiments is over a macroscopic scale of several millimeters, which was extraordinarily longer than the spin-flip diffusion length of conduction electrons, it suggests that, instead of the conduction electrons, the dynamics of local moments in the magnetic materials, or magnon, is important to the LSSE. The coupling between electron

[1]The results presented here are based on the research article: Bowen Ma, Benedetta Flebus, and Gregory A. Fiete. *Longitudinal spin Seebeck effect in pyrochlore iridates with bulk and interfacial Dzyaloshinskii-Moriya interaction*, Phys. Rev. B **101**, 035104 (2020). G. A. Fiete suggested and supervised the project. B. Ma's contribution was focus on the calculations of the model with Dzyaloshinskii-Moriya interaction, and writing the computer code. All authors participated in discussions, and in writing the paper.

spins and localized moments at the interface of ferromagnetic insulator—non-magnetic metal or topological insulator has been studied previously, suggesting the interfacial coupling is crucial to the efficiency of spin transfer. However, most theoretical studies of LSSE are primarily with the assumption of an isotropic interfacial exchange coupling. In addition, a spin transport theory remains largely unexplored for systems with non-collinear magnetic orders [52]. The nature of the lattice geometry combined with spin-orbit coupling implies there is no conserved component of the spin in the presence of the spin-rotational symmetry breaking DM terms. However, spin transport can still be well-defined at the interface between these magnetic insulating systems and an adjacent metal. Motivated by these considerations, here we investigate the interfacial spin transport between a non-collinear magnetic insulator|normal metal heterostructure and present a general theory of the LSSE in the case of an antisymmetric Dzyaloshinskii-Moriya interaction (DMI) at the interface, in addition to the usual Heisenberg form. We numerically evaluate the dependence of the spin current on the temperature and bulk DMI using a pyrochlore iridate as a model insulator with an all-in all-out (AIAO) ground state configuration. We also compare the results of different crystalline surfaces arising from different crystalline orientations and conclude that the relative angles between the interfacial moments and Dzyaloshinskii-Moriya vectors play a significant role in the spin transfer. Our work extends the theory of the LSSE by including the anisotropic nature of the interfacial Dzyaloshinskii-Moriya exchange interaction in magnetic insulator|non-magnetic metal heterostructures

and can suggest possible materials to optimize the interfacial spin transfer in spintronic devices.

The chapter is organized as follows. In Sec. 3.1, we introduce our model for the metallic and the non-collinear magnetic insulating systems, and the exchange and DMI-driven interfacial coupling between their spin densities. Using Kubo formalism, we derive an expression for the spin current flowing across the interface of the magnetic insulator|normal metal heterostructure. In Sec. 3.2, we introduce a specific model Hamiltonian for the magnetic insulating phase of pyrochlore iridates and determine the spectra of the magnetic excitations. Applying our transport theory to these results, we present numerical results for the spin current injected from a pyrochlore iridate into a normal metal. We investigate the dependence of the current on the temperature gradient, the ratio between bulk and interfacial DMI interaction and the crystallographic orientation of the interface. Finally, in Sec. 3.3, we discuss our conclusions and possible future directions.

3.1 Model and Approach

3.1.1 Lattice Model

We consider a magnetic insulator (MI)|nonmagnetic metal (NM) heterostructure as illustrated in Fig. 3.1, allowing the magnetic insulator to have any type of non-collinear magnetic configurations at the interface. A constant temperature gradient is applied across the interface of the heterostructure, yielding a local temperature difference near the interface. A better description

may assume a linear temperature variation through the magnetic insulator and into the metallic system, then one would need to express the temperature as a local function of position and express the formulas in terms of quantities with a real-space dependence on the distance from the interface. The physical conclusions of such a calculation would be the same as those we have reached with a simple temperature difference, and very likely the numerical results of computation would be similar to those we reported in Sec. 3.2. For transport problems, it is natural to use periodic boundary conditions in the xy-plane and an open boundary at the interface along the transport z-direction.

3.1.1.1 Nonmagnetic Metal

Because the non-magnetic material used in experiments is usually a good conducting metal, we treat it as a degenerate Fermi gas with no spin accumulation at the interface. Its spin density at position $(\mathbf{r}, z)$ can be written as,

$$\rho(\mathbf{r}, z) = \frac{\hbar}{2} \sum_{\sigma\sigma'} \psi^{\dagger}_{\sigma}(\mathbf{r}, z)\sigma_{\sigma\sigma'}\psi_{\sigma'}(\mathbf{r}, z), \tag{3.1}$$

where σ is the vector of Pauli matrices with σ (or σ') the spin index, $\mathbf{r}$ is a two dimensional in-plane vector, and $\psi^{\dagger}_{\sigma}(\mathbf{r}, z)$ is the electron creation operator for an electron of spin σ at position $(\mathbf{r}, z)$. Because of the translational invariance in the plane parallel to the interface, we can perform a partial Fourier transform with respect to $\mathbf{r}$, where $\psi_{\sigma}(\mathbf{r}, z) = \sum_{\mathbf{k}} \psi_{\mathbf{k}}(\mathbf{r})c_{\mathbf{k}\sigma}(z)$. The $\mathbf{k}$ vector is the in-plane wavevector reciprocal to the two-dimensional coordinate $\mathbf{r}$. The or-

thonormal basis set $\psi_{\mathbf{k}}(\mathbf{r})$ corresponds to plane waves, i.e., $\psi_{\mathbf{k}}(\mathbf{r}) = e^{i\mathbf{k}\cdot\mathbf{r}}/\sqrt{A}$, where A is the area of the interface. The full electronic Hamiltonian can then be written as

$$\mathcal{H}_e = \int \sum_{\mathbf{k}\sigma} \epsilon_{\mathbf{k}} c^{\dagger}_{\mathbf{k}\sigma}(z) c_{\mathbf{k}\sigma}(z) dz, \tag{3.2}$$

with $\langle c^{\dagger}_{\mathbf{k}'\sigma'}(z') c_{\mathbf{k}\sigma}(z)\rangle = n_F(\beta_M \epsilon_{\mathbf{k}})\, \delta_{\sigma,\sigma'} \delta_{\mathbf{k},\mathbf{k}'} \delta_{z,z'}$. Here, $n_F(x) = (e^x + 1)^{-1}$ is the Fermi distribution function, $\epsilon_{\mathbf{k}}$ the single-electron energy and $T_M = \beta_M^{-1}$ (we set the Boltzmann's constant $k_B = 1$) the local temperature of the metal, which may depend on $\mathbf{k}$ and z.

3.1.1.2 Magnetic Insulator

Because of the boundary conditions, the magnetic insulator can be regarded as multiple two-dimensional lattices stacked along the z-direction. It is convenient to write the lattice coordinate as $(\mathbf{R}_m, l)$, labeling the origin of the m-th two-dimensional lattice site in the l-th layer. The m-th two-dimensional lattice unit cell has a noncollinear magnetic configuration $\{\mathbf{S}_\alpha(\mathbf{r}_i)\}$ with a classical macro-spin $\mathbf{S}_\alpha(\mathbf{r}_i)$ located at sublattice $\mathbf{r}_\alpha$ of lattice $\mathbf{R}_m$, where $\mathbf{r}_i = \mathbf{R}_m + \mathbf{r}_\alpha$. Because the magnetic moments are non-collinear, we orient the Cartesian coordinate system for each magnetic site in the same way as introduced in Chapter 2, such that the $\hat{\mathbf{z}}$ axis locally lies along the classical ground-state orientation of the onsite macro-spin [105, 52]. Namely, the macrospin $\mathbf{S}_\alpha$ is related to the one in the local frame of reference, $\mathbf{S}'_\alpha$, as $\mathbf{S}'_\alpha = \mathcal{R}_\alpha(\theta_\alpha, \phi_\alpha)\mathbf{S}_\alpha$, where $\theta_\alpha(\phi_\alpha)$ is the polar (azimuthal) angle of the classical ground-state orientation of $\mathbf{S}_\alpha$.

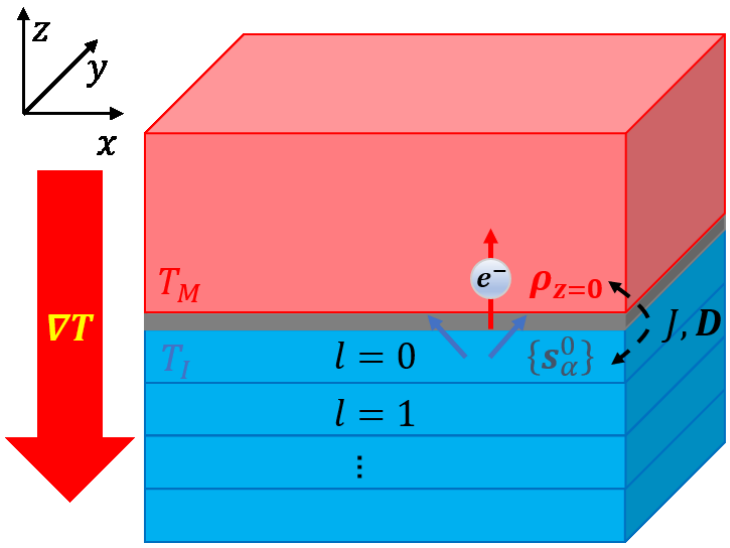

Figure 3.1: Longitudinal Spin Seebeck setup. A thermal gradient ∇T is applied perpendicular to the interface of the heterostructure. The upper red portion is the non-magnetic metal with temperature T_M near the interface, modeled as a degenerate Fermi gas. The lower blue part is the magnetic insulator with temperature T_I, which can be regarded as multiple two dimensional layers with layer index, l. The grey part represents the interface, where the electron spin density, $\rho_{z=0}$, and α-th interfacial magnetic moments, $\mathbf{S}^0_\alpha$, are coupled with an isotropic Heisenberg exchange J and DM interaction $\mathbf{D}$.

In the local frame of reference, the spin at the site $\mathbf{r}_i$ in the l-th layer can be expressed, via the Holstein-Primakoff transformation [71] as

$$\begin{cases} S'^{+}_{\alpha,l}(\mathbf{r}_i) \approx \hbar\sqrt{2S}a^l_\alpha(\mathbf{r}_i) \\ S'^{z}_{\alpha,l}(\mathbf{r}_i) = \hbar\left(S - a^{l\,\dagger}_\alpha(\mathbf{r}_i)a^l_\alpha(\mathbf{r}_i)\right), \end{cases} \tag{3.3}$$

where S is the magnitude of the local spin. Here we ignored higher order terms leading to magnon-magnon interactions. The bosonic operators $a_\alpha(a^\dagger_\alpha)$ are related to the spin-wave annihilation (creation) operators $b_\beta(b^\dagger_\beta)$ via a

Bogoliubov transformation [23, 187], i.e.,

$$\begin{aligned} a^l_\alpha(\mathbf{q}) &= \frac{1}{\sqrt{N}}\sum_m e^{i\mathbf{q}\cdot\mathbf{R}_m} a^l_\alpha(\mathbf{r}_i) \\ &= \sum_{l'}\sum_{\nu=1}^{N_s}\left[M^{ll'}_{\alpha\nu,\mathbf{q}} b^{l'}_\nu(\mathbf{q}) + N^{ll'}_{\alpha\nu,-\mathbf{q}} b^{l'\dagger}_\nu(-\mathbf{q})\right], \end{aligned} \tag{3.4}$$

where $M^{ll'}_{\alpha\nu,\mathbf{q}}$ and $N^{ll'}_{\alpha\nu,-\mathbf{q}}$ are determined from a Bogoliubov transformation that diagonalizes the magnetic excitations of the bulk Hamiltonian of the system, N is the magnetic lattice site number of the two-dimensional layer and N_s is the number of sublattices per unit cell. Thermal magnons in the magnetic insulator follow the Bose-Einstein distribution function $\langle \hat{b^l_\nu}^\dagger(\mathbf{k})\hat{b}^l_\nu(\mathbf{k}')\rangle = n_B\left(\beta_I\omega^l_\nu(\mathbf{k})\right)\delta_{\mathbf{k},\mathbf{k}'}$, where $n_B(x) = (e^x-1)^{-1}$, $\omega^l_\nu(\mathbf{k})$ is the dispersion of the lth layer νth magnonic band, and $T = \beta_I^{-1}$, the local magnon temperature, is below the transition temperature so that the ordering and the fluctuation is well defined.

3.1.1.3 Interfacial Coupling

For simplicity, we assume that the two subsystems have the same Bravais lattice at the interface (corresponding to $z = 0$ in the metal or $l = 0$ in the insulator), that is, the lattice does not change across the interface. Since the interface generally breaks the inversion symmetry, besides a Heisenberg-type interaction with exchange coupling J_{ij}, a Dzyaloshinskii–Moriya interaction (DMI) $\mathbf{D}_{ij}$ could couple spin density $\rho(\mathbf{r}_i = \mathbf{R}_m + \mathbf{r}_\alpha, z = 0)$ and magnetic

moment $\mathbf{S}_{\beta,l=0}(\mathbf{r}_j = \mathbf{R}_n + \mathbf{r}_\beta)$, i.e.,

$$\mathcal{H}_I = \sum_{\langle ij \rangle} \Big[J_{ij} \rho(\mathbf{r}_i) \cdot \mathbf{S}_\beta(\mathbf{r}_j) + \mathbf{D}_{ij} \cdot [\rho(\mathbf{r}_i) \times \mathbf{S}_\beta(\mathbf{r}_j)] \Big], \tag{3.5}$$

where the summation of $\langle ij \rangle$ is only over the pair of nearest-neighbor sites i and j to avoid double-counts and we drop $z = 0$ and $l = 0$ in ρ and $\mathbf{S}$, respectively, for notational brevity.

In each local reference frame, by plugging Eq. (3.3) and Eq. (3.1) into Eq. (3.5) with Bogoliubov transformation Eq. (3.4), we have the interfacial Hamiltonian as[2]

$$\begin{aligned} \mathcal{H}_I \; &= \tfrac{\hbar^2 \sqrt{2NS}}{2A} \textstyle\sum_{<\alpha\beta>} \sum_{\mathbf{qkk'},\mathbf{G}} \sum_{\sigma\sigma'} \sum_{\nu l} \sum_h \delta_{\mathbf{k}-\mathbf{k'}+\mathbf{q},\mathbf{G}} \\ &\quad \times \left({g^l_{\alpha\beta\nu}}^{(h)}(\mathbf{q},\mathbf{k},\mathbf{k'}) {b^l_\nu}^\dagger(\mathbf{q}) c^\dagger_{\mathbf{k}\sigma} L^{(h)}_{\sigma\sigma'} c_{\mathbf{k'}\sigma'} + \text{h.c.} \right), \end{aligned} \tag{3.6}$$

where h index ($h = 1, 2, 3$) refers the $+, -$ and z-components of the spin respectively, $L^{(1,2,3)} = \left(\frac{\sigma^+}{2}, \frac{\sigma^-}{2}, \sigma^z \right)$ and

$${g^l_{\alpha\beta\nu}}^{(h)}(\mathbf{q},\mathbf{k},\mathbf{k'}) = \left[J_{\alpha\beta} {V^l_{\beta\nu,\mathbf{q}}}^{(h)} + |\mathbf{D}_{\alpha\beta}| {U^l_{\alpha\beta\nu,\mathbf{q}}}^{(h)} \right] e^{-i(\mathbf{k}-\mathbf{k'})\cdot\mathbf{r}_\alpha}. \tag{3.7}$$

Here, within a mean-field approximation and far from the magnetic ordering temperature (i.e. $\langle {a^l_\alpha}^\dagger a^l_\alpha \rangle \ll S$), we discard the terms $\propto (S - {a^l_\alpha}^\dagger a^l_\alpha) c^\dagger_{\mathbf{k}\sigma} c_{\mathbf{k'}\sigma'}$ as these are elastic scatterings between electrons off the static magnetic order of the insulator and thus will not depend on the thermal bias [17]. Then Eq. (3.6). can be understood as inelastic scatterings between electrons and thermal magnons in the lowest order, where the contribution from

[2]See details in Appendix B.

the exchange coupling reads as,

$$\begin{cases} {V^l_{\beta\nu,\mathbf{q}}}^{(1)} = \left({M^{0l}_{\beta\nu,\mathbf{q}}}^{\dagger} \cos^2 \frac{\theta_\beta}{2} - N^{0l}_{\beta\nu,-\mathbf{q}} \sin^2 \frac{\theta_\beta}{2} \right) e^{-i\phi_\beta} \\ {V^l_{\beta\nu,\mathbf{q}}}^{(2)} = \left(N^{0l}_{\beta\nu,-\mathbf{q}} \cos^2 \frac{\theta_\beta}{2} - {M^{0l}_{\beta\nu,\mathbf{q}}}^{\dagger} \sin^2 \frac{\theta_\beta}{2} \right) e^{i\phi_\beta} \\ {V^l_{\beta\nu,\mathbf{q}}}^{(3)} = -\frac{\sin\theta_\beta}{2} \left({M^{0l}_{\beta\nu,\mathbf{q}}}^{\dagger} + N^{0l}_{\beta\nu,-\mathbf{q}} \right), \end{cases}$$

and the other term from DMI as,

$$\begin{cases} {U^l_{\alpha\beta\nu,\mathbf{q}}}^{(1)} = i \left[d^3_{\alpha\beta} {V^l_{\beta\nu,\mathbf{q}}}^{(1)} - (d^1_{\alpha\beta} - i d^2_{\alpha\beta}) {V^l_{\beta\nu,\mathbf{q}}}^{(3)} \right] \\ {U^l_{\alpha\beta\nu,\mathbf{q}}}^{(2)} = i \left[(d^1_{\alpha\beta} + i d^2_{\alpha\beta}) {V^l_{\beta\nu,\mathbf{q}}}^{(3)} - d^3_{\alpha\beta} {V^l_{\beta\nu,\mathbf{q}}}^{(2)} \right] \\ {U^l_{\alpha\beta\nu,\mathbf{q}}}^{(3)} = i \left[\frac{d^1_{\alpha\beta} - i d^2_{\alpha\beta}}{2} {V^l_{\beta\nu,\mathbf{q}}}^{(2)} - \frac{d^1_{\alpha\beta} + i d^2_{\alpha\beta}}{2} {V^l_{\beta\nu,\mathbf{q}}}^{(1)} \right], \end{cases}$$

where $\mathbf{d}_{\alpha\beta} = \frac{\mathbf{D}_{\alpha\beta}}{|\mathbf{D}_{\alpha\beta}|} = (d^1_{\alpha\beta}, d^2_{\alpha\beta}, d^3_{\alpha\beta})$.

The amplitudes of the scattering depends on the rotational angles, $\{(\theta_\beta, \phi_\beta)\}$, and Bogoliubov transformation of the bulk magnetic excitations, $\{(M^{0l}_{\beta\nu,\mathbf{q}}, N^{0l}_{\beta\nu,-\mathbf{q}})\}$. Once the geometry of the non-collinear ground state is known, the rotational angles are determined and the latter can be obtained from the magnon Hamiltonian [38, 36, 187].

3.1.2 Spin Currents

To determine the interfacial spin current, we define a total spin accumulation operator $\mathbf{Q}(z)$ at a z-surface as

$$\mathbf{Q}(z) = \int \rho(\mathbf{r}, z)\, d\mathbf{r} = \frac{\hbar}{2} \sum_{\mathbf{k}} \sum_{\sigma\sigma'} c^\dagger_{\mathbf{k}\sigma}(z) \sigma_{\sigma\sigma'} c_{\mathbf{k}\sigma'}(z). \tag{3.8}$$

Assuming that the magnetic order is static and spin density is conserved across the interface of an area A, the interfacial spin current density flowing into the metal can be written as

$$\mathbf{i} = \frac{1}{A}\frac{d\mathbf{Q}}{dt} = -\frac{i}{\hbar}\frac{1}{A}[\mathcal{H}_I, \mathbf{Q}(z=0)]. \tag{3.9}$$

By using Kubo formula [104] to second order in interfacial coupling J_{ij} and $\mathbf{D}_{ij}$, and after plugging Eq. (3.6) and Eq. (3.8) into Eq. (3.9), some algebra[3]and Wick's theorem [196] gives,

$$\begin{cases} \langle i^x \rangle = \frac{\hbar^3 NS}{A^3} \sum_{\nu l} \sum_{hh'} \sum_{\substack{<\alpha\beta> \\ <\alpha'\beta'>}} \sum_{\mathbf{qkk'},\mathbf{G}} \Gamma_{\nu l}(\mathbf{q},\mathbf{k},\mathbf{k}')\delta_{\mathbf{k}-\mathbf{k}'+\mathbf{q},\mathbf{G}} \\ \mathfrak{Re}\left[{g^l_{\alpha\beta\nu}}^{(3)*}(\mathbf{q},\mathbf{k},\mathbf{k}') g^l_{\alpha'\beta'\nu}{}^{(2)}(\mathbf{q},\mathbf{k},\mathbf{k}') - {g^l_{\alpha\beta\nu}}^{(3)*}(\mathbf{q},\mathbf{k},\mathbf{k}') {g^l_{\alpha'\beta'\nu}}^{(1)}(\mathbf{q},\mathbf{k},\mathbf{k}') \right] \\ \\ \langle i^y \rangle = \frac{\hbar^3 NS}{A^3} \sum_{\nu l} \sum_{hh'} \sum_{\substack{<\alpha\beta> \\ <\alpha'\beta'>}} \sum_{\mathbf{qkk'},\mathbf{G}} \Gamma_{\nu l}(\mathbf{q},\mathbf{k},\mathbf{k}')\delta_{\mathbf{k}-\mathbf{k}'+\mathbf{q},\mathbf{G}} \\ \mathfrak{Im}\left[{g^l_{\alpha\beta\nu}}^{(3)*}(\mathbf{q},\mathbf{k},\mathbf{k}') g^l_{\alpha'\beta'\nu}{}^{(1)}(\mathbf{q},\mathbf{k},\mathbf{k}') + {g^l_{\alpha\beta\nu}}^{(3)*}(\mathbf{q},\mathbf{k},\mathbf{k}') {g^l_{\alpha'\beta'\nu}}^{(2)}(\mathbf{q},\mathbf{k},\mathbf{k}') \right] \\ \\ \langle i^z \rangle = \frac{\hbar^3 NS}{2A^3} \sum_{\nu l} \sum_{hh'} \sum_{\substack{<\alpha\beta> \\ <\alpha'\beta'>}} \sum_{\mathbf{qkk'},\mathbf{G}} \Gamma_{\nu l}(\mathbf{q},\mathbf{k},\mathbf{k}')\delta_{\mathbf{k}-\mathbf{k}'+\mathbf{q},\mathbf{G}} \\ \mathfrak{Re}\left[{g^l_{\alpha\beta\nu}}^{(1)*}(\mathbf{q},\mathbf{k},\mathbf{k}') g^l_{\alpha'\beta'\nu}{}^{(1)}(\mathbf{q},\mathbf{k},\mathbf{k}') - {g^l_{\alpha\beta\nu}}^{(2)*}(\mathbf{q},\mathbf{k},\mathbf{k}') {g^l_{\alpha'\beta'\nu}}^{(2)}(\mathbf{q},\mathbf{k},\mathbf{k}') \right] \end{cases} \tag{3.10}$$

where

$$\Gamma_{\nu l}(\mathbf{q},\mathbf{k},\mathbf{k}') = \pi \int \frac{d\omega}{2\pi} \int \frac{d\epsilon}{2\pi} \int \frac{d\epsilon'}{2\pi} \delta(\epsilon - \epsilon' + \omega) A^l_\nu(\mathbf{q},\omega) A(k,\epsilon) A(k',\epsilon') \times \left\{ \Big[1 + n_B(\beta_I \omega)\Big] \Big[1 - n_F(\beta_M \epsilon)\Big] n_F(\beta_M \epsilon') - n_B(\beta_I \omega) n_F(\beta_M \epsilon) \Big[1 - n_F(\beta_M \epsilon')\Big] \right\}. \tag{3.11}$$

[3]See details in Appendix C.

Here, Eq. (3.11) reflects the inelastic scattering of $e^- + e^- \rightarrow magnon$ and its reciprocal process in terms of the spectral function for the νth magnon band at the lth layer, $A^l_\nu(\mathbf{q},\omega)$, and the electron spectral function, $A(\mathbf{k},\epsilon)$. For a non-interacting clean system, we have $A^l_\nu(\mathbf{q},\omega) = 2\pi\delta(\omega - \omega^l_\nu(\mathbf{q}))$ and $A(\mathbf{k},\epsilon) = 2\pi\delta(\epsilon - \epsilon_\mathbf{k})$. Assuming the electronic temperature T_M and the single electron energy $\epsilon_\mathbf{k}$ to be both much smaller than the Fermi energy ϵ_F, we treat the electron density of states as a constant $D(\epsilon_F) = D$. Then Eq. (3.11) can be simplified as,

$$\Gamma_{\nu l}(\mathbf{q}) = \pi D^2 \omega^l_{\nu,\mathbf{q}} \left[n_B(\beta_M \omega^l_{\nu,\mathbf{q}}) - n_B(\beta_I \omega^l_{\nu,\mathbf{q}}) \right]. \tag{3.12}$$

When a thermal gradient drives the system into a non-equilibrium state, a local temperature difference between the two subsystems near the interface breaks the detailed balance and generate a longitudinal spin current. Introducing the notation,

$$\mathbf{g} = \left(\frac{g^{(1)} + g^{(2)}}{2}, \frac{i(g^{(1)} - g^{(2)})}{2}, g^{(3)} \right), \tag{3.13}$$

we can express the interfacial spin current density in a more compact way as,

$$\begin{aligned} \mathbf{i} &= i\frac{\hbar^3 NS}{A^3} \sum_{\substack{\nu l \\ hh'}} \sum_{\substack{<\alpha\beta> \\ <\alpha'\beta'>}} \sum_{\mathbf{qkk'},\mathbf{G}} \Gamma_{\nu l}(\mathbf{q},\mathbf{k},\mathbf{k}') \delta_{\mathbf{k}-\mathbf{k}'+\mathbf{q},\mathbf{G}} \\ &\quad \mathbf{g}^l_{\alpha'\beta'\nu}(\mathbf{q},\mathbf{k},\mathbf{k}') \times {\mathbf{g}^l_{\alpha\beta\nu}}^*(\mathbf{q},\mathbf{k},\mathbf{k}'). \end{aligned} \tag{3.14}$$

One may notice that the spin current depends quadratically on $\mathbf{g}'s$ so that simply changing the signs of both interfacial couplings J_{ij} and $\mathbf{D}_{ij}$ will not change the result.

Since rotational invariance of the electron spin at the interface is broken by the magnetic noncollinearity of the insulator, one may notice that, in Eq. (3.6), all four kinds of spin configurations $\sigma\sigma'$ of the two-electron scattering can contribute to a magnon creation. Thus, in spin current expressions the product between two amplitudes will have some cross terms as interference, which is zero in the ferromagnetic or collinear antiferromagnetic case. These cross terms are generally non-zero but small compared to the diagonal terms due to the phase summation. In some cases they may even cancel out from the lattice symmetry.

3.2 Numerical Results

As we introduced in previous chapter, pyrochlore iridates (PI) are $5d$ transition metal oxides with a corner-sharing tetrahedron lattice, where on each vertex sits an Ir^{4+} ion with an effective spin 1/2 [95, 96, 84, 214], as shown in Fig. 3.2. On one hand, pyrochlore iridates have a strong spin-orbital coupling that may give rise to a large DMI both in the bulk and at the interface, on the other hand, the effective spins of pyrochlore iridates arrange in a non-collinear all-in/all-out(AIAO) configuration under large on-site interaction U [166, 43, 159, 42, 45, 115] and they behave as an insulator in this AIAO phase due to strong correlations among electrons [222, 176]. Thus, in order to further study the effects of an interfacial temperature difference, interfacial coupling strength and magnetic non-collinearity on the LSSE, the pyrochlore iridate serves as a good non-collinear magnetic insulator for us to apply the spin

current expression that we developed above into a numerical calculation.

In order to use Eq. (3.12) and Eq. (3.14) to assess the spin current, we need to first evaluate the magnon energy spectrum $\omega^{l}_{\nu,\mathbf{q}}$ and the Bogoliubov transformation coefficients $\{(M^{0l}_{\beta\nu,\mathbf{q}}, N^{0l}_{\beta\nu,-\mathbf{q}})\}$. These quantities can be obtained by diagonalizing the spin Hamiltonian [199, 107] of a bulk PI,

$$\mathcal{H}_m = \sum_{\langle ij \rangle} \mathcal{J} S_i \cdot S_j + \mathcal{D}_{ij} \cdot (S_i \times S_j) + S^a_i \Gamma^{ab}_{ij} S^b_j, \tag{3.15}$$

obtained from a large U expansion. Here, $\mathcal{J}$ and $\mathcal{D}_{ij}$ are the exchange interaction and DMI in the bulk, which can be different from interfacial coupling with the metallic system, and Γ^{ab}_{ij} is the symmetric anisotropic exchange [130].

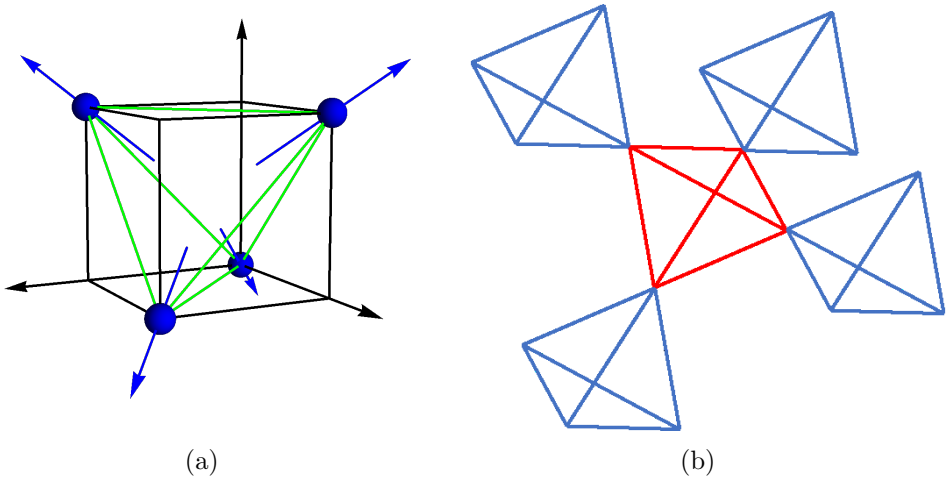

(a) (b)

Figure 3.2: (a) Bulk unit cell in the cubic coordinate system with the AIAO spin configuration. (b) Corner-sharing pyrochlore lattice.

For simplicity, we suppose the metallic side has the same lattice structure as PI and the interfacial coupling has the proper sign (positive $J_{\alpha\beta}$ and

indirect $\mathbf{D}_{\alpha\beta}$ [95, 96]) to favor the AIAO configuration at the interface. In a real material system the interfacial magnetic order may differ from that of the bulk, as may either be determined through first principles calculation or experiment. In that case, one should use the interfacial order in Eq. (3.5). For the units, we choose energy scale in units of t^2/U using the parametrization studied in Refs. [107, 105], and setting $\hbar = 1$, and the lattice constant $a = 1$.

To analyze the interfacial effect, we consider two separate cases where the nonmagnetic ions of PI are grown in different crystalline orientations, [111] and [100], shown in Fig. 3.3.

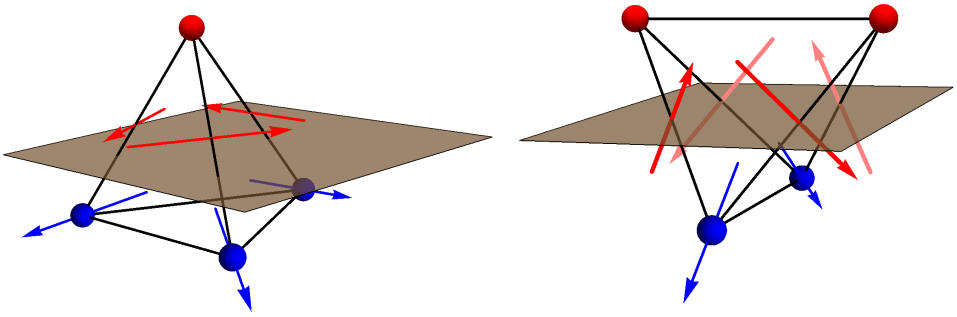

(a) Crystalline Orientation along [111]. (b) Crystalline Orientation along [100].

Figure 3.3: Blue dots are magnetic sites in the insulator and red dots are spin densities localized at metallic lattices. The brown sheet is the interface and the blue arrows indicate the magnetic moments. The red arrows on the red-blue bonds are the indirect DM vectors $\mathbf{D}_{ij}$ between electron spin density $\rho(\mathbf{r}_i)$ and moment $\mathbf{S}_\beta(\mathbf{r}_j)$. Constrained by the symmetry, the DM vector on each bond is parallel to the opposite bond.

Moreover, we count the contribution both from the scattering that $\mathbf{G} = 0$ and other possible Umklapp scattering ($\mathbf{G} \neq 0$). The system size

we use in the numerical summation is a 3-layer$\times 12 \times 12$ lattice to obtain converged results. The dispersion of bulk magnons at the interface calculated from Eq. (3.15) is shown in Fig. 3.4.

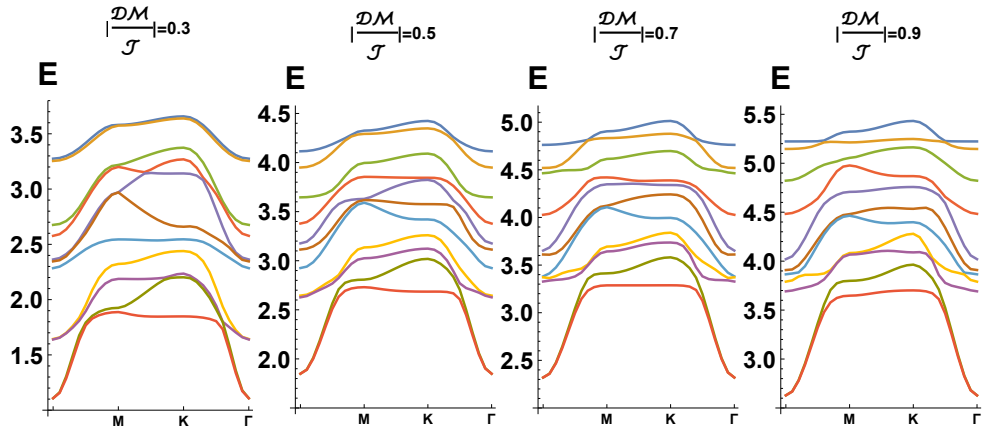

(a) Crystalline orientation along [111].

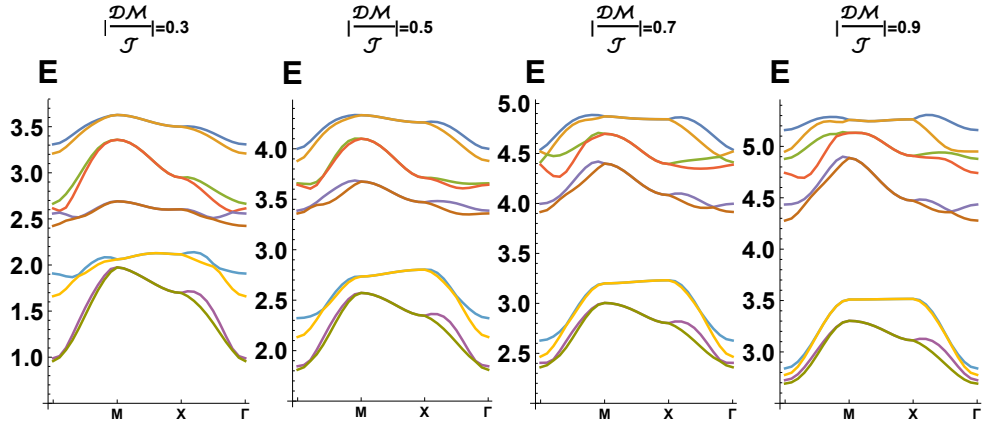

(b) Crystalline orientation along [100].

Figure 3.4: Bulk magnon spectrum along high symmetry directions for different crystalline orientations.

In Fig. 3.5, it shows that the spin current flowing through the [111]

interface is smaller compared to the [100] case, which can be understood as the interfacial total moment in [100] case is larger than the moment in [111] case.

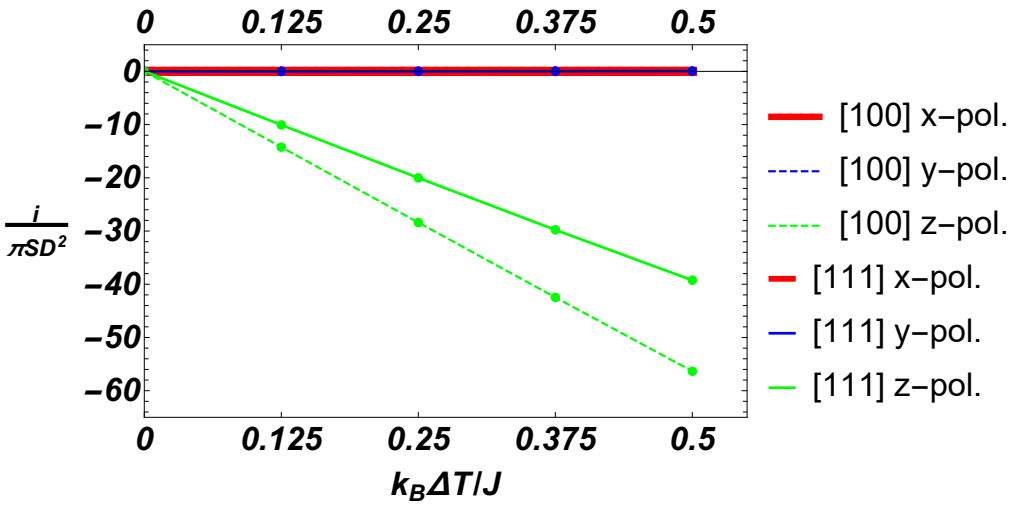

Figure 3.5: Red, blue and green lines represent x, y and z polarization respectively. Solid (dashed) lines represent spin current density when the crystal is oriented in the [111] ([100]) direction. In these two orientation, only the z-polarized spin current density is non-zero (the minus sign means the polarization is along -z) and increases as the temperature difference increases, while i^x and i^y is zero because of the symmetry. Here $k_BT_M = \mathcal{J}, k_BT_I = \mathcal{J} - k_B\Delta T$. $|\mathcal{D}_{ij}|/\mathcal{J} = |\mathbf{D}_{ij}|/J_{ij} = 0.3$. S is the magnitude of the local spin and the effective S=1/2 in the PI.

3.2.1 Temperature Dependence

We set $k_BT_M = \mathcal{J}$ approximately around the transition temperature of PI and calculate the spin current density when $k_BT_I = \mathcal{J}/2, 5\mathcal{J}/8, 3\mathcal{J}/4, 7\mathcal{J}/8, \mathcal{J}$ in order to investigate the dependence on temperature differences. The non-

magnetic ions of PI are usually grown in the [111] direction; thus, there are 3 sublattices at the interface. As previous experimental studies show that $|\mathcal{D}_{ij}|/\mathcal{J} \simeq 0.1 - 0.3$ in the bulk of PI [45], we set this ratio to be 0.3. Although the strength of the interfacial coupling is not necessarily equal to the bulk one, as the temperatures only show up in Eq. (3.12) and thus spin currents will not change the dependence on temperature when changing the interfacial coupling, we simply choose interfacial $J_{ij}, \mathbf{D}_{ij}$ equal to $\mathcal{J}, \mathcal{D}_{ij}$ in the bulk. In both orientations, Fig. 3.5 shows a linear dependence on temperature difference for z-polarized spin current while x- and y-polarized spin current is almost zero. This can be explained with a symmetry consideration that the net magnetic moment only has a non-zero z-component at the interface.

Next, we set the temperature difference $k_B \Delta T = \mathcal{J}/8$ as a constant but change the temperature of the heat bath from $k_B T_M = \mathcal{J}$ to $k_B T_M = \mathcal{J}/8$. We find that the spin current density is larger if the whole system is at a higher temperature, as shown in Fig. 3.6. This comes from the Bose-Einstein statistics of magnons as higher temperature leads to a higher density of magnons participating in the magnon-electron scattering that transfers the spin angular momentum across the interface. However, at high temperature, the magnon-magnon interaction can have a non negligible effects on the scattering which is beyond our present model, and the magnetic order may also changes when the temperature exceeds the transition temperature.

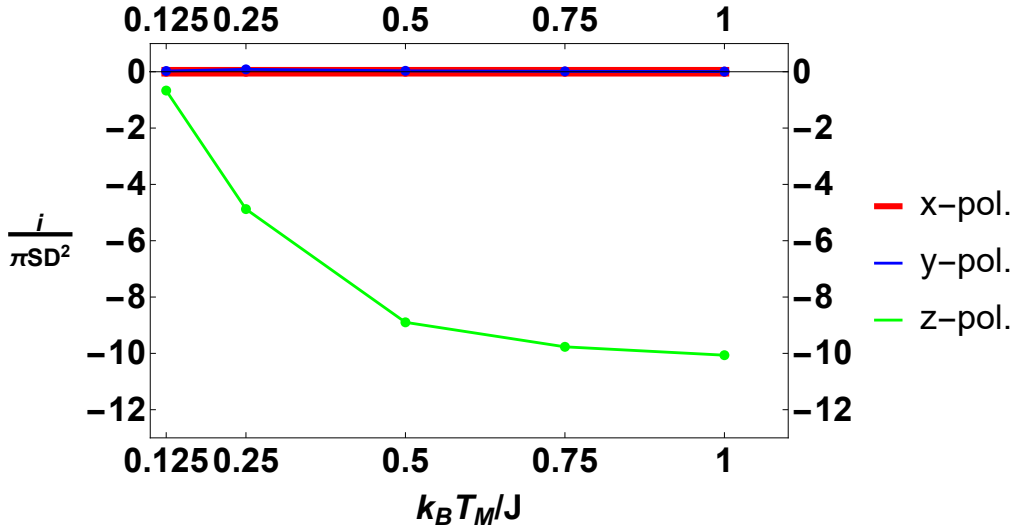

Figure 3.6: Spin current density increases as the temperature of the heat bath T_M increases. Here $k_B\Delta T = k_B T_M - k_B T_I = \mathcal{J}/8$. $|\mathcal{D}_{ij}|/\mathcal{J} = |\mathbf{D}_{ij}|/J_{ij} = 0.3$.

3.2.2 Coupling Strength

Fig. 3.7 shows the effects of the coupling strength on the z-polarized spin current when the crystalline orientation is along [111] and [100]. Here, we set $k_B T_M = 5\mathcal{J}/8$ and $k_B T_I = \mathcal{J}/2$ but change the ratio of the DMI to exchange coupling $|\frac{\mathcal{D}_{ij}}{\mathcal{J}_{ij}}|$ in the bulk and $|\frac{\mathbf{D}_{ij}}{J_{ij}}|$ at the interface. As in Eq. (3.14), the interfacial exchange coupling only appears in $\mathbf{g}$ and $\mathbf{i} \propto J_{ij}^2$. Thus, when $|\frac{\mathbf{D}_{ij}}{J_{ij}}|$ is a constant, the interfacial exchange coupling trivially affects the spin current as a parabolic function of J_{ij}. Therefore, we can simply set the $J_{ij} = \mathcal{J}$ and focus on the behavior of spin currents when changing $|\frac{\mathbf{D}_{ij}}{J_{ij}}|$ and $|\frac{\mathcal{D}_{ij}}{\mathcal{J}_{ij}}|$. Generally, the DMI in the bulk PI increases the excitation energy of magnons, which decreases the spin current. This is shown in Fig. 3.7: the curve with lower $|\frac{\mathcal{DM}}{\mathcal{J}}|$ is above the one with higher DMI, indicating that the bulk DMI

suppresses the spin transport.

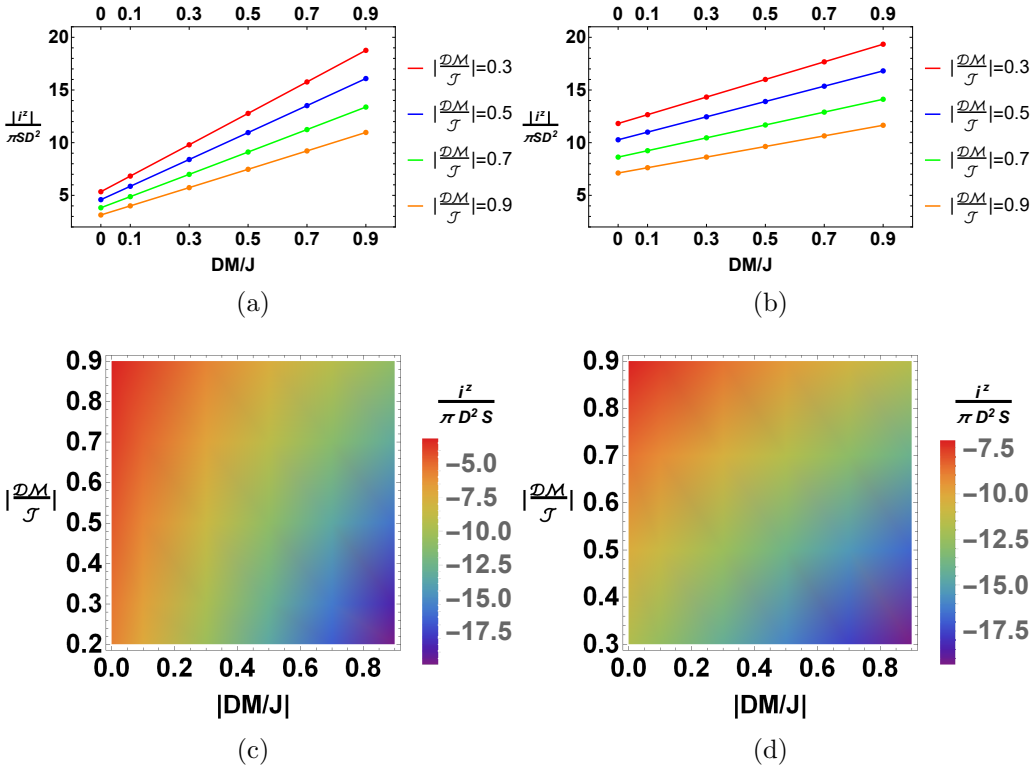

Figure 3.7: The magnitude of z-polarized spin current density/$\pi D^2 S$ as a function of the coupling strength. (a) Crystal oriented in [111] and (b) Crystal oriented in [100]. (c)(d) Corresponding density plots for [111] and [100] orientation. Here $k_B T_M = 5\mathcal{J}/8$ and $k_B T_I = \mathcal{J}/2$, $J_{ij} = \mathcal{J}$, $|\frac{\mathcal{DM}}{\mathcal{J}}|$ is the coupling ratio in the bulk and $|\frac{\mathbf{DM}}{J}|$ is the coupling ratio at the interface. S is the magnitude of the local spin and the effective S=1/2 in PI.

One can also see that the spin current has a linear dependence on the interfacial DMI in Fig. 3.7. To further analyze the effect of interfacial DMI, we consider a FM spin alignment (non-physical, but illustrative) on the pyrochlore lattice, where the magnetic moments are coupled with only

exchange interaction $\mathcal{J} < 0$ in the bulk and align along transport direction (z-direction), while we turn on a DMI at the interface assuming the DM vectors are the same with previous AIAO configuration.

As shown in Fig. 3.8, only the z-polarized spin currents are non-zero in both cases but the dependence on the interfacial DMI are unlike each other and unlike the curves in Fig. 3.7. This difference comes from the relative angles among the magnetic moments, the DM vectors, and the polarization direction. Since the interference is small, if we ignore the cross terms in Eq. (3.14), the spin current density can be simplified as,

$$\begin{aligned}\mathbf{i} \;&= \frac{\hbar^3 N}{A^3} \sum_{\mathbf{qk},\mathbf{G}} \sum_{\alpha\beta} \sum_{\nu l} \Gamma_{\nu l}(\mathbf{q}, \mathbf{k}, \mathbf{k}+\mathbf{q}-\mathbf{G}) \Lambda^{l}_{\beta\nu}(\mathbf{q}) \\ &\quad \left[\mathbf{D}_{\alpha\beta} \left(\mathbf{S}_\beta \cdot \mathbf{D}_{\alpha\beta}\right) + J_{\alpha\beta} \left(\mathbf{D}_{\alpha\beta} \times \mathbf{S}_\beta\right) + J^2_{\alpha\beta} \mathbf{S}_\beta\right], \end{aligned} \tag{3.16}$$

where $\Lambda^{l}_{\beta\nu}(\mathbf{q}) = \frac{1}{2}\left(|M^{0l}_{\beta\nu,\mathbf{q}}|^2 - |N^{0l}_{\beta\nu,-\mathbf{q}}|^2\right)$.

As it can be seen from Eq. (3.16), the spin current density is generally parabolic with respect to the interfacial DMI. The third term within the bracket is the contribution from the isotropic coupling and is quadratic in the exchange coupling strength [52], while the first two terms arise from the interfacial DMI. Since the DMI can be understood as the super-exchange interaction with the help of spin-orbital coupling in a microscopic picture [130], the total spin is not conserved at the interface. The new contributions come from the orbital moment of the ion. In the case of the AIAO spin configuration, the magnetic moment $\mathbf{S}_\beta$ is perpendicular to the corresponding DM vectors leading the first term to be zero and giving rise a linear dependence.

Moreover, the indirect DM vectors in the AIAO state turn out to lead to an enhancement of spin current in the second term, as shown in Fig. 3.7.

In the ferromagnetic cases, when the crystal is oriented in [111], both $\mathbf{S}_\beta \cdot \mathbf{D}_{\alpha\beta} = 0$ and $\left[\mathbf{S}_\beta \times \mathbf{D}_{\alpha\beta}\right]_z = 0$, which results in the DMI not affecting the spin current in Fig. 3.8(a). However, $\mathbf{S}_\beta$ is not perpendicular to $\mathbf{D}_{\alpha\beta}$ anymore if the orientation is in [100] and this will give a parabolic curve, as seen in Fig. 3.8(b). More specifically,

$$\sum_{\alpha\beta} \Lambda^l_{\beta\nu} \left[\mathbf{D}_{\alpha\beta} \left(\mathbf{S}_\beta \cdot \mathbf{D}_{\alpha\beta}\right)\right]_z = \sum_{\alpha\beta} \frac{1}{2} |M^{0l}_{\beta\nu,\mathbf{q}}|^2 S_\beta {D^z_{\alpha\beta}}^2 \tag{3.17}$$

is always postive and

$$\sum_{\alpha\beta} \Lambda^l_{\beta\nu} J_{\alpha\beta} \left[\mathbf{D}_{\alpha\beta} \times \mathbf{S}_\beta\right]_z = JS\Lambda^l_{1(2)\nu} \sum_{\alpha} \left[\mathbf{D}_{\alpha,1} \times \hat{z} + \mathbf{D}_{\alpha,2} \times \hat{z}\right]_z = 0 \tag{3.18}$$

because of the mirror symmetry of the lattice (where $\Lambda^l_{1\nu} = \Lambda^l_{2\nu}$ and $\mathbf{D}_{\alpha,1} + \mathbf{D}_{\alpha,1} \perp \hat{z}$). This leads to a parabola opening up and centered at zero as shown in Fig. 3.8(b).

Therefore, not only the spin orientation at the interface but also the directions of interfacial DM vectors can affect the interfacial spin current. Whether the interfacial DMI will enhance or suppress the spin transfer depends on the details of interfacial orbital moments and Eq. (3.16) can be used to theoretically investigate the effects.

3.3 Discussion and Conclusions

In this work, we extend the theory of spin transport driven by thermal gradient at the interface of a noncollinear magnetic insulator|normal metal heterostructures [52], deriving a general expression for the spin current density when both exchange coupling and Dzyaloshinskii–Moriya interaction are present at the interface. Our theory, which neglects magnon-magnon interactions, is valid at temperatures much below the magnetic ordering temperatures. We numerically calculate the spin current density to study the effects of temperature difference, coupling strength and crystalline orientation using pyrochlore iridates with the AIAO state as the magnetic insulator. We derive an approximate equation to investigate the effects of DM vectors on spin currents and use it to explain the numerical results when the PI is in the AIAO state and the ferromagnetic state. These results give theoretical guidance to manufacturing practical spintronic devices and optimizing the spin transfer across the interface.

Experimentally, the LSSE is detected by the transverse voltage induced from the inverse spin Hall effects [160, 188, 99, 184]. Our result of interfacial spin currents can then be used as a boundary condition to solve the transport equation for spin diffusion and find the spin currents in the bulk of the metal [170]. Making use of experimental data, one can theoretically evaluate the spin Hall angle and investigate different microscopic models on spin-current conversion. This could provide a better description of the relation between the bulk spin Hall angle and the interface properties which may influence the

value of the spin Hall angle extracted in inverse spin Hall measurements.

While here we focus on the spin transport due to magnon-electron scattering, thermalized phonons could also contribute to the scattering [2, 1, 51, 94]. Future work should evaluate the correction to the phonon-dressed magnons. As the LSSE is a non-equilibrium phenomenon, the interplay between the higher order magnons and the spin accumulation near the metallic interface should be considered. Moreover, in Sec. 3.2, we simply treat the interfacial spin configuration and DM vectors as being the same as those in the bulk of the material. However, the lattices of the two systems may not match with each other as we have assumed and the physics at the interface may be more complicated. A first-principle calculation on magnetic canting and orbital moments can be useful to lead to a more realistic result, still within the framework of our theory. In addition, the asymmetry of the interface can give rise to a Rashba-type coupling and Dresselhaus SOC which may introduce Skyrmions near the interface [50, 11, 156]. These effects should be investigated in future work.

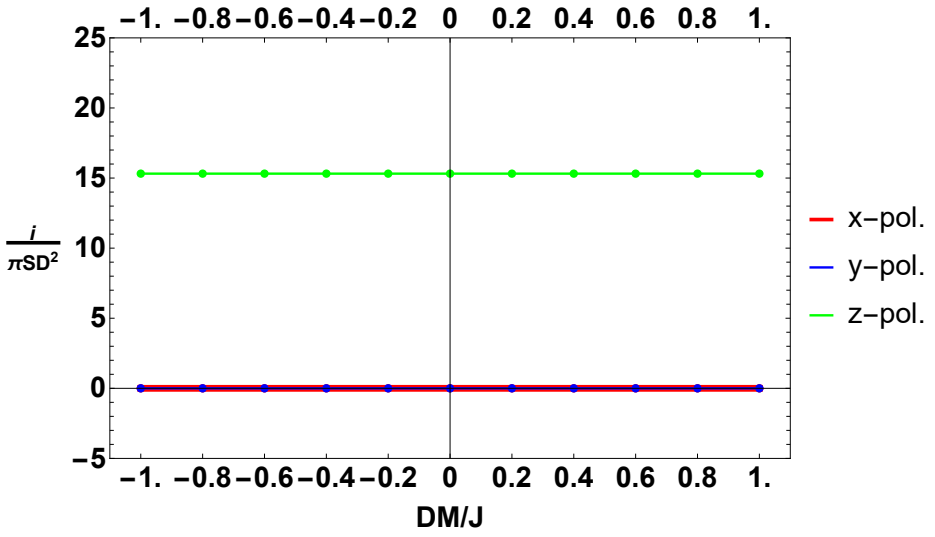

(a) Crystalline Orientation along [111].

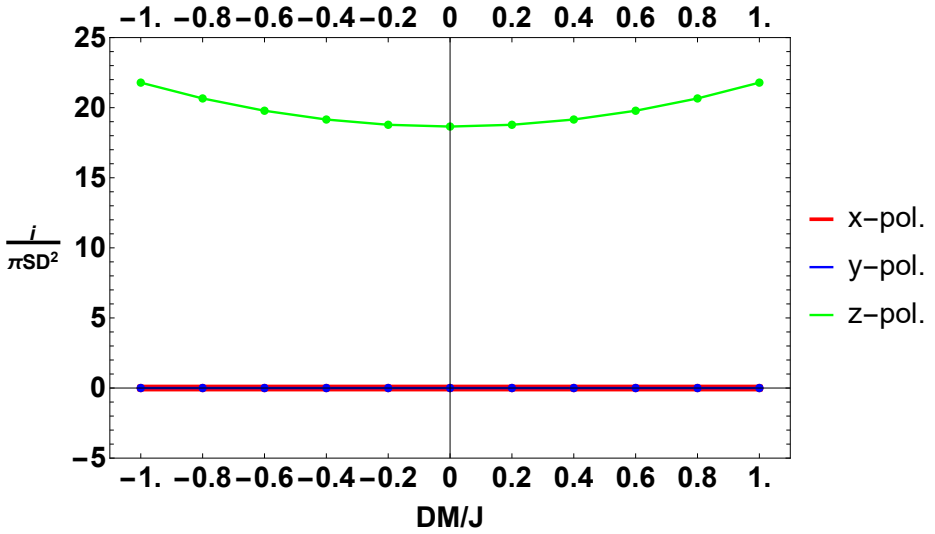

(b) Crystalline Orientation along [100].

Figure 3.8: Spin current density induced by ferromagnetic moments on PI lattice. In these two orientations, the configurations of interfacial DM vectors are the same with the DM vectors in the AIAO state and we allow the interfacial exchange coupling to be either ferromagnetic ($J < 0$) or antiferromagnetic ($J > 0$).

Chapter 4

Topological Magnon-Polaron in Two-dimensional Antiferromagnets

In this chapter[1] ,we theoretically study magnon-phonon hybrid excitations, i.e.,magnon-polarons, in a two-dimensional antiferromagnet on a honeycomb lattice. Antiferromagnetic materials have recently attracted great attention to the community of spintronics [81, 80, 10], as they are insensitive to the perturbation of magnetic fields and have no stray field with fast magnetic dynamics in a timescale at THz comparing to ferromagnets with a frequency of GHz. Many research efforts have been conducted over the past decade on spin dynamics and spin transports in antiferromagnets, such as spin-transfer torques [31, 59], domain-wall motions [60], and spin Seebeck effects [201, 138, 155]. In particular, magnons, as collective excitations emerging from magnetic orders, have low-dissipation and allow a pure spin transport without Joule heating, leading to a surge of interest in utilizing magnons for spintronics. Many magnonic analogs of electronic phenomena, such as magnon thermal

[1]The results presented here are based on the research article: Bowen Ma and Gregory A. Fiete, *Dzyaloshinskii-Moriya Induced Topological Magnon-Phonon Hybridization in 2D Antiferromagnetic Insulators with Tunable Chern Numbers*, arXiv: 2107.11484 (2021). B. Ma suggested the project, performed the calculations, and wrote the computer code. G. A. Fiete supervised the project. Both authors participated in discussions, and in writing the manuscript.

Hall effects [91, 139, 125], magnon Nernst effects [30, 223, 169], and magnonic Edelstein effects [111, 213], have been theoretically studied and experimentally observed.

Along with magnonics, there is also a potential application in spintronics by combining magnetic orders with non-trivial topology [172]. The topologically protected states are usually robust and weakly affected by disorders. It can provide high charge-to-spin conversion efficiency [192], strong magnetoresistance [194, 114] and possess a number of exotic phenomena such as quantum anomalous Hall effects [26, 39] and chiral Majorana fermions [67]. In addition to fermionic topological excitations, there is also an emerging field of investigating topological bosonic excitations, such as topological magnons [218, 127, 32, 113] and topological phonons [150, 217, 77]. Moreover, some recent works have shown topological properties in hybridized systems between magnons and acoustic phonons with the magnetoelastic coupling [58, 219], the Dzyaloshinskii–Moriya (DM) interaction [220], or the dipolar coupling [177]. However, a study for the coupling between magnons and optical phonons is still lacking.

In this chapter, we try to complement prior work by study magnon-phonon hybrid excitations in a 2D collinear antiferromagnetic insulator (AFI) on a honeycomb lattice. The coupling is originated from an in-plane nearest-neighbor DMI by mirror symmetry breaking [40, 175, 151], which can be generically achieved in 2D van der Waals heterostructures. Since antiferromagnets naturally possess at least two sublattices, it is possible to realize the coupling

between magnons and optical phonons. In Sec. 4.1, we introduce the model with both spin and lattice dynamics, and derive the interaction between them arising from the DMI. In Sec. 4.2, we find finite Berry curvature and non-zero Chern numbers with couplings between magnons and optical phonons. We also show that the Chern numbers of magnon-polaron bands can be manipulated by an external magnetic field. In Sec. 4.3, We evaluate the thermal Hall conductivity and propose spin-induced valley Hall effects as a possible experimental observation. We emphasize our results are generic to any lattice structures and can be easily generalized into 3D systems as discussed in Sec. 4.4 at the end of the chapter. Our work suggests antiferromagnets with multiple sublattices in comparison to ferromagnets serve as promising platforms to realize tunable topological excitations hybridizing magnons with both acoustic and optical phonons, where the topology of the bands can provide robust information transport and may find possible applications in spintronics.

4.1 Model

We consider a system with collinear AFI Néel order on a honeycomb lattice, where the magnetic moments are perpendicular to the plane, i.e., $\mathbf{S}_{A,B} = \pm S\hat{\mathbf{z}}$ for the A and B sublattices respectively [see Fig. 4.1(a)]. The Hamiltonian describing both spin and lattice degree of freedoms can be written as

$$H = H_p + H_m + H_{mp}, \tag{4.1}$$

where $H_p,\ H_m,\ H_{mp}$ stands respectively for phonon Hamiltonian, spin Hamiltonian and the interaction between them. The interaction part is a result of in-plane nearest-neighbor DMI originated from mirror symmetry breaking. In equilibrium, it couples neighboring spins as

$$H_D = \mathbf{D}_{ij} \cdot (\mathbf{S}_i \times \mathbf{S}_j). \tag{4.2}$$

where $\mathbf{D}_{ij}$ is the DM vector for bond ij, and by Moriya's rule [130, 131], it is in the plane and perpendicular to the bond, i.e., $\mathbf{D}_{ij} \propto \hat{\mathbf{z}} \times \mathbf{R}_{ij}$ [see Fig. 4.1(b)].

This DMI which is perpendicular to spin moments does not present in the linear spin-wave Hamiltonian [91, 220], though it can be significant for determining the ground state. Here we assume it does not appreciably change (i.e., the change is numerically small) the Néel ground order as long as the exchange coupling and anisotropy are large enough. However, both magnitude and direction of $\mathbf{D}_{ij}$ implicitly depend on $\mathbf{R}_{ij}$ and thus it couples the spin degree of freedom with lattice dynamics. In the following, we give detailed modelings on each term and find the matrix representation of the Hamiltonian under second quantized operators.

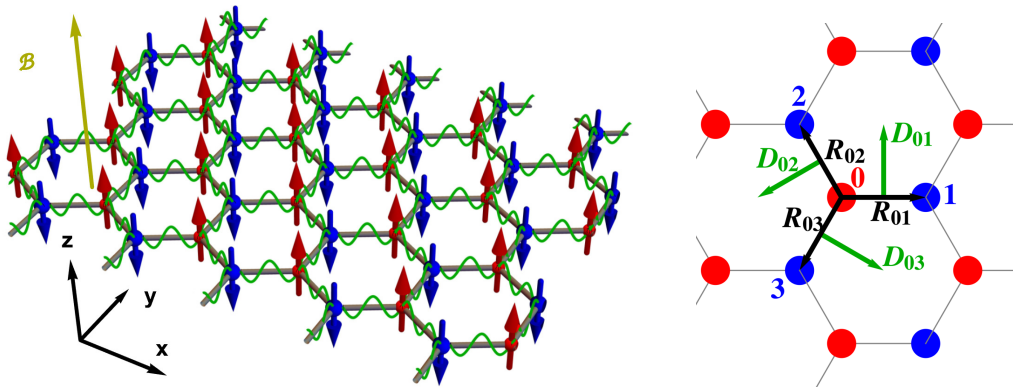

(a) (b)

Figure 4.1: (a) The schematic illustration of the hybrid magnon-phonon system. The ground state of the magnetization is Néel order along the z axis (red and blue arrows, color denoting the A and B sublattices). (b) DM vectors (green arrows) for the nearest bonds originated from mirror symmetry $\mathcal{M}_{yz}$ breaking.

4.1.1 Elastic Hamiltonian

We begin from the stretch between site i and j away from their equilibrium positions $\mathbf{R}_{ij}^0$ by a small displacement $\mathbf{u}_{ij} = \mathbf{u}_j - \mathbf{u}_i$ as

$$\begin{aligned} |\Delta\mathbf{R}_{ij}| &= |\mathbf{R}_{ij}| - |\mathbf{R}_{ij}^0| = \sqrt{(\mathbf{R}_{ij}^0 + \mathbf{u}_{ij})^2} - |\mathbf{R}_{ij}^0| \\ &= |\mathbf{R}_{ij}^0| \sqrt{1 + 2\frac{\mathbf{R}_{ij}^0 \cdot \mathbf{u}_{ij}}{|\mathbf{R}_{ij}^0|^2} + \mathbf{u}_{ij}^2} - |\mathbf{R}_{ij}^0| \approx \hat{\mathbf{R}}_{ij}^0 \cdot \mathbf{u}_{ij}. \end{aligned} \tag{4.3}$$

Therefore, to the lowest order, only in-plane displacement along bond ij presents in the elastic Hamiltonian, and thus we focus on $\mathbf{u} = (x,\ y)$ in the following. By Hooke's law, the phonon part H_p can be expressed to the lowest

order with nearest-neighbor and next-nearest-neighbor couplings as

$$H_p = \sum_i \frac{\mathbf{p}_i^2}{2m_i} + \frac{k_1}{2}\sum_{\langle ij\rangle}(\hat{\mathbf{R}}_{ij}^0 \cdot \mathbf{u}_{ij})^2 + \frac{k_2}{2}\sum_{\langle\langle ij\rangle\rangle}(\hat{\mathbf{R}}_{ij}^0 \cdot \mathbf{u}_{ij})^2, \tag{4.4}$$

where m_i is the mass of atom i, and k_1 (k_2) is the spring constant that corresponds to the elastic energy between two (next) nearest neighbor atoms. As we are interested in the interaction between spin and lattice dynamics, we only take the atoms A and B with moments into account. For simplicity without loss of generality, we assume $m_A = m_B = M$.

In the position-momentum space, the displacement $\mathbf{u}_i$ can be Fourier transformed as

$$\mathbf{u}_i = \frac{1}{\sqrt{N}}\sum_{\mathbf{k}} u_{\mathbf{k}} e^{i\mathbf{k}\cdot\mathbf{R}_i}, \tag{4.5}$$

and its conjugated momentum as

$$\mathbf{p}_i = \frac{1}{\sqrt{N}}\sum_{\mathbf{k}} p_{-\mathbf{k}} e^{-i\mathbf{k}\cdot\mathbf{R}_i}, \tag{4.6}$$

where N is the number of unit cell. With Eq. (4.5) and (4.6), H_p in k-space has a form as

$$H_p(\mathbf{k}) = \begin{bmatrix} \frac{1}{2}D(\mathbf{k}) & 0 \\ 0 & \frac{\jmath_4}{2M} \end{bmatrix}, \tag{4.7}$$

under the basis $(x_A(\mathbf{k}),\ y_A(\mathbf{k}),\ x_B(\mathbf{k}),\ y_B(\mathbf{k}),\ p_A^x(\mathbf{k}),\ p_A^y(\mathbf{k}),\ p_B^x(\mathbf{k}),\ p_B^y(\mathbf{k}))^T$, where $D(\mathbf{k})$ is the dynamical matrix that has been used a lot in studying lattice dynamics. For a honeycomb lattice,

$$D(\mathbf{k}) = \begin{bmatrix} D_{AA}(\mathbf{k}) & D_{AB}(\mathbf{k}) \\ D_{BA}(\mathbf{k}) & D_{BB}(\mathbf{k}) \end{bmatrix}, \tag{4.8}$$

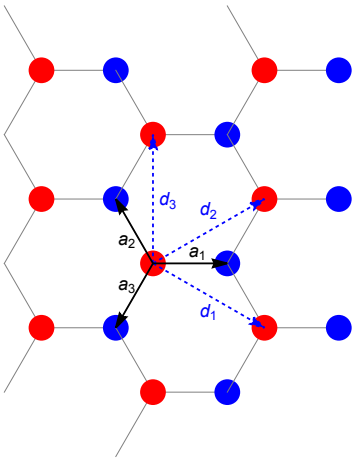

Figure 4.2: Honeycomb lattice structure. Red and blue spheres are A and B sublattices respectively.

where

$$D_{AA}(\mathbf{k}) = D_{BB}(\mathbf{k}) = \begin{bmatrix} \frac{3k_1}{2} + 3k_2\left(1 - \cos\frac{3k_x a}{2}\cos\frac{\sqrt{3}k_y a}{2}\right) & \sqrt{3}k_2 \sin\frac{3k_x a}{2}\sin\frac{\sqrt{3}k_y a}{2} \\ \sqrt{3}k_2 \sin\frac{3k_x a}{2}\sin\frac{\sqrt{3}k_y a}{2} & \frac{3k_1}{2} + k_2\left(3 - \cos\frac{3k_x a}{2}\cos\frac{\sqrt{3}k_y a}{2} - 2\cos\sqrt{3}k_y a\right) \end{bmatrix}, \tag{4.9}$$

and

$$D_{BA}(\mathbf{k}) = D^{\dagger}_{AB}(\mathbf{k}) = \begin{bmatrix} -\frac{1}{2}k_1 e^{\frac{ik_x a}{2}}\left(\cos\frac{\sqrt{3}}{2}k_y a + 2e^{-i\frac{3k_x a}{2}}\right) & -i\frac{\sqrt{3}}{2}k_1 e^{\frac{ik_x a}{2}}\sin\frac{\sqrt{3}k_y a}{2} \\ -i\frac{\sqrt{3}}{2}k_1 e^{\frac{ik_x a}{2}}\sin\frac{\sqrt{3}k_y a}{2} & -\frac{3}{2}k_1 e^{\frac{ik_x a}{2}}\cos\frac{\sqrt{3}k_y a}{2} \end{bmatrix}. \tag{4.10}$$

Here the coordinates are used with the choice of lattice basis vectors $\mathbf{a}_1 = a(1,0),\ \mathbf{a}_2 = a(-1/2, \sqrt{3}/2),\ \mathbf{a}_3 = a(-1/2, -\sqrt{3}/2)$ as shown in Fig. 4.2.

4.1.2 Spin Hamiltonian

The magnetic part H_m is given by

$$H_m = J_1 \sum_{\langle ij \rangle} \mathbf{S}_i \cdot \mathbf{S}_j - J_2 \sum_{\langle\langle ij \rangle\rangle} \mathbf{S}_i \cdot \mathbf{S}_j - \frac{K_z}{2} \sum_i (S_i^z)^2 - \mathcal{B} \sum_i S_i^z, \tag{4.11}$$

where J_1 (J_2) > 0 is the (next-)nearest-neighbor antiferromagnetic (ferromagnetic) Heisenberg exchange coupling, $K_z > 0$ is the easy-axis anisotropy and $\mathcal{B} = g\mu_B B$ is the external effecitve magnetic field. With Holstein-Primakoff transformation, i.e.,

$$\begin{cases} S_{A,i}^+ = S_{A,i}^x + iS_{A,i}^y = \sqrt{2S - a_i^\dagger a_i}\, a_i \approx \sqrt{2S} a_i \\ S_{A,i}^- = S_{A,i}^x - iS_{A,i}^y = a_i^\dagger \sqrt{2S - a_i^\dagger a_i} \approx \sqrt{2S} a_i^\dagger \\ S_{A,i}^z = S - a_i^\dagger a_i \end{cases}, \tag{4.12}$$

$$\begin{cases} S_{B,j}^+ = S_{B,j}^x + iS_{B,j}^y = b_j^\dagger \sqrt{2S - b_j^\dagger b_j} \approx \sqrt{2S} b_j^\dagger \\ S_{B,j}^- = S_{B,j}^x - iS_{B,j}^y = \sqrt{2S - b_j^\dagger b_j}\, b_j \approx \sqrt{2S} b_j \\ S_{B,j}^z = -S + b_j^\dagger b_j \end{cases}, \tag{4.13}$$

Eq. (4.11) can be re-written as

$$\begin{aligned} H_m = {} & J_1 S \sum_{\langle ij \rangle} (a_i b_j + a_i^\dagger b_j^\dagger + a_i^\dagger a_i + b_j^\dagger b_j) \\ & - J_2 S \sum_{\langle\langle ii' \rangle\rangle} (a_i^\dagger a_{i'} + a_{i'}^\dagger a_i - a_i^\dagger a_i - a_{i'}^\dagger a_{i'}) \\ & - J_2 S \sum_{\langle\langle jj' \rangle\rangle} (b_j^\dagger b_{j'} + b_{j'}^\dagger b_j - b_j^\dagger b_j - b_{j'}^\dagger b_{j'}) \\ & + \left(\mathcal{B} - \frac{K_z(1-2S)}{2} \right) \sum_i a_i^\dagger a_i - \left(\mathcal{B} + \frac{K_z(1-2S)}{2} \right) \sum_j b_j^\dagger b_j. \end{aligned} \tag{4.14}$$

With Fourier transform using the convention

$$a_i = \frac{1}{\sqrt{N}} \sum_{\mathbf{k}} a_i e^{i\mathbf{k}\cdot\mathbf{R}_i}, \tag{4.15}$$

$$b_j = \frac{1}{\sqrt{N}} \sum_{\mathbf{k}} b_j e^{i\mathbf{k}\cdot\mathbf{R}_j}, \tag{4.16}$$

we obtain the expression for H_m with basis $(a_{\mathbf{k}}, b_{\mathbf{k}}, a^{\dagger}_{-\mathbf{k}}, b^{\dagger}_{-\mathbf{k}})^T$ as

$$H_m(\mathbf{k}) = \frac{1}{2} \begin{bmatrix} A_m(\mathbf{k}) & B_m(\mathbf{k}) \\ B^*_m(-\mathbf{k}) & A^*_m(-\mathbf{k}) \end{bmatrix}, \tag{4.17}$$

where

$$A_m(\mathbf{k}) = S \begin{bmatrix} 3J_1 + 2J_2 f(\mathbf{k}) + K_z\left(1 - \frac{1}{2S}\right) + \frac{\mathcal{B}}{S} & 0 \\ 0 & 3J_1 + 2J_2 f(\mathbf{k}) + K_z\left(1 - \frac{1}{2S}\right) - \frac{\mathcal{B}}{S} \end{bmatrix} \tag{4.18}$$

with $f(\mathbf{k}) = 3 - \sum_i \cos(\mathbf{k}\cdot\mathbf{d}_i)$ and

$$B_m(\mathbf{k}) = S \begin{bmatrix} 0 & J_1 \sum_i e^{i\mathbf{k}\cdot\mathbf{a}_i} \\ J_1 \sum_i e^{-i\mathbf{k}\cdot\mathbf{a}_i} & 0 \end{bmatrix}. \tag{4.19}$$

4.1.3 Magnon-Phonon Coupling

In this subsection, we derive H_{mp} of Eq. (4.1) from H_D of Eq. (4.2). As $\mathbf{D}_{ij} \propto \hat{\mathbf{z}} \times \mathbf{R}_{ij}$, we can determine DM vectors to be $\mathbf{D}_{ij} = D(\mathbf{R}_{ij})\hat{\mathbf{z}} \times \hat{\mathbf{R}}_{ij}$ (D can be positive or negative for parallel or anti-parallel). Then the DMI between A-sublattice i and B-sublattice j can be written as

$$\begin{aligned} \mathbf{D}_{ij} \cdot (\mathbf{S}_i \times \mathbf{S}_j) &= D(\mathbf{R}_{ij})(\hat{\mathbf{z}} \times \hat{\mathbf{R}}_{ij}) \cdot (\mathbf{S}_i \times \mathbf{S}_j) \\ &= D(\mathbf{R}_{ij}) \left[(\hat{\mathbf{z}} \cdot \mathbf{S}_i)(\hat{\mathbf{R}}_{ij} \cdot \mathbf{S}_j) - (\hat{\mathbf{z}} \cdot \mathbf{S}_j)(\hat{\mathbf{R}}_{ij} \cdot \mathbf{S}_i) \right] \\ &= SD(\mathbf{R}_{ij})\hat{\mathbf{R}}_{ij} \cdot (\mathbf{S}_i + \mathbf{S}_j) \\ &= SD(\mathbf{R}^0_{ij} + \mathbf{u}_{ij})(\hat{\mathbf{R}}^0_{ij} + \hat{\mathbf{u}}_{ji}) \cdot (\mathbf{S}_i + \mathbf{S}_j), \end{aligned} \tag{4.20}$$

where we use relation $(\mathbf{A}\times\mathbf{B})\cdot(\mathbf{C}\times\mathbf{D}) = (\mathbf{A}\cdot\mathbf{C})(\mathbf{B}\cdot\mathbf{D}) - (\mathbf{A}\cdot\mathbf{D})(\mathbf{B}\cdot\mathbf{C})$ and $\hat{\mathbf{z}}\cdot\mathbf{S}_{i(j)} = \pm S$.

To the lowest order with in-plane $\mathbf{u}_{ij}$,

$$D(\mathbf{R}^0_{ij}+\mathbf{u}_{ij}) \approx D(\mathbf{R}^0_{ij}) + \mathbf{u}_{ij}\cdot\nabla D = D(\mathbf{R}^0_{ij}) + \frac{dD}{dR}\hat{\mathbf{R}}^0_{ij}\cdot\mathbf{u}_{ij} + \frac{dD}{Rd\theta}\hat{\theta}_{ij}\cdot\mathbf{u}_{ij}, \tag{4.21}$$

$$\hat{\mathbf{R}}^0_{ij} + \hat{\mathbf{u}}_{ji} = \frac{\mathbf{R}^0_{ij}+\mathbf{u}_{ij}}{|\mathbf{R}^0_{ij}+\mathbf{u}_{ij}|} \approx \frac{\mathbf{R}^0_{ij}+\mathbf{u}_{ij}}{|\mathbf{R}^0_{ij}|}\left(1 - \frac{\mathbf{R}^0_{ij}\cdot\mathbf{u}_{ij}}{|\mathbf{R}^0_{ij}|^2}\right). \tag{4.22}$$

Combining Eq. (4.21) and (4.22) into Eq. (4.20), we have

$$\begin{aligned}\mathbf{D}_{ij}\cdot(\mathbf{S}_i\times\mathbf{S}_j) &= SD(\mathbf{R}^0_{ij})\mathbf{R}^0_{ij}\cdot(\mathbf{S}_i+\mathbf{S}_j)\\ &+ \frac{SD(\mathbf{R}^0_{ij})}{|\mathbf{R}^0_{ij}|}\left[\mathbf{u}_{ij} - (1+\gamma_1)\hat{\mathbf{R}}^0_{ij}\left(\hat{\mathbf{R}}^0_{ij}\cdot\mathbf{u}_{ij}\right) + \gamma_2\hat{\mathbf{R}}^0_{ij}\left(\hat{\theta}_{ij}\cdot\mathbf{u}_{ij}\right)\right]\cdot(\mathbf{S}_i+\mathbf{S}_j),\end{aligned} \tag{4.23}$$

where $\gamma_1 = -\frac{d\ln D}{d\ln R}$ and $\gamma_2 = \frac{d}{d\theta}\ln D$.

The first term in Eq. (4.23) is the zeroth-order term and it does not present in linear spin-wave Hamiltonian as we mentioned earlier, while the second term couples local spins with lattice displacements. If we take $\gamma_1 = \gamma_2 = 0$ which is reasonably small for tiny displacements, it reduces to

$$\begin{aligned}H_{mp} &\approx \frac{DS}{a}\sum_{\langle ij\rangle}\mathbf{u}_{ij}\left[\mathcal{I}_2 - \hat{\mathbf{R}}^0_{ij}\hat{\mathbf{R}}^0_{ij}\right]\left(\tilde{\mathbf{S}}_{A,i}+\tilde{\mathbf{S}}_{B,j}\right)\\ &= \frac{DS}{a}\sum_{\langle ij\rangle}\left(\hat{\mathbf{R}}^0_{ij}\times\mathbf{u}_{ij}\right)\cdot\left[\hat{\mathbf{R}}^0_{ij}\times(\mathbf{S}_{A,i}+\mathbf{S}_{B,j})\right],\end{aligned} \tag{4.24}$$

where $D = |\mathbf{D}_{ij}|$ is the magnitude of the DMI in equilibrium, $a = |\mathbf{R}^0_{ij}|$ is the bond length, $\mathcal{I}_2$ is the 2×2 identity matrix, $\hat{\mathbf{R}}^0_{ij}\hat{\mathbf{R}}^0_{ij}$ is the Kronecker product between two $\hat{\mathbf{R}}^0_{ij}$'s and $\tilde{\mathbf{S}}_{A(B),i} = (S^x_{A(B),i},\ S^y_{A(B),i})$. The second equation

mimics a Rashba-type spin-orbital coupling [25, 122] or a Raman spin–phonon interaction [217, 164, 82, 193], which has been studied in topological aspects of spin or phonon systems. If we take a arbitrarily small,

$$\begin{aligned} H_{mp} &= \frac{DS}{a}\sum_{\langle ij\rangle}\left(\hat{\mathbf{R}}^0_{ij}\times\mathbf{u}_{ij}\right)\cdot\left[\hat{\mathbf{R}}^0_{ij}\times(\mathbf{S}_{A,i}+\mathbf{S}_{B,j})\right] \\ &= \frac{DS}{2a}\sum_{ij}\left(\hat{\mathbf{R}}^0_{ij}\times\mathbf{u}_{ij}\right)\cdot\left[\hat{\mathbf{R}}^0_{ij}\times(\mathbf{S}_{A,i}+\mathbf{S}_{B,j})\right] \\ &+ \frac{DS}{2a}\sum_{ij}\left(\hat{\mathbf{R}}^0_{ji}\times\mathbf{u}_{ji}\right)\cdot\left[\hat{\mathbf{R}}^0_{ji}\times(\mathbf{S}_{A,j}+\mathbf{S}_{B,i})\right] \\ &= DS^2\sum_{ij}\left(\hat{\mathbf{R}}^0_{ij}\times\frac{\mathbf{u}_j-\mathbf{u}_i}{a}\right)\cdot\left[\hat{\mathbf{R}}^0_{ij}\times\left(\frac{\mathbf{S}_{A,i}-\mathbf{S}_{B,i}}{2S}-\frac{\mathbf{S}_{A,j}-\mathbf{S}_{B,j}}{2S}\right)\right] \qquad (4.25) \\ &\approx -\frac{DS^2}{V}\int dV\,[\nabla\times\mathbf{u}(\mathbf{r})]\cdot[\nabla\times\mathbf{n}(\mathbf{r})]\,, \qquad (4.26) \end{aligned}$$

where $\mathbf{u}(\mathbf{r})$ is the displacement field and $\mathbf{n}(\mathbf{r})=\frac{\mathbf{S}_A-\mathbf{S}_B}{2S}$ is the staggered spin field. This is indeed has a similar form to Rashba spin-orbital coupling as $\alpha_R\mathbf{E}\cdot(\mathbf{p}\times\boldsymbol{\sigma})$ or Raman spin-phonon coupling as $\mathbf{h}\cdot(\mathbf{p}\times\mathbf{u})$.

It is clear from Eq. (4.24) that this DMI induced magnon-phonon coupling breaks the combined symmetry of time reversal plus 180° rotation about an in-plane axis [28, 174]. With magnetic fields, this symmetry breaking allows the existence of thermal Hall effects [128], which are absent in magnon-only or phonon-only scenarios. Moreover, in contrast to the ferromagnetic case, $H_{mp}+H_m$ also breaks inversion symmetry [30] and gives rise to chiral phonons at high symmetry points [215, 216] as will be shown below.

4.2 Band Topology

As magnons and phonons are both bosons, one can treat them equivalently as magnon-polaron excitations and re-write Eq. (4.1) to a generalized BdG form as

$$H_{\mathbf{k}} = \begin{bmatrix} \frac{1}{2}H_m(\mathbf{k}) & H_{mp}(\mathbf{k}) & 0 \\ H_{mp}^{\dagger}(\mathbf{k}) & \frac{1}{2}D(\mathbf{k}) & 0 \\ 0 & 0 & \frac{\mathcal{J}_4}{2M} \end{bmatrix}, \tag{4.27}$$

with representation $\mathbf{X_k} = \left(a_{\mathbf{k}}, b_{\mathbf{k}}, a_{-\mathbf{k}}^{\dagger}, b_{-\mathbf{k}}^{\dagger}, \mathbf{u_k}, \mathbf{p}_{-\mathbf{k}}\right)^T$, where $a_{\mathbf{k}}$ ($b_{\mathbf{k}}$) is A (B) sublattice magnon annihilation operator under Holstein-Primakoff representation [71] S_A^+ (S_B^+) $= \sqrt{2S}a$ ($b^{\dagger}$), $\mathbf{u_k}$ ($\mathbf{p}_{-\mathbf{k}}$) is a four-vector for two-dimensional displacements (momenta) of A and B sublattices, H_m ($\mathbf{k}$) ($H_{mp}(\mathbf{k})$) corresponds to Eq. (4.17)–Eq. (4.19) [Eq. (4.24)] and $D(\mathbf{k})$ is the dynamical matrix corresponding to Eq. (4.8)–Eq. (4.10). Under this representation, the bosonic commutator is written as

$$\left[\mathbf{X_k},\ \mathbf{X_k^{\dagger}}\right] = g = \begin{bmatrix} \mathcal{J}_2 & & & \\ & -\mathcal{J}_2 & & \\ & & & i\mathcal{J}_4 \\ & & -i\mathcal{J}_4 & \end{bmatrix}, \tag{4.28}$$

and the eigenstates satisfy [38, 168],

$$gH_{\mathbf{k}} \left|\psi_{n\mathbf{k}}\right\rangle = \sigma_{nn} E_{n\mathbf{k}} \left|\psi_{n\mathbf{k}}\right\rangle,\ \left\langle\psi_{n\mathbf{k}}\right| g \left|\psi_{n'\mathbf{k}}\right\rangle = \sigma_{nn'} \tag{4.29}$$

where $\sigma = \sigma_z \bigotimes \mathcal{I}_{6\times 6}$ stands for particle-hole space. With particle-hole symmetry, $E_{n\mathbf{k}} = E_{n+6,-\mathbf{k}}$ and thus we only plot the first six eigenvalues in Fig. 4.3 and others are redundant.

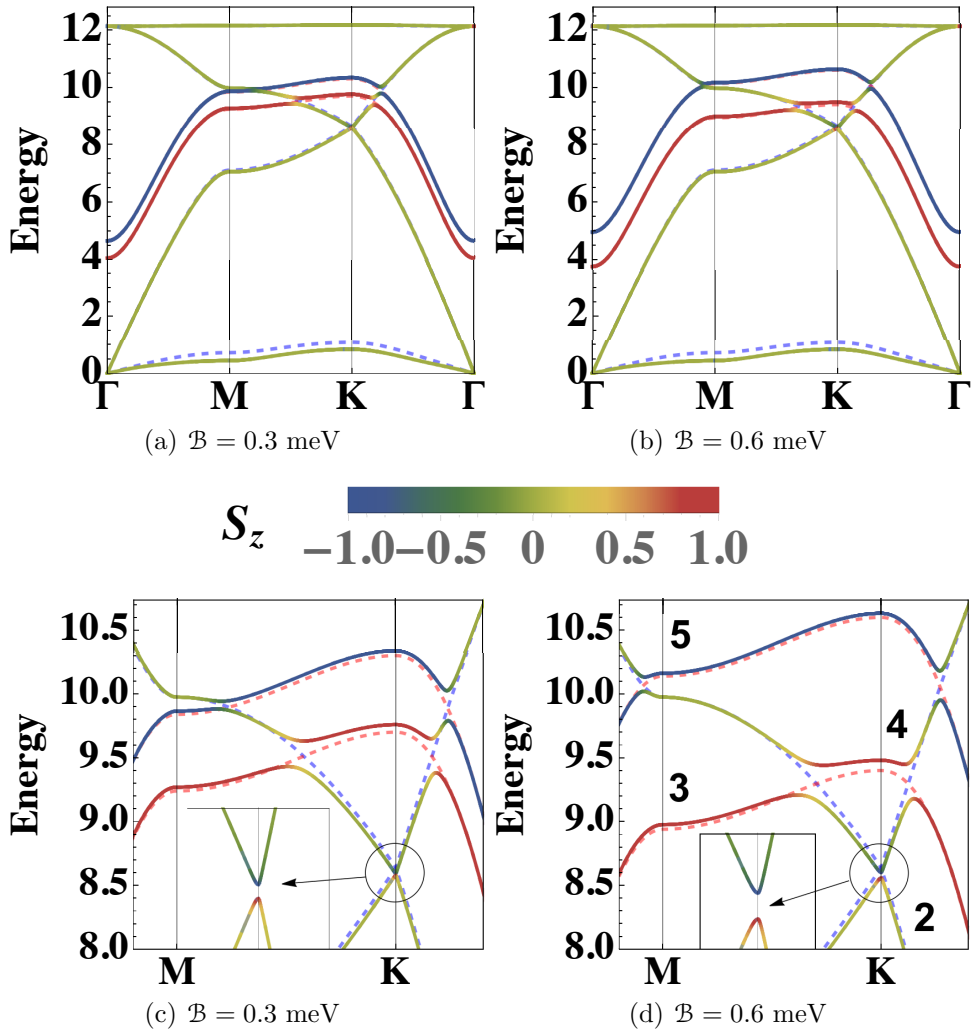

(a) $\mathcal{B} = 0.3$ meV (b) $\mathcal{B} = 0.6$ meV

(c) $\mathcal{B} = 0.3$ meV (d) $\mathcal{B} = 0.6$ meV

Figure 4.3: Topological magnon-polaron bands. Energy is in the unit of meV. We set parameters as $S = 3/2$, $J_1 = 2.0$ meV, $J_2 = 0.0$ meV, $K_z = 1.0$ meV, $m_B/m_A = 1$, $\hbar\sqrt{k_1/M} = 7.0$ meV, $\hbar\sqrt{k_2/M} = 0.5$ meV, $D = 0.2$ meV. The solid lines are bands with DMI and the blue (red) dashed lines are phonon (magnon) dispersions without DMI. (a)(b) Full band dispersions along high symmetry path. (c)(d) Bands around anti-crossing points. Band numbering is shown in (d). The insets show the gap opens at valleys and allows phonons with different chiralities (red or blue). More details for chiral phonons are shown in Fig. 4.6(a)-(d).

Here $S^z = \langle\psi_{n\mathbf{k}}| \left(-a^\dagger_{\mathbf{k}} a_{\mathbf{k}} + b^\dagger_{\mathbf{k}} b_{\mathbf{k}} + \mathbf{u}^A_{\mathbf{k}} \times \mathbf{p}^A_{-\mathbf{k}} + \mathbf{u}^B_{\mathbf{k}} \times \mathbf{p}^B_{-\mathbf{k}}\right) |\psi_{n\mathbf{k}}\rangle$ mediates both magnon spins and phonon polarizations [215].

In Fig. 4.3, there are gapped rings around $\mathbf{\Gamma}$ or $\mathbf{K}$ ($\mathbf{K}'$) formed by anti-crossing points among magnon and phonon bands due to the DMI coupling, which gives rise to nontrivial topological properties in this magnon-polaron system. In such a generalized BdG system, the Berry curvature is given by the Bloch wavefunction $|u_{n\mathbf{k}}\rangle = e^{-i\mathbf{k}\cdot\mathbf{r}} |\psi_{n\mathbf{k}}\rangle$ as [125]

$$\mathbf{\Omega}_{n\mathbf{k}} = i \langle \nabla_{\mathbf{k}} u_{n\mathbf{k}}| \, g \times |\nabla_{\mathbf{k}} u_{n\mathbf{k}}\rangle \,, \tag{4.30}$$

and the Chern numbers can be obtained by integrating Berry curvature $\Omega^z_{n\mathbf{k}}$ along the Brillouin zone as [152]

$$C_n = \frac{1}{2\pi} \int_{BZ} d^2\mathbf{k} \; \Omega^z_{n\mathbf{k}}. \tag{4.31}$$

With Eq. (4.30) and (4.31), we calculate[2] the band Chern numbers[3] by the Fukui method [56] and find that the magnetic field can change the Chern numbers by integers. In Fig. 4.3(a), the Chern numbers for the middle three anti-crossed bands from low to high[4] are $(-2, +4, -2)$, while they change to $(-2, +1, +1)$ in Fig. 4.3(b) by a phase transition when $\mathcal{B} > \mathcal{B}_c (\approx 0.41$ meV with the parameters in Fig. 4.3, see Fig. 4.4). Since in this parameter region the coupling barely affects acoustic modes and the top optical mode,

[2]More details on the numerical method can be found in Appendix. B

[3]As the top (also bottom) two bands are degenerate at Γ point, we add up the Berry curvature of the two bands to obtain a well-defined Chern number. We also adds up the Berry curvature in Fig. 4.5.

[4]That is band–3, band–4 and band–5 numbered in Fig. 4.3(d)

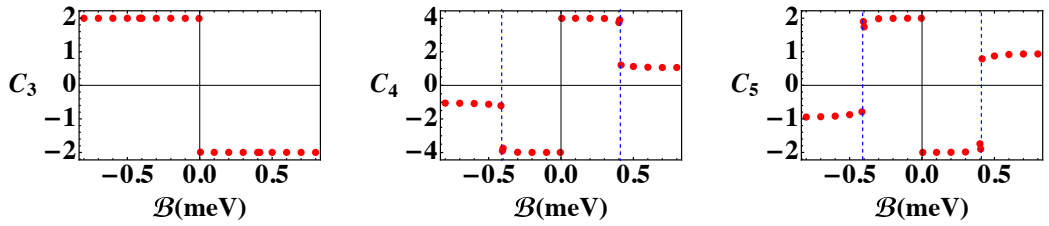

Figure 4.4: Chern numbers with varying the magnetic field. C_n is the Chern number for band–n (n=3, 4, 5). Blue dashed lines show the phase transitions occur at $\mathcal{B} \approx \pm 0.41$ meV with the same parameters used in Fig. 4.3

the band topology can be effectively mapped into an SU(3) algebra [14, 219]. Here, instead of an analytic calculation (which is generally not accessible), we achieve an understanding of the band topology more intuitively by looking at Berry curvatures.

As shown in Fig. 4.5, non-trivial Berry curvatures are induced around the anti-crossing regions, and thus the change of Chern numbers can be intuitively understood as a pair of gapped rings around $\mathbf{K}$ and $\mathbf{K}'$ combining into or splitted by one anti-crossing ring around $\mathbf{\Gamma}$. Notice that there are opposite Berry curvatures at $\mathbf{K}$ and $\mathbf{K}'$ in band–3 from the gap by spin-induced inversion symmetry breaking, but it does not contribute to the Chern number due to a cancellation between these two valleys [216]. However, as shown in Fig. 4.6(a)-(d), large phonon angular momentum $S_P^z = \left\langle \mathbf{u}_{\mathbf{k}}^A \times \mathbf{p}_{-\mathbf{k}}^A + \mathbf{u}_{\mathbf{k}}^B \times \mathbf{p}_{-\mathbf{k}}^B \right\rangle$ occurs at $\mathbf{K}$ for band–2 and band–3 giving rise to chiral phonons. The polarization of these phonons can be flipped by reversing the magnetic field and they can contribute to a valley Hall effect along with the opposite Berry curvature.

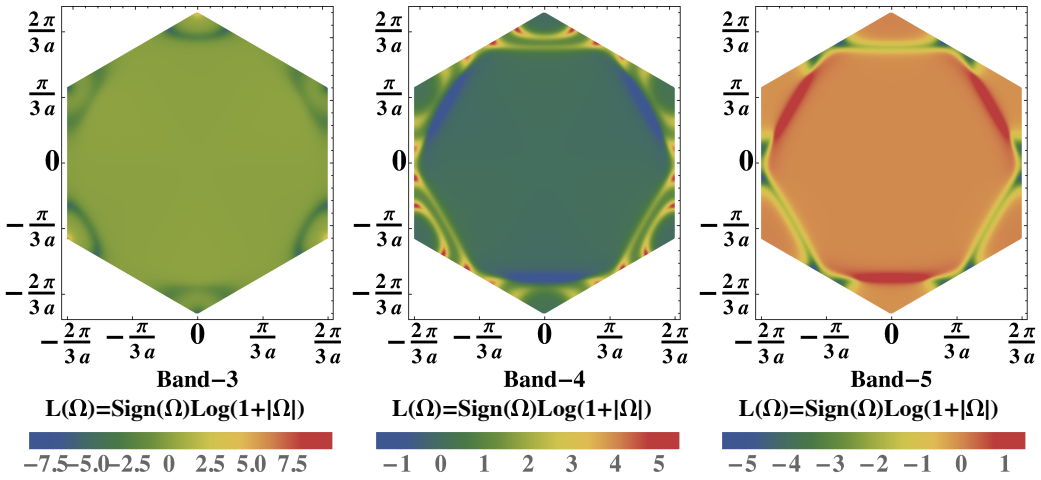

(a) $\mathcal{B} = 0.3$ meV

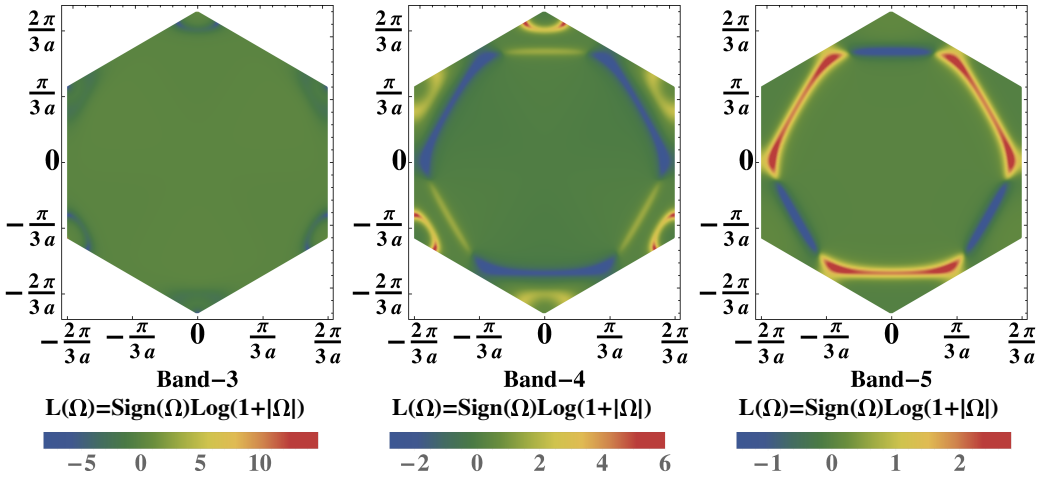

(b) $\mathcal{B} = 0.6$ meV

Figure 4.5: Berry curvatures of the middle three anti-crossed bands in Fig. 4.3. Band numbers are ordered from bottom to top. When the magnetic field increases, there is one gapped ring around $\mathbf{\Gamma}$ between band–3 and band–4 splits into two rings around $\mathbf{K}$ and $\mathbf{K}'$ leading to a topological phase transition.

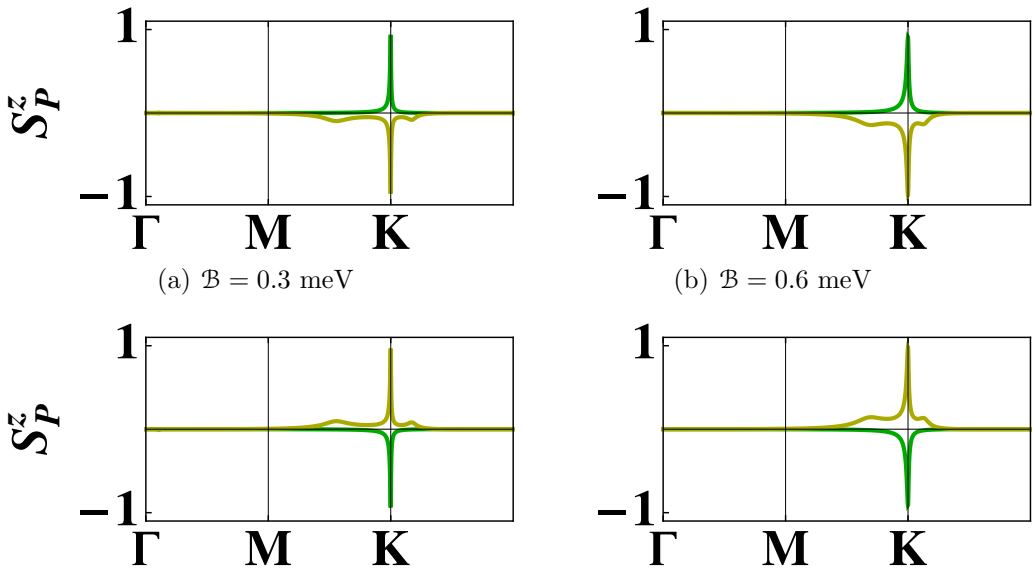

(a) $\mathcal{B} = 0.3$ meV (b) $\mathcal{B} = 0.6$ meV

(c) $\mathcal{B} = -0.3$ meV (d) $\mathcal{B} = -0.6$ meV

Figure 4.6: The contribution of phonon polarization to S_z. The green (yellow) line is for band–2 (3). Changing the direction of the magnetic field can flip the polarization of these phonons.

Similar to the physics of gapped 2D Dirac systems[5] [19], the physics of anti-crossing magnon-phonon pair can be effectively described by

$$H_{\text{eff}} = \frac{E^{\pm}_{m\mathbf{k}} + E^{\pm}_{p\mathbf{k}}}{2}\mathcal{I}_2 + \mathbf{d}^{\pm\pm}_{\mathbf{k}} \cdot \sigma + V_{\mathbf{k}}, \tag{4.32}$$

where $E^{+(-)}_{m\mathbf{k}}$ is the upper (lower) magnon energy without the DMI, $E^{+(-)}_{p\mathbf{k}}$ is the lower optical (upper acoustic) phonon energy without the DMI, $\boldsymbol{\sigma} = (\sigma_x, \sigma_y, \sigma_z)$ is the Pauli matrices, $\mathbf{d}^{\pm\pm}_{\mathbf{k}}$ opens a gap between $E^{\pm}_{m\mathbf{k}}$ and $E^{\pm}_{p\mathbf{k}}$ arising from the DMI and can be regarded as an analog of the gaping term in

[5]Though here we have innumerable band anti-crossing points which form a gapped ring.

Kane-Mele model [85, 98], and $V_{\mathbf{k}}$ includes terms that do not conserve particle numbers and perturbations that do not participate in opening the gap between the two bands [58, 219]. A Skyrmion (anti-Skyrmion) topological charge Q ($-Q$) can then be defined with $\mathbf{d}_{\mathbf{k}}^{\pm\pm}$ as $Q = \frac{1}{4\pi}\int d^2\mathbf{k}\ \hat{\mathbf{d}}_{\mathbf{k}} \cdot \left(\partial_{k_x}\hat{\mathbf{d}}_{\mathbf{k}} \times \partial_{k_y}\hat{\mathbf{d}}_{\mathbf{k}}\right)$ for the upper (lower) band. In general, the analytical expression for $\mathbf{d}_{\mathbf{k}}^{\pm\pm}$ is not available, but since $\mathbf{d}_z^{\pm\pm} = (E_{m\mathbf{k}}^{\pm} - E_{p\mathbf{k}}^{\pm})/2$, the Skyrmion numbers will change with the moving of anti-crossing rings [58]. As the band Chern number reflects the winding number of $\hat{\mathbf{d}}_{\mathbf{k}}$ wrapping the unit sphere in the Brillouin zone, a skyrmion arising from $\mathbf{d}$ with charge Q determines the lower (upper) band with a Chern number Q ($-Q$) [18]. In addition to changing the field strength, reversing the external field will also change the Chern numbers by flipping the sign, thus we find the topology of our system is highly tunable.

4.3 Thermal and Valley Hall Effects

In order to connect our results with possible experimental observations, we evaluate the thermal Hall effect arising from the non-trivial Berry curvatures of magnon-polaron bands. With a longitudinal temperature gradient $\nabla_y T$, an anomalous transverse motion of magnon-polaron excitations can be induced by the fictitious field $\Omega_{n\mathbf{k}}^z$ associated with a transverse thermal conductivity κ_{xy} as [125]

$$\kappa_{xy} = -\frac{k_B^2 T}{\hbar V}\sum_{n,\mathbf{k}}\left[c_2(g(E_{n\mathbf{k}})) - \frac{\pi^2}{3}\right]\Omega_{n\mathbf{k}}^z, \tag{4.33}$$

where $c_2(x) = (1+x)\ln^2(1+1/x) - \ln^2 x - 2\mathrm{Li}_2(-x)$, $\mathrm{Li}_2(x)$ is the polylogarithm function, and $g(x) = (\exp(x/k_BT) - 1)^{-1}$ is the Bose-Einstein distribution. In Fig. 4.7, we evaluate κ_{xy} with parameters [197, 79, 63] for $MnPS_3$ as $m_A = m_B = M = 55$ u, $S = 5/2$, $J_1 = 1.54$ meV, $J_2 = 0.14$ meV, $g = -2.0$ and set $K_z = 0.1$ meV, $D = 0.5$ meV, $\hbar\sqrt{k_1/M} = 11$ meV and $\hbar\sqrt{k_2/M} = 2.2$ meV. At the low field, the two magnon bands couple with the lower optical phonon giving a Chern number distribution $(0,\ +2,\ -4,\ +2)$ from bottom to top, while they couple with the lower optical and upper acoustic phonon respectively at high field giving a Chern distribution $(-2,\ +2,\ -2,\ +2)$. These results are also consistent with our analysis on band topology by looking at the moving of gapped rings. The change of κ_{xy} with magnetic field results from the topological transition with different Chern numbers, while the sign change with temperature reflects the competition among bands of different Chern numbers come to dominate the transverse thermal transport.

In addition, as the spatial inversion symmetry is broken by the spin degree of freedom, the gap opens at $\mathbf{K}$ and $\mathbf{K}'$ valley, and thus gives rise to chiral phonons with different polarizations at these high symmetry points [see Fig. 4.3(c)(d) and 4.7(b)(c)]. This has not been discussed in previous studies in coupled systems without optical phonons. By introducing a longitudinal strain gradient across the system, we expect an opposite motion of chiral phonon at different valleys as $v \propto -\mathbf{E}_{\text{strain}} \times \mathbf{\Omega}$ in the transverse direction and create a temperature difference between two edges [216]. As these two Hall effects originate from non-trivial topology of the system, according to bulk-

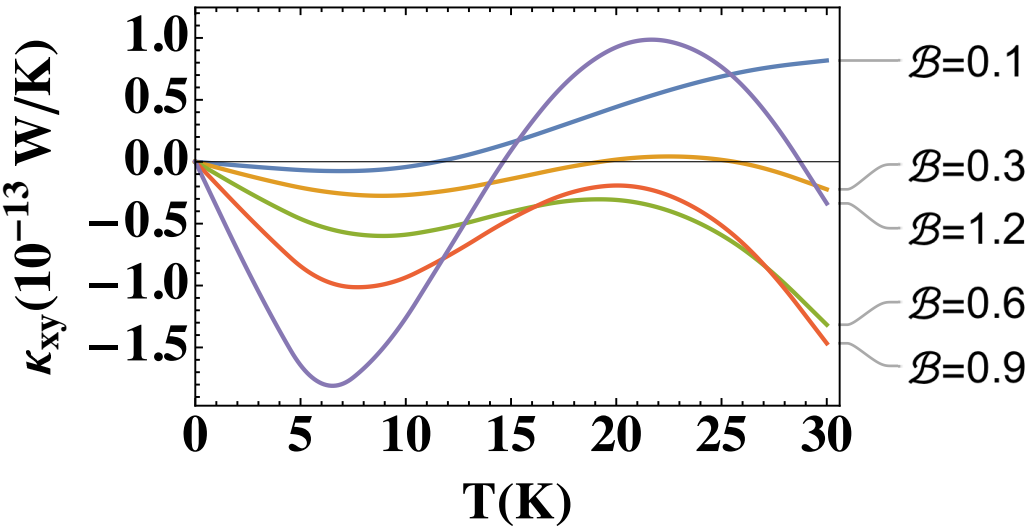

(a) Thermal Hall response. $\mathcal{B}$ is in unit of meV.

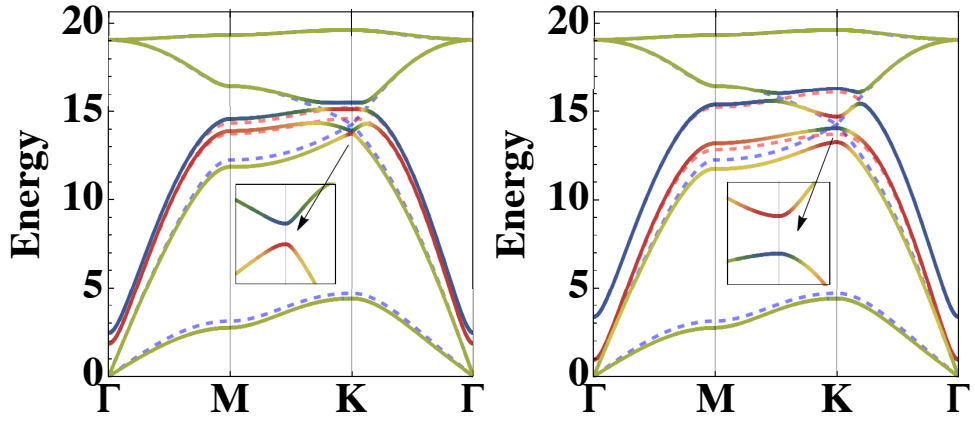

(b) $\mathcal{B}$ = 0.3 meV with Chern number (0, 0, −2, +4, −2, 0).

(c) $\mathcal{B}$ = 1.2 meV with Chern number (0, +2, −2, +2, −2, 0).

Figure 4.7: Thermal Hall response using parameters from $MnPS_3$. A topological phase transition occurs when the magnetic field increases. See main text for details.

edge correspondence, we expect to observe a thermal Hall signal by the edge modes that is weakly affected by the bulk disorders.

4.4 Discussions

In this chapter, we study the topology of magnon-polaron bands in a 2D honeycomb Néel order antiferromagnet with an in-plane DMI induced magnon-phonon coupling. Without DMI, the magnon or phonon bands are trivial, while non-trivial Berry curvature occurs around the anti-crossing rings opened by the magnon-phonon coupling. In contrast to previous studies, in our case, antiferromagnetic magnons can couple with both optical phonons and acoustic phonons giving rise to an integer band Chern numbers with an external magnetic field. Moreover, by changing the field magnitude and direction, it is possible to tune these Chern numbers along with changing the anti-crossing rings. We also investigate thermal Hall effects induced from finite Berry curvatures and propose valley Hall effects with chiral phonons arising from the inversion symmetry breaking by magnons. Even though we study the model on a honeycomb lattice, the coupling can be expressed with a displacement field $\mathbf{u} \approx \mathbf{u}_{ij}/a$ and a stagger spin field $\mathbf{n} \approx (\mathbf{S}_A - \mathbf{S}_B)/2S$ as $\frac{DS^2}{a^3}\,(\nabla \times \mathbf{u}) \cdot (\nabla \times \mathbf{n})$ as in Eq. (4.26), which does not depend on lattice details. This 2D model can also be generalized to a 3D system with mirror symmetry breaking in the bulk [97, 49] and it can couple the magnons with out-of-plane phonon modes as well which could further enrich the physics of topology. In principle, our method can be used in any bosonic systems such as plasmonics [6, 41] and photonics

[147], and may find similar and interesting applications there.

Chapter 5

Summary and Outlook

In this final chapter of the dissertation, we first make a summary of the preceding chapters, remarking the applications to experiments and the progress we made in comparison with prior work, then present an outlook of our work for future study.

In Chapter 2, we studied magnon Nernst effects in a triangular-kagome-triangular pyrochlore iridate thin film. The transverse thermal response of spin currents is due to the topological nature of the magnon bands, originated from a Dzyaloshinskii–Moriya interaction (DMI) and accompanied by a non-collinear all-in/all-out (AIAO) spin ordering. With a spin lattice symmetry consideration, we calculated the temperature dependence of the magnon Nernst response by varying the spin-orbit coupling parameters of the DMI, and found the transport contribution from topologically protected chiral edge modes, complementing prior work on thermal magnons in thin-film pyrochlore iridates and non-collinear systems.

In Chapter 3, instead of the DMI between localized spins, we investigated the interfacial DMI between the spin of itinerant electrons in a non-magnetic metal and the local moments in a magnetic insulator, and its effects

on the thermally-driven spin current transfer at the interface, i.e., the longitudinal spin Seebeck effects. By applying our theory to the interface between an insulating AIAO spin-ordered pyrochlore iridate and a non-magnetic metal, we numerically calculated the dependence of the interfacial spin current on the temperature gradient, the interfacial couplings, and the crystalline orientation along the interface. Our results showed that the magnetic structure and the DMI at the interface, which has not been considered in previous studies, can lead to a significant effect on interfacial spin current transfer.

Having seen the importance of Dzyaloshinskii–Moriya interactions, in Chapter 4, we theoretically studied magnon-phonon coupling by an in-plane DMI from mirror symmetry breaking in a two-dimensional honeycomb antiferromagnet. We found non-trivial Berry curvature due to the gap between magnon and both optical and acoustic phonon bands, and topological magnon-phonon hybridized excitations with highly tunable Chern numbers. The inversion and effective time-reversal symmetry breaking can lead to thermal Hall effects and valley Hall effects, which are absent without the DMI. To our best knowledge, this is the first study on the topological properties arising from the coupling between antiferromagnetic magnons and optical phonons. Our work complements earlier studies that optical phonons are absent or ignored in the magnon-phonon coupling, and it may be useful to design tunable transport devices in the field of spintronics and draw a connection to chiral phonons with spin caloritronics.

While all of our work is motivated by studying the thermal transport

of magnons, we found the Dzyaloshinskii–Moriya interaction (DMI) can have significant effects on magnonics. More fundamentally, it is the magnetic point group symmetry [128, 7] of the ground state and/or the symmetry breaking of the excited state that plays an important role in the physics of magnons, as the DMI can lead to the non-collinearity of spin orderings and affect the symmetry of quasiparticle excitations. However, the DMI, which originated from the asymmetry nature of the exchange couplings, also crucially depends on the symmetry of the materials. Thus, one may ask how the spin current and thermal transport of magnons reversely affect the direction and strength of the DMI and how it may control novel magnetic structures such as skyrmions [221, 156, 211] and hedgehogs [205, 55, 180], and interesting phase of matters such as topological magnons and Weyl magnons. There is also an increasing interest in other non-equilibrium systems with magnons, such as spin-lattice interaction driven by nonlinear phononics [137] and floquet engineering of magnon bands [141, 146].

Appendices

Appendix A

Numerical Method of Bosonic Berry Curvature

In this appendix, we introduce the numerical method for calculating bosonic Berry curvature and bosonic band Chern number.

We begin from a general bosonic BdG Hamiltonian for N particles

$$H = \frac{1}{2}\sum_{\mathbf{k}} \mathbf{X}_{\mathbf{k}}^{\dagger}\mathbf{H}_{\mathbf{k}}\mathbf{X}_{\mathbf{k}} \tag{A.1}$$

with a $2N$ dimensional basis $\mathbf{X}_{\mathbf{k}}$ satisfying a commutator relation

$$[\mathbf{X}_{\mathbf{k}}, \mathbf{X}_{\mathbf{k}}^{\dagger}] = g, \tag{A.2}$$

it can be transformed into a bosonic representation $\mathbf{Y} = Q^{-1}\mathbf{X}$, which satisfies

$$H = \frac{1}{2}\sum_{\mathbf{k}} \mathbf{Y}_{\mathbf{k}}^{\dagger}\mathbf{E}_{\mathbf{k}}\mathbf{Y}_{\mathbf{k}},\ [\mathbf{Y}_{\mathbf{k}}, \mathbf{Y}_{\mathbf{k}}^{\dagger}] = \sigma_3,\ \mathbf{Y}_{\mathbf{k}} = \sigma_1\mathbf{Y}_{-\mathbf{k}}^{*}\sigma_1, \tag{A.3}$$

where $\sigma_3 = \sigma_z \bigotimes \mathcal{I}_{N\times N},\ \sigma_1 = \sigma_x \bigotimes \mathcal{I}_{N\times N}$ and $\mathbf{E}$ is a diagonal matrix. By comparing Eq. (A.1)(A.2) with Eq. (A.3), it can be seen that

$$g = Q[\mathbf{Y}, \mathbf{Y}^{\dagger}]Q^{\dagger} = Q\sigma_3 Q^{\dagger} \Rightarrow Q^{\dagger} = \sigma_3 Q^{-1} g, \tag{A.4}$$

$$Q^{\dagger}\mathbf{H}Q = \mathbf{E} \Rightarrow Q^{-1}g\mathbf{H}Q = \sigma_3\mathbf{E}, \tag{A.5}$$

where the n-th column of Q corresponds to the linear representation under basis $\mathbf{X}$ for eigenvector $|u_{n\mathbf{k}}\rangle$ in the main text. Then, with Eq. (A.3) and (A.5),

$$\begin{aligned} i\hbar\frac{d}{dt}\mathbf{X}_{\mathbf{k}} = i\hbar Q_{\mathbf{k}}\frac{d}{dt}\mathbf{Y}_{\mathbf{k}} = Q_{\mathbf{k}}[\mathbf{Y}_{\mathbf{k}},\ H] = Q_{\mathbf{k}}[\mathbf{Y}_{\mathbf{k}},\ \frac{1}{2}\sum_{\mathbf{k}'}\mathbf{Y}^{\dagger}_{\mathbf{k}'}\mathbf{E}_{\mathbf{k}'}\mathbf{Y}_{\mathbf{k}'}] \\ = Q_{\mathbf{k}}\sigma_3\mathbf{E}_{\mathbf{k}}\mathbf{Y}_{\mathbf{k}} = Q_{\mathbf{k}}\sigma_3\mathbf{E}_{\mathbf{k}}Q^{-1}_{\mathbf{k}}\mathbf{X}_{\mathbf{k}} = g\mathbf{H}_{\mathbf{k}}\mathbf{X}_{\mathbf{k}}. \end{aligned} \tag{A.6}$$

Therefore, a bosonic vector potential $\mathbf{A}_n$ and Berry curvature $\mathbf{\Omega}_{n\mathbf{k}}$ for $\mathbf{X}_{\mathbf{k}}$ can be defined as[1][30, 220]

$$\mathbf{A}_n = i\left\langle u_{n\mathbf{k}}\right| g^{-1}\partial_{\mathbf{k}}\left|u_{n\mathbf{k}}\right\rangle,\ \mathbf{\Omega}_{n\mathbf{k}} = i\left\langle \nabla_{\mathbf{k}}u_{n\mathbf{k}}\right| g^{-1}\times\left|\nabla_{\mathbf{k}}u_{n\mathbf{k}}\right\rangle. \tag{A.7}$$

With the spirit of a momentum space lattice discretization method by Fukui *et al.* [56] and gauge-independent Berry curvature computation [18], the Chern number and Berry curvature can be numerically calculated from Eq. (A.7) once $Q_{\mathbf{k}}$ has been found.

If there is no dispersionless Goldstone mode in the system, $\det g\mathbf{H} \neq 0$ and the eigenvectors P of $g\mathbf{H}$ can be found easily in any numerical methods, and if there is no degeneracy (or the degeneracy can be avoided in numerics), the eigenvectors can be rearranged so that

$$Q = PT, \tag{A.8}$$

where $T = \mathrm{Diag}(t_1, t_2, \ldots, t_{2N})$. Taking Eq. (A.8) into Eq. (A.5), one can find

$$P^{-1}g(P^{\dagger})^{-1} = T\sigma_3T^{\dagger} = \sigma_3\mathrm{Diag}(|t_1|^2, |t_2|^2, \ldots, |t_{2N}|^2) \tag{A.9}$$

[1]In the chapter 2 and chapter 4 of the main text, we both have $g = g^{-1}$.

is a diagonal matrix and $|t_i|$ can be solved from Eq. (A.9). Therefore, the paraunitary matrix Q can be constructed from eigenvectors P as

$$Q = P(P^\dagger g^{-1} P \sigma_3)^{-\frac{1}{2}} U, \tag{A.10}$$

where U is a $U(1)$ phase factor that can be chosen as the identity.

Appendix B

Derivation on Interfacial Magnon-Electron Couplings

In this appendix, we derive Eq. (3.6) from Eq. (3.5). We explicitly write the contribution to interfacial couplings from the Heisenberg exchange coupling and the Dzyaloshinskii–Moriya interaction (DMI) as

$$V = \sum_{<ij>} J_{ij}\rho(\mathbf{r},z)\cdot\mathbf{S}_{\beta,l=0}(\mathbf{r}_j)\delta_{z,0}\delta_{\mathbf{r},\mathbf{r}_i}, \tag{B.1}$$

$$U = \mathbf{D}_{ij}\cdot\left(\rho(\mathbf{r},z)\times\mathbf{S}_{\beta,l=0}(\mathbf{r}_j)\right)\delta_{z,0}\delta_{\mathbf{r},\mathbf{r}_i}. \tag{B.2}$$

In order to write the Hamiltonian into a second quantized form, we need to express Eq. (B.1) and (B.2) with local coordinates.

Noticing that

$$\begin{aligned}\rho\cdot\mathbf{S} = \rho\cdot\left(\mathcal{R}_\beta^{-1}\mathbf{S}'_\beta\right) = (\mathcal{R}_\beta\rho)\cdot\mathbf{S}'_\beta &= \frac{\hbar}{2}\sum_{\sigma\sigma'}\psi^\dagger_\sigma(\mathbf{r},z)\psi_{\sigma'}(\mathbf{r},z)\left[(\mathcal{R}_\beta\sigma)\cdot\mathbf{S}'_\beta\right]_{\sigma\sigma'} \\ &= \frac{\hbar}{2}\sum_{\sigma\sigma'}\psi^\dagger_\sigma(\mathbf{r},z)\psi_{\sigma'}(\mathbf{r},z)\left[\frac{\sigma'^{+}S'^{-}+\sigma'^{-}S'^{+}}{2}+\sigma'^{z}S'^{z}\right]_{\sigma\sigma'}\end{aligned} \tag{B.3}$$

where $\sigma' = \mathcal{R}_\beta\sigma$, i.e.

$$\frac{\sigma'^{+}}{2} = \left(\frac{\sigma'^{-}}{2}\right)^\dagger = \begin{pmatrix} -\frac{1}{2}\sin\theta_\beta & \cos^2\frac{\theta_\beta}{2}e^{-i\phi_\beta} \\ -\sin^2\frac{\theta_\beta}{2}e^{i\phi_\beta} & \frac{1}{2}\sin\theta_\beta \end{pmatrix}$$

By plugging Eqs. (3.3) and (3.1) into Eq. (B.1) with Bogoliubov Transformation Eq. (3.4), we have

$$V = \frac{\hbar^2}{2A}\sqrt{\frac{2S}{N}}\sum_{<ij>} J_{\alpha\beta}\sum_{\mathbf{qkk'}} e^{-i(\mathbf{k}-\mathbf{k'})\cdot\mathbf{r}} e^{-i\mathbf{q}\cdot\mathbf{r_j}}\delta_{z,0}\delta_{\mathbf{r},\mathbf{r}_i}$$
$$\times\sum_{h}\sum_{\nu l}\sum_{\sigma\sigma'}\left(V^{l\ (h)}_{\beta\nu}(\mathbf{q})b^{l\,\dagger}_{\nu}(\mathbf{q})\ c^{\dagger}_{\mathbf{k}\sigma}L^{(h)}_{\sigma\sigma'}c_{\mathbf{k'}\sigma'} + \text{h.c.}\right) \tag{B.4}$$

where $L^{(h)} = \left(\frac{\sigma^+}{2}, \frac{\sigma^-}{2}, \sigma^z\right)$ and

$$\begin{cases} V^{l\ (1)}_{\beta\nu}(\mathbf{q}) = \left(M^{0l\,*}_{\beta\nu}(\mathbf{q}))\cos^2\frac{\theta_\beta}{2} - N^{0l}_{\beta\nu}(-\mathbf{q})\sin^2\frac{\theta_\beta}{2}\right)e^{-i\phi_\beta} \\ V^{l\ (2)}_{\beta\nu}(\mathbf{q}) = \left(N^{0l}_{\beta\nu}(-\mathbf{q}))\cos^2\frac{\theta_\beta}{2} - M^{0l\,*}_{\beta\nu}(\mathbf{q})\sin^2\frac{\theta_\beta}{2}\right)e^{i\phi_\beta} \\ V^{l\ (3)}_{\beta\nu}(\mathbf{q}) = -\frac{\sin\theta_\beta}{2}\left(M^{0l\,*}_{\beta\nu}(\mathbf{q}) + N^{0l}_{\beta\nu}(-\mathbf{q})\right) \end{cases}$$

One might notice that, in Eq. (B.4),

- We discard the classical contribution to the interfacial exchange interaction, i.e., terms that are zeroth order in magnon operators, as it leads to a contribution to the spin current which is vanishing in the absence of spin accumulation [17].

- We discard terms of the type $c^{\dagger}_{\mathbf{k}\sigma}c_{\mathbf{k'}\sigma'}a^{\dagger}_{\mathbf{q}}a_{\mathbf{q'}}\delta_{\sigma\sigma'}$ as they appear to modify spin flows at higher orders (in bias and thermal fluctuations).

- Terms with different magnon-band indices will not mix as $\langle b^{l\,\dagger}_{\nu}b^{l'}_{\nu'}\rangle = \delta_{\nu\nu'}\delta_{ll'}$.

Similarly, for DMI term, noticing that

$$\begin{aligned}\mathbf{D}\cdot(\rho\times\mathbf{S}_\beta) &= \mathbf{D}\cdot\left(\rho\times(\mathcal{R}_\beta^{-1}\mathbf{S}'_\beta)\right)=\mathbf{D}\cdot\mathcal{R}_\beta^{-1}\left((\mathcal{R}_\beta\rho)\times\mathbf{S}'_\beta\right)\\ &=(\mathcal{R}_\beta\mathbf{D})\cdot\left((\mathcal{R}_\beta\rho)\times\mathbf{S}'_\beta\right)=((\mathcal{R}_\beta\mathbf{D})\times(\mathcal{R}_\beta\rho))\cdot\mathbf{S}'_\beta\\ &=\mathcal{R}_\beta(\mathbf{D}\times\rho)\cdot\mathbf{S}'_\beta=\frac{\hbar}{2}\sum_{\sigma\sigma'}\psi^\dagger_\sigma(\mathbf{r},z)\psi_{\sigma'}(\mathbf{r},z)\left[\mathbf{\Sigma}'\cdot\mathbf{S}'_\beta\right]_{\sigma\sigma'},\end{aligned}\tag{B.5}$$

where $\mathbf{\Sigma}'=\mathcal{R}_\beta(\mathbf{D}\times\sigma)$.

Eq. (B.5) has the same structure if we replace $\mathbf{\Sigma}'$ to σ' in Eq. (B.3), so we expect a very similar expression of U as Eq. (B.4). With some calculation, one can easily work out that

$$\begin{aligned}U=&\frac{\hbar^2}{2A}\sqrt{\frac{2S}{N}}\sum_{<ij>}D_{\alpha\beta}\sum_{\mathbf{qkk'}}e^{-i(\mathbf{k}-\mathbf{k}')\cdot\mathbf{r}}e^{-i\mathbf{q}\cdot\mathbf{r_j}}\delta_{z,0}\delta_{\mathbf{r},\mathbf{r}_i}\\ &\times\sum_h\sum_{\nu l}\sum_{\sigma\sigma'}\left(U^l_{\alpha\beta\nu}{}^{(h)}(\mathbf{q})b^{l\,\dagger}_\nu(\mathbf{q})\;c^\dagger_{\mathbf{k}\sigma}L^{(h)}_{\sigma\sigma'}c_{\mathbf{k}'\sigma'}+\text{h.c.}\right)\end{aligned}\tag{B.6}$$

where $\mathbf{D}_{\alpha\beta}=D_{\alpha\beta}\mathbf{d}_{\alpha\beta}$ with $|\mathbf{d}_{\alpha\beta}|=1$ and

$$\begin{cases}U^l_{\alpha\beta\nu}{}^{(1)}(\mathbf{q}) &= i\left[d^3_{\alpha\beta}\left(M^{0l\,*}_{\beta\nu}(\mathbf{q}))\cos^2\frac{\theta_\beta}{2}-N^{0l}_{\beta\nu}(-\mathbf{q})\sin^2\frac{\theta_\beta}{2}\right)e^{-i\phi_\beta}\right]\\ &+ i\left[(d^1_{\alpha\beta}-id^2_{\alpha\beta})\frac{\sin\theta_\beta}{2}\left(M^{0l\,*}_{\beta\nu}(\mathbf{q})+N^{0l}_{\beta\nu}(-\mathbf{q})\right)\right]\\ &= i\left[d^3_{\alpha\beta}V^l_{\beta\nu}{}^{(1)}(\mathbf{q})-(d^1_{\alpha\beta}-id^2_{\alpha\beta})V^l_{\beta\nu}{}^{(3)}(\mathbf{q})\right]\\ U^l_{\alpha\beta\nu}{}^{(2)}(\mathbf{q}) &= -i\left[d^3_{\alpha\beta}\left(N^{0l}_{\beta\nu}(-\mathbf{q}))\cos^2\frac{\theta_\beta}{2}-M^{0l\,*}_{\beta\nu}(\mathbf{q})\sin^2\frac{\theta_\beta}{2}\right)e^{i\phi_\beta}\right]\\ &- i\left[(d^1_{\alpha\beta}+id^2_{\alpha\beta})\frac{\sin\theta_\beta}{2}\left(M^{0l\,*}_{\beta\nu}(\mathbf{q})+N^{0l}_{\beta\nu}(-\mathbf{q})\right)\right]\\ &= i\left[(d^1_{\alpha\beta}+id^2_{\alpha\beta})V^l_{\beta\nu}{}^{(3)}(\mathbf{q})-d^3_{\alpha\beta}V^l_{\beta\nu}{}^{(2)}(\mathbf{q})\right]\\ U^l_{\alpha\beta\nu}{}^{(3)}(\mathbf{q}) &= i\left[\frac{d^1_{\alpha\beta}-id^2_{\alpha\beta}}{2}\left(N^{0l}_{\beta\nu}(-\mathbf{q}))\cos^2\frac{\theta_\beta}{2}-M^{0l\,*}_{\beta\nu}(\mathbf{q})\sin^2\frac{\theta_\beta}{2}\right)e^{i\phi_\beta}\right]\\ &- i\left[\frac{d^1_{\alpha\beta}+id^2_{\alpha\beta}}{2}\left(M^{0l\,*}_{\beta\nu}(\mathbf{q}))\cos^2\frac{\theta_\beta}{2}-N^{0l}_{\beta\nu}(-\mathbf{q})\sin^2\frac{\theta_\beta}{2}\right)e^{-i\phi_\beta}\right]\\ &= i\left[\frac{d^1_{\alpha\beta}-id^2_{\alpha\beta}}{2}V^l_{\beta\nu}{}^{(2)}(\mathbf{q})-\frac{d^1_{\alpha\beta}+id^2_{\alpha\beta}}{2}V^l_{\beta\nu}{}^{(1)}(\mathbf{q})\right]\end{cases}$$

Combining Eq. (B.4) and Eq. (B.6), we obtain Eq. (3.5) in Chapter 3.

Appendix C

Derivation on Spin Currents in the LSSE

In this appendix, we derive the spin current expression in Eq. (3.10) by Wick's theorem. Assuming the magnetic order to be static, from definition Eq. (3.9), the interfacial spin current $\mathbf{I} = A\mathbf{i}$ can be written as

$$\mathbf{I} = -\frac{\hbar}{2}\frac{d}{dt}\sum_{\mathbf{k}}\sum_{\sigma\sigma'} c^{\dagger}_{\mathbf{k}\sigma}(z=0)\sigma_{\sigma\sigma'}c_{\mathbf{k}\sigma'}(z=0). \tag{C.1}$$

Let us write the spin and wave-number index by a capital letter $S = (\mathbf{k}, \sigma)$ and introduce

$$H_1 = \sum_{h}\sum_{qSS'} \delta_{\mathbf{k}-\mathbf{k}'+\mathbf{q},\mathbf{G}} e^{-i(\mathbf{k}-\mathbf{k}')\cdot\mathbf{r}_\alpha - i\mathbf{q}\cdot r_\beta}\, {H^l_{\alpha\beta\nu}}^{(h)}(\mathbf{q}, S, S') {b^l_\nu}^{\dagger}(\mathbf{q}) c^{\dagger}_S c_{S'}, \tag{C.2}$$

where ${H^l_{\alpha\beta\nu}}^{(h)}(\mathbf{q}, S, S') = {H^l_{\alpha\beta\nu}}^{(h)}(\mathbf{q}) L^{(h)}_{\sigma\sigma'}$

In this shorthand,

$$\mathcal{H}_I = \frac{\hbar^2\sqrt{2NS}}{2A}\sum_{\langle\alpha\beta\rangle}\sum_{\nu l}\left(H_1 + {H_1}^{\dagger}\right). \tag{C.3}$$

For simplicity, we drop the sum over $\langle\alpha\beta\rangle, \nu$ and l for a while, and recover the sum in the end. Invoking the Heisenberg equation of motion, we can find

$$I_{SS'} \equiv \frac{d}{dt}c^{\dagger}_S(z=0)c_{S'}(z=0) = -\frac{i}{\hbar}[\mathcal{H}, c^{\dagger}_S c_{S'}] = -\frac{i}{\hbar}[\mathcal{H}_I, c^{\dagger}_S c_{S'}] = K_{SS'} + (K_{S'S})^{\dagger} \tag{C.4}$$

with

$$
\begin{aligned}
K_{SS'} &= -i\frac{\hbar\sqrt{2NS}}{2A}\left[H_1, c_S^\dagger c_{S'}\right] \\
&= -i\frac{\hbar\sqrt{2NS}}{2A}\sum_{h\mathbf{q}RR'} e^{-i(\mathbf{k}-\mathbf{k}')\cdot\mathbf{r}_\alpha - i\mathbf{q}\cdot\mathbf{r}_\beta} {H^l_{\alpha\beta\nu}}^{(h)}(\mathbf{q},R,R') {b^l_\nu}^\dagger(\mathbf{q})\left[c_R^\dagger c_{R'}, c_S^\dagger c_{S'}\right]\delta_{\mathbf{k}-\mathbf{k}'+\mathbf{q},\mathbf{G}} \\
&= -i\frac{\hbar\sqrt{2NS}}{2A}\sum_{hqR}\Big[\delta_{\mathbf{K}-\mathbf{k}+\mathbf{q},\mathbf{G}} e^{-i(\mathbf{K}-\mathbf{k})\cdot\mathbf{r}_\alpha - i\mathbf{q}\cdot\mathbf{r}_\beta} {H^l_{\alpha\beta\nu}}^{(h)}(\mathbf{q},R,S) {b^l_\nu}^\dagger(\mathbf{q}) c_R^\dagger c_{S'} \\
&-\delta_{\mathbf{k}'-\mathbf{K}+\mathbf{q},\mathbf{G}} e^{-i(\mathbf{k}'-\mathbf{K})\cdot\mathbf{r}_\alpha - i\mathbf{q}\cdot\mathbf{r}_\beta} {H^l_{\alpha\beta\nu}}^{(h)}(\mathbf{q},S,R) {b^l_\nu}^\dagger(\mathbf{q}) c_S^\dagger c_R\Big],
\end{aligned}
\tag{C.5}
$$

where $R = (\mathbf{K}, \sigma'')$, $\mathbf{G}$ is the reciprocal lattice vector. Next, we use the Kubo formula to find

$$
\begin{aligned}
\langle I_{SS'}\rangle &= -\frac{i}{\hbar}\int_{-\infty}^{+\infty} dt'\ \theta(t-t')\langle[I_{S'S}(t), \mathcal{H}_I(t')]\rangle_0 \\
&= -\frac{i\hbar\sqrt{2NS}}{2A}\int_{-\infty}^{+\infty} dt'\ \theta(t-t')\langle\Big[K_{SS'}(t) + \left(K_{S'S}(t)\right)^\dagger, H_1(t') + H_1(t')^\dagger\Big]\rangle_0.
\end{aligned}
\tag{C.6}
$$

Since both $H_1(t)$ and $K_{SS'}(t)$ are proportional to $b^\dagger$, we can rewrite

$$
\langle I_{SS'}\rangle = -iW_{SS'} + iW^*_{S'S}, \tag{C.7}
$$

where

$$
W_{SS'} = \frac{1}{\hbar}\int_{-\infty}^{+\infty} dt'\ \theta(t-t')\langle\left[K_{SS'}(t),\ \frac{\hbar^2\sqrt{2NS}}{2A}H_1^\dagger(t')\right]\rangle_0. \tag{C.8}
$$

We introduce the spin-resolved current as

$$
\langle I_{\sigma\sigma'}\rangle = \sum_{\mathbf{k}}\langle I_{\mathbf{k}\sigma,\mathbf{k}\sigma'}\rangle = -i\left(Y_{\sigma\sigma'} - Y^*_{\sigma'\sigma}\right) \quad \text{with} \quad Y_{\sigma\sigma'} = \sum_{\mathbf{k}} W_{\mathbf{k}\sigma,\mathbf{k}\sigma'}\,. \tag{C.9}
$$

Thus, the spin current can be written as

$$\begin{aligned}\langle \mathbf{I} \rangle &= -\frac{\hbar}{2}\sum_{\sigma,\sigma'}\sigma_{\sigma\sigma'}\langle I_{\sigma\sigma'}\rangle = i\frac{\hbar}{2}\sum_{\sigma\sigma'}\left(\sigma_{\sigma\sigma'}Y_{\sigma\sigma'} - \sigma_{\sigma\sigma'}Y^*_{\sigma'\sigma}\right) \\ &= i\frac{\hbar}{2}\mathrm{Tr}\left[\sigma^T Y - \sigma Y^*\right] = i\frac{\hbar}{2}\mathrm{Tr}\left[\sigma^T Y - (\sigma^T Y)^*\right] = -\hbar\mathfrak{Im}\left[\mathrm{Tr}(\sigma^T Y)\right] \\ &= -\mathfrak{Im}\left[\mathrm{Tr}(\sigma(\hbar Y^T))\right]. \end{aligned} \tag{C.10}$$

After some algebraic manipulations and invoking the Wick's theorem, we find

$$\hbar Y_{\sigma,\sigma'} = \sum_k \int_{-\infty}^{+\infty} dt'\ \theta(t-t')\langle\left[K_{\mathbf{k}\sigma,\mathbf{k}\sigma'}(t),\ \frac{\hbar^2\sqrt{2NS}}{2A}H_1^\dagger(t')\right]\rangle_0 \tag{C.11}$$

$$= \frac{\hbar^3 NS}{2A^2}\sum_{hh'}\sum_{\substack{\langle\alpha\beta\rangle \\ \langle\alpha'\beta'\rangle}}\sum_{\mathbf{qkk'}}\delta_{\mathbf{k}-\mathbf{k'}+\mathbf{q},\mathbf{G}}H^{l}_{\alpha\beta\nu}{}^{(h)}(\mathbf{q})H^{l}_{\alpha'\beta'\nu}{}^{(h')*}(\mathbf{q})e^{-i(\mathbf{k}-\mathbf{k'})\cdot(\mathbf{r}_\alpha-\mathbf{r}'_\alpha)-i\mathbf{q}\cdot(\mathbf{r}_\beta-\mathbf{r}'_\beta)} \tag{C.12}$$

$$\times\left\{\int_{-\infty}^{+\infty} dt'\ \theta(t-t')D^{l<}_{\nu\mathbf{q}}(t'-t)\left[L^{(h)},\ G^{>}_{\mathbf{k}}(t-t')L^{(h')^T}G^{<}_{\mathbf{k'}}(t-t')\right]_{\sigma'\sigma}\right.$$

$$\left.-\int_{-\infty}^{+\infty} dt'\ \theta(t-t')D^{l>}_{\nu\mathbf{q}}(t'-t)\left[L^{(h)},\ G^{<}_{\mathbf{k}}(t-t')L^{(h')^T}G^{>}_{\mathbf{k'}}(t-t')\right]_{\sigma'\sigma}\right\} \tag{C.13}$$

where

$$G^{>}_{\mathbf{k}}(t-t') = \begin{pmatrix} G^{>}_{k\uparrow\uparrow}(t-t') & G^{>}_{k\uparrow\downarrow}(t-t') \\ G^{>}_{k\downarrow\uparrow}(t-t') & G^{>}_{k\downarrow\downarrow}(t-t')\end{pmatrix}, \tag{C.14}$$

with $G^{>}_{\mathbf{k}\beta\delta}(t-t') = -i\langle c_\beta(t)c^\dagger_\delta(t')\rangle_0$, $G^{<}_{\mathbf{k}\beta\delta}(t-t') = i\langle c_\beta(t')c^\dagger_\delta(t)\rangle_0$, $D^{l<}_{\nu\mathbf{q}}(t-t') = -i\langle b^{l\dagger}_{\nu,\mathbf{q}}(t')b^{l}_{\nu,\mathbf{q}}(t)\rangle_0$ and $D^{l>}_{\mathbf{q}}(t-t') = -i\langle b^{l}_{\nu,\mathbf{q}}(t)b^{l\dagger}_{\nu,\mathbf{q}}(t')\rangle_0$. In our case, $\hat{G}^{<(>)}_{\mathbf{k}}(t'-t) = \hat{I}G^{<(>)}_{\mathbf{k}}(t'-t)$, where $\hat{I}$ is the identity matrix.

Hence, Eq. (C.13) becomes

$$\hbar Y^T = \frac{\hbar^3 NS}{2A^2} \sum_{hh'} \sum_{\substack{\langle\alpha\beta\rangle \\ \langle\alpha'\beta'\rangle}} \sum_{\mathbf{qkk'}} H^l_{\alpha\beta\nu}{}^{(h)}(\mathbf{q}) H^l_{\alpha'\beta'\nu}{}^{(h')*}(\mathbf{q}) \delta_{\mathbf{k}-\mathbf{k'}+\mathbf{q},\mathbf{G}} \left[L^{(h')}, L^{(h)T}\right]$$
$$\times \int dt'\ \theta(t-t') \left[D^{l<}_{\mathbf{q}}(t-t') G^{>}_{\mathbf{k}}(t-t') G^{<}_{\mathbf{k'}}(t'-t)\right.$$
$$\left. - D^{l>}_{\mathbf{q}}(t-t') G^{<}_{\mathbf{k}}(t-t') G^{>}_{\mathbf{k'}}(t'-t)\right] e^{-i(\mathbf{k}-\mathbf{k'})\cdot(\mathbf{r}_\alpha - \mathbf{r}'_\alpha) - i\mathbf{q}\cdot(\mathbf{r}_\beta - \mathbf{r}'_\beta)}. \qquad \text{(C.15)}$$

Let us introduce for now

$$B_{\nu l}(\mathbf{q},\mathbf{k},\mathbf{k'}) = \int_{-\infty}^{+\infty} dt'\ \theta(t-t') \left[D^{l<}_{\mathbf{q}}(t-t') G^{>}_{\mathbf{k}}(t-t') G^{<}_{\mathbf{k'}}(t'-t)\right.$$
$$\left. - D^{l>}_{\mathbf{q}}(t-t') G^{<}_{\mathbf{k}}(t-t') G^{>}_{\mathbf{k'}}(t'-t)\right], \qquad \text{(C.16)}$$

and it's easy to find

h	h'	$\left[L^{(h')}, L^{(h)T}\right]$	$\mathrm{Tr}\left(\sigma\left[L^{(h')}, L^{(h)T}\right]\right)$
1	1	$\frac{\sigma_z}{2}$	$(0,0,1)$
1	2	0	0
1	3	$-\frac{\sigma_+}{2}$	$(-1,-i,0)$
2	1	0	0
2	2	$-\frac{\sigma_z}{2}$	$(0,0,-1)$
2	3	$\frac{\sigma_-}{2}$	$(1,-i,0)$
3	1	$-\frac{\sigma_-}{2}$	$(-1,i,0)$
3	2	$\frac{\sigma_+}{2}$	$(1,i,0)$
3	3	0	0

Finally, we have Eq. (3.10) in the main text as

$$\begin{cases} \langle I^x \rangle = \frac{\hbar^3 NS}{A^2} \sum_{\nu l} \sum_{hh'} \sum_{<\alpha'\beta'>}^{\langle\alpha\beta\rangle} \sum_{\mathbf{qkk'}} \delta_{\mathbf{k}-\mathbf{k'}+\mathbf{q},\mathbf{G}} e^{-i(\mathbf{k}-\mathbf{k'})\cdot(\mathbf{r}_\alpha - \mathbf{r}'_\alpha) - i\mathbf{q}\cdot(\mathbf{r}_\beta - \mathbf{r}'_\beta)} \\ \times \mathfrak{Re}\left[{H^l_{\alpha\beta\nu}}^{(3)}(\mathbf{q}) {H^l_{\alpha'\beta'\nu}}^{(1)*}(\mathbf{q}) - {H^l_{\alpha\beta\nu}}^{(3)}(\mathbf{q}) {H^l_{\alpha'\beta'\nu}}^{(2)*}(\mathbf{q}) \right] \mathfrak{Im}\left[B_{\nu l}(\mathbf{q}, \mathbf{k}, \mathbf{k'}) \right] \\ \\ \langle I^y \rangle = \frac{\hbar^3 NS}{A^2} \sum_{\nu l} \sum_{hh'} \sum_{<\alpha'\beta'>}^{\langle\alpha\beta\rangle} \sum_{\mathbf{qkk'}} \delta_{\mathbf{k}-\mathbf{k'}+\mathbf{q},\mathbf{G}} e^{-i(\mathbf{k}-\mathbf{k'})\cdot(\mathbf{r}_\alpha - \mathbf{r}'_\alpha) - i\mathbf{q}\cdot(\mathbf{r}_\beta - \mathbf{r}'_\beta)} \\ \times \mathfrak{Im}\left[{H^l_{\alpha\beta\nu}}^{(3)}(\mathbf{q}) {H^l_{\alpha'\beta'\nu}}^{(1)*}(\mathbf{q}) + {H^l_{\alpha\beta\nu}}^{(3)}(\mathbf{q}) {H^l_{\alpha'\beta'\nu}}^{(2)*}(\mathbf{q}) \right] \mathfrak{Im}\left[B_{\nu l}(\mathbf{q}, \mathbf{k}, \mathbf{k'}) \right] \\ \\ \langle I^z \rangle = \frac{\hbar^3 NS}{2A^2} \sum_{\nu l} \sum_{hh'} \sum_{<\alpha'\beta'>}^{\langle\alpha\beta\rangle} \sum_{\mathbf{qkk'}} \delta_{\mathbf{k}-\mathbf{k'}+\mathbf{q},\mathbf{G}} e^{-i(\mathbf{k}-\mathbf{k'})\cdot(\mathbf{r}_\alpha - \mathbf{r}'_\alpha) - i\mathbf{q}\cdot(\mathbf{r}_\beta - \mathbf{r}'_\beta)} \\ \times \mathfrak{Re}\left[{H^l_{\alpha\beta\nu}}^{(2)}(\mathbf{q}) {H^l_{\alpha'\beta'\nu}}^{(2)*}(\mathbf{q}) - {H^l_{\alpha\beta\nu}}^{(1)}(\mathbf{q}) {H^l_{\alpha'\beta'\nu}}^{(1)*}(\mathbf{q}) \right] \mathfrak{Im}\left[B_{\nu l}(\mathbf{q}, \mathbf{k}, \mathbf{k'}) \right] \end{cases}$$

To compute $\mathfrak{Im}\left[B_{\nu l}(\mathbf{q}, \mathbf{k}, \mathbf{k}')\right]$, or , performing a Fourier transform, one can rewrite Eq. (C.16) in terms of the spectral function for the νth magnon band at the lth layer, $A^l_\nu(\mathbf{q}, \omega)$, and the electron spectral function, $A(\mathbf{k}, \epsilon)$ using the following relations: $G^>_{\mathbf{k}}(\epsilon) = -iA(\mathbf{k}, \epsilon)[1 - n_F(\beta'\epsilon)]$, $G^<_{\mathbf{k}}(\epsilon) = iA(\mathbf{k}, \epsilon) n_F(\beta'\epsilon)$, $D^{l>}_{\nu,\mathbf{q}}(\omega) = -iA^l_\nu(\mathbf{q}, \omega)\left[1 + n_B(\beta\omega_\nu)\right]$ and $D^{l<}_{\nu,\mathbf{q}}(\omega) = -iA^l_\nu(\mathbf{q}, \omega) n_B(\beta\omega_\nu)$. Using $\mathrm{Im}(\omega \pm i\eta)^{-1} = \mp\pi\delta(\omega)$, we find same result as shown in Eq. (3.11)

$$\mathfrak{Im}\left[B_{\nu l}(\mathbf{q}, \mathbf{k}, \mathbf{k}')\right] = \pi \int \frac{d\omega}{2\pi} \int \frac{d\epsilon}{2\pi} \int \frac{d\epsilon'}{2\pi} \delta(\epsilon - \epsilon' + \omega) A^l_\nu(\mathbf{q}, \omega) A(k, \epsilon) A(k', \epsilon') \\ \times \left[\left(1 + n_B(\beta\omega)\right) \left(1 - n_F(\beta'\epsilon)\right) n_F(\beta'\epsilon') - n_B(\beta\omega) n_F(\beta'\epsilon) \left(1 - n_F(\beta'\epsilon')\right) \right] . \tag{C.17}$$

The first and second term on the right-hand side of Eq. (C.17) correspond to an electron scattering by, respectively, one-magnon emission and one-magnon absorption. For a non-interacting clean system, we have $A^l_\nu(\mathbf{q}, \omega) = 2\pi\delta(\omega - \omega^l_\nu(\mathbf{q}))$ and $A(\mathbf{k}, \epsilon) = 2\pi\delta(\epsilon - \epsilon_{\mathbf{k}})$. We assume that the common electronic temperature T' and the single electron energy $\epsilon_{\mathbf{k}}$ are both much smaller than the Fermi energy ϵ_F. Thus, we can treat the electron density of states as a

constant, i.e., D.

Using the following properties, i.e.,

$$n_F(x)\left[1-n_F(y)\right] = n_B(x-y)\left[n_F(y)-n_F(x)\right] \tag{C.18}$$

$$\int d\epsilon \left[n_F(\epsilon)-n_F(\epsilon+x)\right] = x \tag{C.19}$$

$$1+n_B(x) = -n_B(-x) \tag{C.20}$$

we can rewrite Eq. (C.17) as

$$\mathfrak{Im}\left[B_{\nu l}(\mathbf{q},\mathbf{k},\mathbf{k}')\right] = \pi D^2 \omega_\nu^l(\mathbf{q})\left[n_B(\beta'\omega_\nu^l(\mathbf{q})) - n_B(\beta\omega_\nu^l(\mathbf{q}))\right] \tag{C.21}$$

giving same result as in Eq. (3.12)

Bibliography

[1] Hiroto Adachi, Jun-ichiro Ohe, Saburo Takahashi, and Sadamichi Maekawa. Linear-response theory of spin seebeck effect in ferromagnetic insulators. *Physical Review B*, 83(9):094410, 2011.

[2] Hiroto Adachi, Ken-ichi Uchida, Eiji Saitoh, Jun-ichiro Ohe, Saburo Takahashi, and Sadamichi Maekawa. Gigantic enhancement of spin seebeck effect by phonon drag. *Applied Physics Letters*, 97(25):252506, 2010.

[3] Monika Aidelsburger. Measuring the chern number of hofstadter bands with bosonic atoms. In *APS Division of Atomic, Molecular and Optical Physics Meeting Abstracts*, volume 2015, pages J6–002, 2015.

[4] Kazuya Ando, Saburo Takahashi, Junichi Ieda, Yosuke Kajiwara, Hiroyasu Nakayama, Tatsuro Yoshino, Kazuya Harii, Yasunori Fujikawa, M Matsuo, S Maekawa, et al. Inverse spin-hall effect induced by spin pumping in metallic system. *Journal of applied physics*, 109(10):103913, 2011.

[5] Yoichi Ando. Topological insulator materials. *Journal of the Physical Society of Japan*, 82(10):102001, 2013.

[6] Ian Appelbaum, HD Drew, and MS Fuhrer. Proposal for a topological plasmon spin rectifier. *Applied Physics Letters*, 98(2):023103, 2011.

[7] R Arita, J Kuneš, AV Kozhevnikov, AG Eguiluz, and M Imada. Ab initio studies on the interplay between spin-orbit interaction and coulomb correlation in sr 2 iro 4 and ba 2 iro 4. *Physical review letters*, 108(8):086403, 2012.

[8] Mois I Aroyo, JM Perez-Mato, Danel Orobengoa, EMRE Tasci, Gemma de la Flor, and Asel Kirov. Crystallography online: Bilbao crystallographic server. *Bulg. Chem. Commun*, 43(2):183–197, 2011.

[9] Joseph E Avron, Ruedi Seiler, and Barry Simon. Homotopy and quantization in condensed matter physics. *Physical review letters*, 51(1):51, 1983.

[10] V Baltz, Aurelien Manchon, M Tsoi, T Moriyama, T Ono, and Y Tserkovnyak. Antiferromagnetic spintronics. *Reviews of Modern Physics*, 90(1):015005, 2018.

[11] Sumilan Banerjee, James Rowland, Onur Erten, and Mohit Randeria. Enhanced stability of skyrmions in two-dimensional chiral magnets with rashba spin-orbit coupling. *Physical Review X*, 4(3):031045, 2014.

[12] A Barman, Gianluca Gubbiotti, Sam Ladak, Adekunle Olusola Adeyeye, Maciej Krawczyk, Joachim Gräfe, Christoph Adelmann, Sorin Cotofana,

Azad Naeemi, Vitaliy I Vasyuchka, et al. The 2021 magnonics roadmap. *Journal of Physics: Condensed Matter*, 2021.

[13] Ryan Barnett. Edge-state instabilities of bosons in a topological band. *Physical Review A*, 88(6):063631, 2013.

[14] Ryan Barnett, Greg R Boyd, and Victor Galitski. Su (3) spin-orbit coupling in systems of ultracold atoms. *Physical review letters*, 109(23):235308, 2012.

[15] Jean Baptiste Joseph baron Fourier. *Théorie analytique de la chaleur*. Chez Firmin Didot, père et fils, 1822.

[16] Gerrit EW Bauer, Eiji Saitoh, and Bart J Van Wees. Spin caloritronics. *Nature materials*, 11(5):391–399, 2012.

[17] Scott A Bender and Yaroslav Tserkovnyak. Interfacial spin and heat transfer between metals and magnetic insulators. *Physical Review B*, 91(14):140402, 2015.

[18] B Andrei Bernevig. *Topological insulators and topological superconductors*. Princeton university press, 2013.

[19] B Andrei Bernevig, Taylor L Hughes, and Shou-Cheng Zhang. Quantum spin hall effect and topological phase transition in hgte quantum wells. *science*, 314(5806):1757–1761, 2006.

[20] Michael Victor Berry. Quantal phase factors accompanying adiabatic changes. *Proceedings of the Royal Society of London. A. Mathematical and Physical Sciences*, 392(1802):45–57, 1984.

[21] Felix Bloch. Zur theorie des ferromagnetismus. *Zeitschrift für Physik*, 61(3-4):206–219, 1930.

[22] AN Bogdanov and UK Rößler. Chiral symmetry breaking in magnetic thin films and multilayers. *Physical review letters*, 87(3):037203, 2001.

[23] NN Bogoljubov, Vladimir Veniaminovic Tolmachov, and DV Širkov. A new method in the theory of superconductivity. *Fortschritte der physik*, 6(11-12):605–682, 1958.

[24] Marin Bukov, Michael Kolodrubetz, and Anatoli Polkovnikov. Schrieffer-wolff transformation for periodically driven systems: Strongly correlated systems with artificial gauge fields. *Physical review letters*, 116(12):125301, 2016.

[25] Yua A Bychkov. Properties of 2d electron gas with lifted spectral degeneracy. *JETP lett.*, 39(2):78–81, 1984.

[26] Cui-Zu Chang, Jinsong Zhang, Xiao Feng, Jie Shen, Zuocheng Zhang, Minghua Guo, Kang Li, Yunbo Ou, Pang Wei, Li-Li Wang, et al. Experimental observation of the quantum anomalous hall effect in a magnetic topological insulator. *Science*, 340(6129):167–170, 2013.

[27] Gang Chen and Michael Hermele. Magnetic orders and topological phases from f-d exchange in pyrochlore iridates. *Physical Review B*, 86(23):235129, 2012.

[28] Hua Chen, Qian Niu, and Allan H MacDonald. Anomalous hall effect arising from noncollinear antiferromagnetism. *Physical review letters*, 112(1):017205, 2014.

[29] Qi Chen, Hsiang-Hsuan Hung, Xiang Hu, and Gregory A Fiete. Correlation effects in pyrochlore iridate thin films grown along the [111] direction. *Physical Review B*, 92(8):085145, 2015.

[30] Ran Cheng, Satoshi Okamoto, and Di Xiao. Spin nernst effect of magnons in collinear antiferromagnets. *Physical review letters*, 117(21):217202, 2016.

[31] Ran Cheng, Jiang Xiao, Qian Niu, and Arne Brataas. Spin pumping and spin-transfer torques in antiferromagnets. *Physical review letters*, 113(5):057601, 2014.

[32] R Chisnell, JS Helton, DE Freedman, DK Singh, RI Bewley, DG Nocera, and YS Lee. Topological magnon bands in a kagome lattice ferromagnet. *Physical review letters*, 115(14):147201, 2015.

[33] Andrii V Chumak, Alexander A Serga, and Burkard Hillebrands. Magnon transistor for all-magnon data processing. *Nature communications*, 5(1):1–8, 2014.

[34] Andrii V Chumak, Vitaliy I Vasyuchka, Alexander A Serga, and Burkard Hillebrands. Magnon spintronics. *Nature Physics*, 11(6):453–461, 2015.

[35] J Clerk Maxwell. On the dynamical theory of gases. *Philosophical Transactions of the Royal Society of London Series I*, 157:49–88, 1867.

[36] JHP Colpa. Diagonalization of the quadratic boson hamiltonian. *Physica A: Statistical Mechanics and its Applications*, 93(3-4):327–353, 1978.

[37] Peter Debye. Zur theorie der spezifischen wärmen. *Annalen der Physik*, 344(14):789–839, 1912.

[38] Adrian G Del Maestro and Michel JP Gingras. Quantum spin fluctuations in the dipolar heisenberg-like rare earth pyrochlores. *Journal of Physics: Condensed Matter*, 16(20):3339, 2004.

[39] Yujun Deng, Yijun Yu, Meng Zhu Shi, Zhongxun Guo, Zihan Xu, Jing Wang, Xian Hui Chen, and Yuanbo Zhang. Quantum anomalous hall effect in intrinsic magnetic topological insulator mnbi2te4. *Science*, 367(6480):895–900, 2020.

[40] Kai Di, Vanessa Li Zhang, Hock Siah Lim, Ser Choon Ng, Meng Hau Kuok, Jiawei Yu, Jungbum Yoon, Xuepeng Qiu, and Hyunsoo Yang. Direct observation of the dzyaloshinskii-moriya interaction in a pt/co/ni film. *Physical review letters*, 114(4):047201, 2015.

[41] P Di Pietro, M Ortolani, O Limaj, A Di Gaspare, V Giliberti, F Giorgianni, M Brahlek, N Bansal, N Koirala, Seongshik Oh, et al. Observa-

tion of dirac plasmons in a topological insulator. *Nature nanotechnology*, 8(8):556–560, 2013.

[42] Steven M Disseler. Direct evidence for the all-in/all-out magnetic structure in the pyrochlore iridates from muon spin relaxation. *Physical Review B*, 89(14):140413, 2014.

[43] Steven M Disseler, Chetan Dhital, A Amato, SR Giblin, Clarina de la Cruz, Stephen D Wilson, and MJ Graf. Magnetic order in the pyrochlore iridates a 2 ir 2 o 7 (a= y, yb). *Physical Review B*, 86(1):014428, 2012.

[44] Hayato Doki, Masatoshi Akazawa, Hyun-Yong Lee, Jung Hoon Han, Kaori Sugii, Masaaki Shimozawa, Naoki Kawashima, Migaku Oda, Hiroyuki Yoshida, and Minoru Yamashita. Spin thermal hall conductivity of a kagome antiferromagnet. *Physical review letters*, 121(9):097203, 2018.

[45] C Donnerer, MC Rahn, M Moretti Sala, JG Vale, D Pincini, J Strempfer, M Krisch, D Prabhakaran, AT Boothroyd, and DF McMorrow. All-in–all-out magnetic order and propagating spin waves in sm 2 ir 2 o 7. *Physical review letters*, 117(3):037201, 2016.

[46] Chunhui Du, Toeno Van der Sar, Tony X Zhou, Pramey Upadhyaya, Francesco Casola, Huiliang Zhang, Mehmet C Onbasli, Caroline A Ross, Ronald L Walsworth, Yaroslav Tserkovnyak, et al. Control and local measurement of the spin chemical potential in a magnetic insulator. *Science*, 357(6347):195–198, 2017.

[47] Igor Dzyaloshinsky. A thermodynamic theory of "weak" ferromagnetism of antiferromagnetics. *Journal of physics and chemistry of solids*, 4(4):241–255, 1958.

[48] Maged Elhajal, Benjamin Canals, Raimon Sunyer, and Claudine Lacroix. Ordering in the pyrochlore antiferromagnet due to dzyaloshinsky-moriya interactions. *Physical Review B*, 71(9):094420, 2005.

[49] Amalio Fernández-Pacheco, Elena Vedmedenko, Fanny Ummelen, Rhodri Mansell, Dorothée Petit, and Russell P Cowburn. Symmetry-breaking interlayer dzyaloshinskii–moriya interactions in synthetic antiferromagnets. *Nature materials*, 18(7):679–684, 2019.

[50] Albert Fert, Nicolas Reyren, and Vincent Cros. Magnetic skyrmions: advances in physics and potential applications. *Nature Reviews Materials*, 2(7):17031, 2017.

[51] Benedetta Flebus, Ka Shen, Takashi Kikkawa, Ken-ichi Uchida, Zhiyong Qiu, Eiji Saitoh, Rembert A Duine, and Gerrit EW Bauer. Magnon-polaron transport in magnetic insulators. *Physical Review B*, 95(14):144420, 2017.

[52] Benedetta Flebus, Yaroslav Tserkovnyak, and Gregory A Fiete. Interfacial spin seebeck effect in noncollinear magnetic systems. *Physical Review B*, 99(22):224410, 2019.

[53] Michael Först, Cristian Manzoni, Stefan Kaiser, Yasuhide Tomioka, Yoshinori Tokura, Roberto Merlin, and Andrea Cavalleri. Nonlinear phononics as an ultrafast route to lattice control. *Nature Physics*, 7(11):854–856, 2011.

[54] R Franz and G Wiedemann. Ueber die wärme-leitungsfähigkeit der metalle. *Annalen der Physik*, 165(8):497–531, 1853.

[55] Y Fujishiro, N Kanazawa, T Nakajima, XZ Yu, K Ohishi, Y Kawamura, K Kakurai, T Arima, H Mitamura, A Miyake, et al. Topological transitions among skyrmion-and hedgehog-lattice states in cubic chiral magnets. *Nature communications*, 10(1):1–8, 2019.

[56] Takahiro Fukui, Yasuhiro Hatsugai, and Hiroshi Suzuki. Chern numbers in discretized brillouin zone: efficient method of computing (spin) hall conductances. *Journal of the Physical Society of Japan*, 74(6):1674–1677, 2005.

[57] Ara Go, William Witczak-Krempa, Gun Sang Jeon, Kwon Park, and Yong Baek Kim. Correlation effects on 3d topological phases: from bulk to boundary. *Physical review letters*, 109(6):066401, 2012.

[58] Gyungchoon Go, Se Kwon Kim, and Kyung-Jin Lee. Topological magnon-phonon hybrid excitations in two-dimensional ferromagnets with tunable chern numbers. *Physical review letters*, 123(23):237207, 2019.

[59] Helen V Gomonay and Vadim M Loktev. Spin transfer and current-induced switching in antiferromagnets. *Physical Review B*, 81(14):144427, 2010.

[60] O Gomonay, T Jungwirth, and J Sinova. Staggering antiferromagnetic domain wall velocity in a staggered spin-orbit field. *arXiv preprint arXiv:1602.06766*, 2016.

[61] F Duncan M Haldane. Model for a quantum hall effect without landau levels: Condensed-matter realization of the" parity anomaly". *Physical review letters*, 61(18):2015, 1988.

[62] M Zahid Hasan and Charles L Kane. Colloquium: topological insulators. *Reviews of modern physics*, 82(4):3045, 2010.

[63] Arsalan Hashemi, Hannu-Pekka Komsa, Martti Puska, and Arkady V Krasheninnikov. Vibrational properties of metal phosphorus trichalcogenides from first-principles calculations. *The Journal of Physical Chemistry C*, 121(48):27207–27217, 2017.

[64] Moosa Hatami, Gerrit EW Bauer, Qinfang Zhang, and Paul J Kelly. Thermal spin-transfer torque in magnetoelectronic devices. *Physical review letters*, 99(6):066603, 2007.

[65] Yasuhiro Hatsugai. Chern number and edge states in the integer quantum hall effect. *Physical review letters*, 71(22):3697, 1993.

[66] Yasuhiro Hatsugai. Edge states in the integer quantum hall effect and the riemann surface of the bloch function. *Physical Review B*, 48(16):11851, 1993.

[67] Qing Lin He, Lei Pan, Alexander L Stern, Edward C Burks, Xiaoyu Che, Gen Yin, Jing Wang, Biao Lian, Quan Zhou, Eun Sang Choi, et al. Chiral majorana fermion modes in a quantum anomalous hall insulator–superconductor structure. *Science*, 357(6348):294–299, 2017.

[68] Kasra Hejazi, Jianpeng Liu, and Leon Balents. Floquet spin and spin-orbital hamiltonians and doublon-holon generations in periodically driven mott insulators. *Physical Review B*, 99(20):205111, 2019.

[69] Tomoki Hirosawa, Sebastián A Díaz, Jelena Klinovaja, and Daniel Loss. Magnonic quadrupole topological insulator in antiskyrmion crystals. *Physical Review Letters*, 125(20):207204, 2020.

[70] Max Hirschberger, Jason W Krizan, RJ Cava, and NP Ong. Large thermal hall conductivity of neutral spin excitations in a frustrated quantum magnet. *Science*, 348(6230):106–109, 2015.

[71] T Holstein and Hl Primakoff. Field dependence of the intrinsic domain magnetization of a ferromagnet. *Physical Review*, 58(12):1098, 1940.

[72] Xiang Hu, Andreas Rüegg, and Gregory A Fiete. Topological phases in layered pyrochlore oxide thin films along the [111] direction. *Physical Review B*, 86(23):235141, 2012.

[73] Xiang Hu, Zhicheng Zhong, and Gregory A Fiete. First principles prediction of topological phases in thin films of pyrochlore iridates. *Scientific reports*, 5(1):1–7, 2015.

[74] CM Jaworski, J Yang, S Mack, DD Awschalom, JP Heremans, and RC Myers. Observation of the spin-seebeck effect in a ferromagnetic semiconductor. *Nature materials*, 9(11):898–903, 2010.

[75] FJ Jedema, HB Heersche, AT Filip, JJA Baselmans, and BJ Van Wees. Electrical detection of spin precession in a metallic mesoscopic spin valve. *Nature*, 416(6882):713–716, 2002.

[76] Friso Jacobus Jedema, AT Filip, and BJ Van Wees. Electrical spin injection and accumulation at room temperature in an all-metal mesoscopic spin valve. *Nature*, 410(6826):345–348, 2001.

[77] Yuanjun Jin, Rui Wang, and Hu Xu. Recipe for dirac phonon states with a quantized valley berry phase in two-dimensional hexagonal lattices. *Nano letters*, 18(12):7755–7760, 2018.

[78] Mark Johnson and RH Silsbee. Thermodynamic analysis of interfacial transport and of the thermomagnetoelectric system. *Physical Review B*, 35(10):4959, 1987.

[79] PA Joy and S Vasudevan. Magnetism in the layered transition-metal thiophosphates m ps 3 (m= mn, fe, and ni). *Physical Review B*, 46(9):5425, 1992.

[80] T Jungwirth, J Sinova, Aurelien Manchon, X Marti, J Wunderlich, and C Felser. The multiple directions of antiferromagnetic spintronics. *Nature Physics*, 14(3):200–203, 2018.

[81] Tomas Jungwirth, X Marti, P Wadley, and J Wunderlich. Antiferromagnetic spintronics. *Nature nanotechnology*, 11(3):231–241, 2016.

[82] Yu Kagan and LA Maksimov. Anomalous hall effect for the phonon heat conductivity in paramagnetic dielectrics. *Physical review letters*, 100(14):145902, 2008.

[83] Y Kajiwara, K Harii, S Takahashi, Jun-ichiro Ohe, K Uchida, M Mizuguchi, H Umezawa, H Kawai, Kazuya Ando, K Takanashi, et al. Transmission of electrical signals by spin-wave interconversion in a magnetic insulator. *Nature*, 464(7286):262–266, 2010.

[84] Junjiro Kanamori. Theory of the magnetic properties of ferrous and cobaltous oxides, i. *Progress of Theoretical Physics*, 17(2):177–196, 1957.

[85] Charles L Kane and Eugene J Mele. Quantum spin hall effect in graphene. *Physical review letters*, 95(22):226801, 2005.

[86] Mehdi Kargarian and Gregory A. Fiete. Topological crystalline insulators in transition metal oxides. *Phys. Rev. Lett.*, 110:156403, 2013.

[87] Mehdi Kargarian and Gregory A Fiete. Topological crystalline insulators in transition metal oxides. *Physical review letters*, 110(15):156403, 2013.

[88] Mehdi Kargarian, Jun Wen, and Gregory A Fiete. Competing exotic topological insulator phases in transition-metal oxides on the pyrochlore lattice with distortion. *Physical Review B*, 83(16):165112, 2011.

[89] Torsten Karzig, Charles-Edouard Bardyn, Netanel H Lindner, and Gil Refael. Topological polaritons. *Physical Review X*, 5(3):031001, 2015.

[90] Y Kasahara, K Sugii, T Ohnishi, M Shimozawa, M Yamashita, N Kurita, H Tanaka, J Nasu, Y Motome, T Shibauchi, et al. Unusual thermal hall effect in a kitaev spin liquid candidate α- rucl 3. *Physical review letters*, 120(21):217205, 2018.

[91] Hosho Katsura, Naoto Nagaosa, and Patrick A Lee. Theory of the thermal hall effect in quantum magnets. *Physical review letters*, 104(6):066403, 2010.

[92] Frederic Keffer. Moriya interaction and the problem of the spin arrangements in β mns. *Physical Review*, 126(3):896, 1962.

[93] Alexander B Khanikaev, S Hossein Mousavi, Wang-Kong Tse, Mehdi Kargarian, Allan H MacDonald, and Gennady Shvets. Photonic topological insulators. *Nature materials*, 12(3):233–239, 2013.

[94] Takashi Kikkawa, Ka Shen, Benedetta Flebus, Rembert A Duine, Kenichi Uchida, Zhiyong Qiu, Gerrit EW Bauer, and Eiji Saitoh. Magnon polarons in the spin seebeck effect. *Physical review letters*, 117(20):207203, 2016.

[95] BJ Kim, Hosub Jin, SJ Moon, J-Y Kim, B-G Park, CS Leem, Jaejun Yu, TW Noh, C Kim, S-J Oh, et al. Novel j eff= 1/2 mott state induced by relativistic spin-orbit coupling in sr 2 iro 4. *Physical review letters*, 101(7):076402, 2008.

[96] BJ Kim, H Ohsumi, T Komesu, S Sakai, T Morita, H Takagi, and T-h Arima. Phase-sensitive observation of a spin-orbital mott state in sr2iro4. *Science*, 323(5919):1329–1332, 2009.

[97] Duck-Ho Kim, Mitsutaka Haruta, Hye-Won Ko, Gyungchoon Go, Hyeon-Jong Park, Tomoe Nishimura, Dae-Yun Kim, Takaya Okuno, Yuushou Hirata, Yasuhiro Futakawa, et al. Bulk dzyaloshinskii–moriya interaction in amorphous ferrimagnetic alloys. *Nature materials*, 18(7):685–690, 2019.

[98] Se Kwon Kim, Héctor Ochoa, Ricardo Zarzuela, and Yaroslav Tserkovnyak. Realization of the haldane-kane-mele model in a system of localized spins. *Physical review letters*, 117(22):227201, 2016.

[99] Takashi Kimura, Y Otani, T Sato, S Takahashi, and S Maekawa. Room-temperature reversible spin hall effect. *Physical review letters*, 98(15):156601, 2007.

[100] Charles Kittel and Ching-yao Fong. *Quantum theory of solids*, volume 5. Wiley New York, 1963.

[101] S Klembt, TH Harder, OA Egorov, K Winkler, R Ge, MA Bandres, M Emmerling, L Worschech, TCH Liew, M Segev, et al. Exciton-polariton topological insulator. *Nature*, 562(7728):552–556, 2018.

[102] K v Klitzing, Gerhard Dorda, and Michael Pepper. New method for high-accuracy determination of the fine-structure constant based on quantized hall resistance. *Physical review letters*, 45(6):494, 1980.

[103] VV Kruglyak, SO Demokritov, and D Grundler. Magnonics. *Journal of Physics D: Applied Physics*, 43(26):264001, 2010.

[104] Ryogo Kubo, Mario Yokota, and Sadao Nakajima. Statistical-mechanical theory of irreversible processes. ii. response to thermal disturbance. *Journal of the Physical Society of Japan*, 12(11):1203–1211, 1957.

[105] Pontus Laurell and Gregory A Fiete. Topological magnon bands and unconventional superconductivity in pyrochlore iridate thin films. *Physical review letters*, 118(17):177201, 2017.

[106] Pontus Laurell and Gregory A Fiete. Magnon thermal hall effect in kagome antiferromagnets with dzyaloshinskii-moriya interactions. *Physical Review B*, 98(9):094419, 2018.

[107] Eric Kin-Ho Lee, Subhro Bhattacharjee, and Yong Baek Kim. Magnetic excitation spectra in pyrochlore iridates. *Physical Review B*, 87(21):214416, 2013.

[108] Patrick A Lee, Naoto Nagaosa, and Xiao-Gang Wen. Doping a mott insulator: Physics of high-temperature superconductivity. *Reviews of modern physics*, 78(1):17, 2006.

[109] Benjamin Lenk, Henning Ulrichs, Fabian Garbs, and Markus Münzenberg. The building blocks of magnonics. *Physics Reports*, 507(4-5):107–136, 2011.

[110] Michael Levin and Ady Stern. Fractional topological insulators. *Physical review letters*, 103(19):196803, 2009.

[111] Bo Li, Alexander Mook, Aldo Raeliarijaona, and Alexey A Kovalev. Magnonic analog of the edelstein effect in antiferromagnetic insulators. *Physical Review B*, 101(2):024427, 2020.

[112] Bo Li, Shane Sandhoefner, and Alexey A Kovalev. Intrinsic spin nernst effect of magnons in a noncollinear antiferromagnet. *Physical Review Research*, 2(1):013079, 2020.

[113] Fei-Ye Li, Yao-Dong Li, Yong Baek Kim, Leon Balents, Yue Yu, and Gang Chen. Weyl magnons in breathing pyrochlore antiferromagnets. *Nature communications*, 7(1):1–7, 2016.

[114] Tian Liang, Quinn Gibson, Mazhar N Ali, Minhao Liu, RJ Cava, and NP Ong. Ultrahigh mobility and giant magnetoresistance in the dirac semimetal cd 3 as 2. *Nature materials*, 14(3):280–284, 2015.

[115] Tian Liang, Timothy H Hsieh, Jun J Ishikawa, Satoru Nakatsuji, Liang Fu, and Nai Phuan Ong. Orthogonal magnetization and symmetry breaking in pyrochlore iridate eu 2 ir 2 o 7. *Nature Physics*, 13(6):599, 2017.

[116] Michael Lohse, Christian Schweizer, Oded Zilberberg, Monika Aidelsburger, and Immanuel Bloch. A thouless quantum pump with ultracold bosonic atoms in an optical superlattice. *Nature Physics*, 12(4):350–354, 2016.

[117] Bowen Ma, Benedetta Flebus, and Gregory A Fiete. Longitudinal spin seebeck effect in pyrochlore iridates with bulk and interfacial dzyaloshinskii-moriya interaction. *Physical Review B*, 101(3):035104, 2020.

[118] J. Maciejko and G. A. Fiete. Fractionalized topological insulators. *Nat. Phys.*, 11:385, 2015.

[119] Joseph Maciejko, Victor Chua, and Gregory A. Fiete. Topological order in a correlated three-dimensional topological insulator. *Phys. Rev. Lett.*, 112:016404, 2014.

[120] Joseph Maciejko, Victor Chua, and Gregory A Fiete. Topological order in a correlated three-dimensional topological insulator. *Physical review*

letters, 112(1):016404, 2014.

[121] Joseph Maciejko and Andreas Rüegg. Topological order in a correlated chern insulator. *Physical Review B*, 88(24):241101, 2013.

[122] Aurelien Manchon, Hyun Cheol Koo, Junsaku Nitta, SM Frolov, and RA Duine. New perspectives for rashba spin–orbit coupling. *Nature materials*, 14(9):871–882, 2015.

[123] Kazuyuki Matsuhira, Makoto Wakeshima, Yukio Hinatsu, and Seishi Takagi. Metal–insulator transitions in pyrochlore oxides ln 2ir2o7. *Journal of the Physical Society of Japan*, 80(9):094701, 2011.

[124] Kazuyuki Matsuhira, Makoto Wakeshima, Ryo Nakanishi, Takaaki Yamada, Akira Nakamura, Wataru Kawano, Seishi Takagi, and Yukio Hinatsu. Metal–insulator transition in pyrochlore iridates ln 2ir2o7 (ln= nd, sm, and eu). *Journal of the Physical Society of Japan*, 76(4):043706, 2007.

[125] Ryo Matsumoto and Shuichi Murakami. Rotational motion of magnons and the thermal hall effect. *Physical Review B*, 84(18):184406, 2011.

[126] Sibylle Meyer, Y-T Chen, Sebastian Wimmer, Matthias Althammer, Tobias Wimmer, Richard Schlitz, Stephan Geprägs, Hans Huebl, Diemo Ködderitzsch, H Ebert, et al. Observation of the spin nernst effect. *Nature materials*, 16(10):977–981, 2017.

[127] Alexander Mook, Jürgen Henk, and Ingrid Mertig. Edge states in topological magnon insulators. *Physical Review B*, 90(2):024412, 2014.

[128] Alexander Mook, Jürgen Henk, and Ingrid Mertig. Thermal hall effect in noncollinear coplanar insulating antiferromagnets. *Physical Review B*, 99(1):014427, 2019.

[129] Joel E Moore. The birth of topological insulators. *Nature*, 464(7286):194, 2010.

[130] Tôru Moriya. Anisotropic superexchange interaction and weak ferromagnetism. *Physical review*, 120(1):91, 1960.

[131] Tôru Moriya. New mechanism of anisotropic superexchange interaction. *Physical Review Letters*, 4(5):228, 1960.

[132] Sebastian Mühlbauer, Benedikt Binz, F Jonietz, Christian Pfleiderer, Achim Rosch, Anja Neubauer, Robert Georgii, and Peter Böni. Skyrmion lattice in a chiral magnet. *Science*, 323(5916):915–919, 2009.

[133] Kouki Nakata, Se Kwon Kim, Jelena Klinovaja, and Daniel Loss. Magnonic topological insulators in antiferromagnets. *Physical Review B*, 96(22):224414, 2017.

[134] Kouki Nakata, Pascal Simon, and Daniel Loss. Wiedemann-franz law for magnon transport. *Physical Review B*, 92(13):134425, 2015.

[135] Branislav K Nikolić, Liviu P Zârbo, and Satofumi Souma. Imaging mesoscopic spin hall flow: Spatial distribution of local spin currents and spin densities in and out of multiterminal spin-orbit coupled semiconductor nanostructures. *Physical Review B*, 73(7):075303, 2006.

[136] Qian Niu, Ds J Thouless, and Yong-Shi Wu. Quantized hall conductance as a topological invariant. *Physical Review B*, 31(6):3372, 1985.

[137] Tobia F Nova, Andrea Cartella, Alice Cantaluppi, Michael Först, Davide Bossini, Rostislav V Mikhaylovskiy, Aleksei V Kimel, Roberto Merlin, and Andrea Cavalleri. An effective magnetic field from optically driven phonons. *Nature Physics*, 13(2):132–136, 2017.

[138] Yuichi Ohnuma, Hiroto Adachi, Eiji Saitoh, and Sadamichi Maekawa. Spin seebeck effect in antiferromagnets and compensated ferrimagnets. *Physical Review B*, 87(1):014423, 2013.

[139] Y Onose, T Ideue, H Katsura, Y Shiomi, N Nagaosa, and Y Tokura. Observation of the magnon hall effect. *Science*, 329(5989):297–299, 2010.

[140] SA Owerre. Dirac magnon nodal loops in quasi-2d quantum magnets. *Scientific reports*, 7(1):1–9, 2017.

[141] SA Owerre. Floquet topological magnons. *Journal of Physics Communications*, 1(2):021002, 2017.

[142] SA Owerre. Magnonic analogs of topological dirac semimetals. *Journal of Physics Communications*, 1(2):025007, 2017.

[143] SA Owerre. Noncollinear antiferromagnetic haldane magnon insulator. *Journal of Applied Physics*, 121(22):223904, 2017.

[144] SA Owerre. Topological thermal hall effect in frustrated kagome antiferromagnets. *Physical Review B*, 95(1):014422, 2017.

[145] SA Owerre. Weyl magnons in noncoplanar stacked kagome antiferromagnets. *Physical Review B*, 97(9):094412, 2018.

[146] SA Owerre, Paula Mellado, and G Baskaran. Photoinduced floquet topological magnons in kitaev magnets. *EPL (Europhysics Letters)*, 126(2):27002, 2019.

[147] Tomoki Ozawa, Hannah M Price, Alberto Amo, Nathan Goldman, Mohammad Hafezi, Ling Lu, Mikael C Rechtsman, David Schuster, Jonathan Simon, Oded Zilberberg, et al. Topological photonics. *Reviews of Modern Physics*, 91(1):015006, 2019.

[148] Sergey S Pershoguba, Saikat Banerjee, JC Lashley, Jihwey Park, Hans Ågren, Gabriel Aeppli, and Alexander V Balatsky. Dirac magnons in honeycomb ferromagnets. *Physical Review X*, 8(1):011010, 2018.

[149] Dmytro Pesin and Leon Balents. Mott physics and band topology in materials with strong spin–orbit interaction. *Nature Physics*, 6(5):376–381, 2010.

[150] Emil Prodan and Camelia Prodan. Topological phonon modes and their role in dynamic instability of microtubules. *Physical review letters*, 103(24):248101, 2009.

[151] Alireza Qaiumzadeh, Ivan A Ado, Rembert A Duine, Mikhail Titov, and Arne Brataas. Theory of the interfacial dzyaloshinskii-moriya interaction in rashba antiferromagnets. *Physical review letters*, 120(19):197202, 2018.

[152] Xiao-Liang Qi, Taylor L Hughes, and Shou-Cheng Zhang. Topological field theory of time-reversal invariant insulators. *Physical Review B*, 78(19):195424, 2008.

[153] Xiao-Liang Qi and Shou-Cheng Zhang. Topological insulators and superconductors. *Reviews of Modern Physics*, 83(4):1057, 2011.

[154] Jeffrey G Rau, Eric Kin-Ho Lee, and Hae-Young Kee. Spin-orbit physics giving rise to novel phases in correlated systems: Iridates and related materials. *Annual Review of Condensed Matter Physics*, 7:195–221, 2016.

[155] SM Rezende, RL Rodríguez-Suárez, and A Azevedo. Theory of the spin seebeck effect in antiferromagnets. *Physical Review B*, 93(1):014425, 2016.

[156] James Rowland, Sumilan Banerjee, and Mohit Randeria. Skyrmions in chiral magnets with rashba and dresselhaus spin-orbit coupling. *Physical*

Review B, 93(2):020404, 2016.

[157] Andreas Rückriegel, Arne Brataas, and Rembert A Duine. Bulk and edge spin transport in topological magnon insulators. *Physical Review B*, 97(8):081106, 2018.

[158] Andreas Rüegg and Gregory A Fiete. Topological order and semions in a strongly correlated quantum spin hall insulator. *Physical review letters*, 108(4):046401, 2012.

[159] H Sagayama, D Uematsu, T-h Arima, K Sugimoto, JJ Ishikawa, E O'farrell, and S Nakatsuji. Determination of long-range all-in-all-out ordering of ir 4+ moments in a pyrochlore iridate eu 2 ir 2 o 7 by resonant x-ray diffraction. *Physical Review B*, 87(10):100403, 2013.

[160] E Saitoh, M Ueda, H Miyajima, and G Tatara. Conversion of spin current into charge current at room temperature: Inverse spin-hall effect. *Applied physics letters*, 88(18):182509, 2006.

[161] Rhine Samajdar, Mathias S Scheurer, Shubhayu Chatterjee, Haoyu Guo, Cenke Xu, and Subir Sachdev. Enhanced thermal hall effect in the square-lattice néel state. *Nature Physics*, 15(12):1290–1294, 2019.

[162] Robert Schaffer, Eric Kin-Ho Lee, Bohm-Jung Yang, and Yong Baek Kim. Recent progress on correlated electron systems with strong spin–orbit coupling. *Reports on Progress in Physics*, 79(9):094504, 2016.

[163] Max C Shapiro, Scott C Riggs, Matthew B Stone, Clarina R de la Cruz, Songxue Chi, Andrey A Podlesnyak, and Ian R Fisher. Structure and magnetic properties of the pyrochlore iridate y 2 ir 2 o 7. *Physical Review B*, 85(21):214434, 2012.

[164] L Sheng, DN Sheng, and CS Ting. Theory of the phonon hall effect in paramagnetic dielectrics. *Physical review letters*, 96(15):155901, 2006.

[165] Junren Shi, Ping Zhang, Di Xiao, and Qian Niu. Proper definition of spin current in spin-orbit coupled systems. *Physical review letters*, 96(7):076604, 2006.

[166] Hiroshi Shinaoka, Shintaro Hoshino, Matthias Troyer, and Philipp Werner. Phase diagram of pyrochlore iridates: all-in–all-out magnetic ordering and non-fermi-liquid properties. *Physical review letters*, 115(15):156401, 2015.

[167] Hiroshi Shinaoka, Takashi Miyake, and Shoji Ishibashi. Noncollinear magnetism and spin-orbit coupling in 5 d pyrochlore oxide cd 2 os 2 o 7. *Physical review letters*, 108(24):247204, 2012.

[168] Ryuichi Shindou, Ryo Matsumoto, Shuichi Murakami, and Jun-ichiro Ohe. Topological chiral magnonic edge mode in a magnonic crystal. *Physical Review B*, 87(17):174427, 2013.

[169] Y Shiomi, R Takashima, and E Saitoh. Experimental evidence consistent with a magnon nernst effect in the antiferromagnetic insulator mnps

3. *Physical Review B*, 96(13):134425, 2017.

[170] Jairo Sinova, Sergio O Valenzuela, J Wunderlich, CH Back, and T Jungwirth. Spin hall effects. *Reviews of Modern Physics*, 87(4):1213, 2015.

[171] Abraham Slachter, Frank Lennart Bakker, Jean-Paul Adam, and Bart Jan van Wees. Thermally driven spin injection from a ferromagnet into a non-magnetic metal. *Nature Physics*, 6(11):879–882, 2010.

[172] Libor Šmejkal, Yuriy Mokrousov, Binghai Yan, and Allan H MacDonald. Topological antiferromagnetic spintronics. *Nature physics*, 14(3):242–251, 2018.

[173] Tudor D Stanescu, Victor Galitski, JY Vaishnav, Charles W Clark, and S Das Sarma. Topological insulators and metals in atomic optical lattices. *Physical Review A*, 79(5):053639, 2009.

[174] M-T Suzuki, Takashi Koretsune, Masayuki Ochi, and Ryotaro Arita. Cluster multipole theory for anomalous hall effect in antiferromagnets. *Physical Review B*, 95(9):094406, 2017.

[175] Silvia Tacchi, RE Troncoso, Martina Ahlberg, Gianluca Gubbiotti, Marco Madami, Johan Åkerman, and Pedro Landeros. Interfacial dzyaloshinskii-moriya interaction in pt/cofeb films: effect of the heavy-metal thickness. *Physical review letters*, 118(14):147201, 2017.

[176] Nobuyuki Taira, Makoto Wakeshima, and Yukio Hinatsu. Magnetic properties of iridium pyrochlores r2ir2o7 (r= y, sm, eu and lu). *Journal of Physics: Condensed Matter*, 13(23):5527, 2001.

[177] Ryuji Takahashi and Naoto Nagaosa. Berry curvature in magnon-phonon hybrid systems. *Physical review letters*, 117(21):217205, 2016.

[178] Saburo Takahashi and Sadamichi Maekawa. Spin current in metals and superconductors. *Journal of the Physical Society of Japan*, 77(3):031009–031009, 2008.

[179] Fukui Takahiro, Hatsugai Yasuhiro, and Suzuki Hiroshi. Chern numbers in discretized brillouin zone: Efficient method of computing (spin) hall conductances. *Journal of the Physical Society of Japan*, 2013.

[180] Toshiaki Tanigaki, Kiyou Shibata, Naoya Kanazawa, Xiuzhen Yu, Yoshinori Onose, Hyun Soon Park, Daisuke Shindo, and Yoshinori Tokura. Real-space observation of short-period cubic lattice of skyrmions in mnge. *Nano letters*, 15(8):5438–5442, 2015.

[181] David J Thouless, Mahito Kohmoto, M Peter Nightingale, and Marcel den Nijs. Quantized hall conductance in a two-dimensional periodic potential. *Physical review letters*, 49(6):405, 1982.

[182] K Uchida, S Takahashi, K Harii, J Ieda, W Koshibae, Kazuya Ando, S Maekawa, and E Saitoh. Observation of the spin seebeck effect. *Nature*, 455(7214):778–781, 2008.

[183] Ken-Ichi Uchida. Transport phenomena in spin caloritronics. *Proceedings of the Japan Academy, Series B*, 97(2):69–88, 2021.

[184] Ken-ichi Uchida, Hiroto Adachi, Takeru Ota, Hiroyasu Nakayama, Sadamichi Maekawa, and Eiji Saitoh. Observation of longitudinal spin-seebeck effect in magnetic insulators. *Applied Physics Letters*, 97(17):172505, 2010.

[185] Kentaro Ueda, Ryoma Kaneko, Hiroaki Ishizuka, Jun Fujioka, Naoto Nagaosa, and Yoshinori Tokura. Spontaneous hall effect in the weyl semimetal candidate of all-in all-out pyrochlore iridate. *Nature communications*, 9(1):3032, 2018.

[186] Kentaro Ueda, Taekoo Oh, Bohm-Jung Yang, Ryoma Kaneko, Jun Fujioka, Naoto Nagaosa, and Yoshinori Tokura. Magnetic-field induced multiple topological phases in pyrochlore iridates with mott criticality. *Nature communications*, 8(1):1–7, 2017.

[187] JG Valatin. Comments on the theory of superconductivity. *Il Nuovo Cimento (1955-1965)*, 7(6):843–857, 1958.

[188] Sergio O Valenzuela and M Tinkham. Direct electronic measurement of the spin hall effect. *Nature*, 442(7099):176, 2006.

[189] JL Van Hemmen. A note on the diagonalization of quadratic boson and fermion hamiltonians. *Zeitschrift für Physik B Condensed Matter*, 38(3):271–277, 1980.

[190] Xiangang Wan, Ari Turner, Ashvin Vishwanath, and Sergey Y Savrasov. Electronic structure of pyrochlore iridates: from topological dirac metal to mott insulator. *arXiv preprint arXiv:1007.0016*, 2010.

[191] Xiangang Wan, Ari M Turner, Ashvin Vishwanath, and Sergey Y Savrasov. Topological semimetal and fermi-arc surface states in the electronic structure of pyrochlore iridates. *Physical Review B*, 83(20):205101, 2011.

[192] Hailong Wang, James Kally, Joon Sue Lee, Tao Liu, Houchen Chang, Danielle Reifsnyder Hickey, K Andre Mkhoyan, Mingzhong Wu, Anthony Richardella, and Nitin Samarth. Surface-state-dominated spin-charge current conversion in topological-insulator–ferromagnetic-insulator heterostructures. *Physical review letters*, 117(7):076601, 2016.

[193] Jian-Sheng Wang and Lifa Zhang. Phonon hall thermal conductivity from the green-kubo formula. *Physical Review B*, 80(1):012301, 2009.

[194] Xiaolin Wang, Yi Du, Shixue Dou, and Chao Zhang. Room temperature giant and linear magnetoresistance in topological insulator bi 2 te 3 nanosheets. *Physical Review Letters*, 108(26):266806, 2012.

[195] XS Wang, HW Zhang, and XR Wang. Topological magnonics: A paradigm for spin-wave manipulation and device design. *Physical Review Applied*, 9(2):024029, 2018.

[196] Gian-Carlo Wick. The evaluation of the collision matrix. *Physical review*, 80(2):268, 1950.

[197] AR Wildes, B Roessli, B Lebech, and KW Godfrey. Spin waves and the critical behaviour of the magnetization in. *Journal of Physics: Condensed Matter*, 10(28):6417, 1998.

[198] William Witczak-Krempa, Gang Chen, Yong Baek Kim, and Leon Balents. Correlated quantum phenomena in the strong spin-orbit regime. *Annu. Rev. Condens. Matter Phys.*, 5(1):57–82, 2014.

[199] William Witczak-Krempa and Yong Baek Kim. Topological and magnetic phases of interacting electrons in the pyrochlore iridates. *Physical Review B*, 85(4):045124, 2012.

[200] CH Wong, HJ van Driel, Rakpong Kittinaradorn, HTC Stoof, and RA Duine. Spin caloritronics in noncondensed bose gases. *Physical review letters*, 108(7):075301, 2012.

[201] Stephen M Wu, Wei Zhang, KC Amit, Pavel Borisov, John E Pearson, J Samuel Jiang, David Lederman, Axel Hoffmann, and Anand Bhattacharya. Antiferromagnetic spin seebeck effect. *Physical review letters*, 116(9):097204, 2016.

[202] Cong Xiao and Qian Niu. Conserved current of nonconserved quantities. *arXiv preprint arXiv:2009.12058*, 2020.

[203] Di Xiao, Ming-Che Chang, and Qian Niu. Berry phase effects on electronic properties. *Reviews of modern physics*, 82(3):1959, 2010.

[204] Cenke Xu and Joel E Moore. Stability of the quantum spin hall effect: Effects of interactions, disorder, and z 2 topology. *Physical Review B*, 73(4):045322, 2006.

[205] Su-Yang Xu, Madhab Neupane, Chang Liu, Duming Zhang, Anthony Richardella, L Andrew Wray, Nasser Alidoust, Mats Leandersson, Thiagarajan Balasubramanian, Jaime Sánchez-Barriga, et al. Hedgehog spin texture and berry's phase tuning in a magnetic topological insulator. *Nature Physics*, 8(8):616–622, 2012.

[206] Daiki Yanagishima and Yoshiteru Maeno. Metal-nonmetal changeover in pyrochlore iridates. *Journal of the Physical Society of Japan*, 70(10):2880–2883, 2001.

[207] Bohm-Jung Yang and Yong Baek Kim. Topological insulators and metal-insulator transition in the pyrochlore iridates. *Physical Review B*, 82(8):085111, 2010.

[208] Kai-Yu Yang, Yuan-Ming Lu, and Ying Ran. Quantum hall effects in a weyl semimetal: Possible application in pyrochlore iridates. *Physical Review B*, 84(7):075129, 2011.

[209] Kai-Yu Yang, Yuan-Ming Lu, and Ying Ran. Quantum hall effects in a weyl semimetal: Possible application in pyrochlore iridates. *Phys. Rev. B*, 84:075129, Aug 2011.

[210] Yihao Yang, Zhen Gao, Haoran Xue, Li Zhang, Mengjia He, Zhaoju Yang, Ranjan Singh, Yidong Chong, Baile Zhang, and Hongsheng Chen. Realization of a three-dimensional photonic topological insulator. *Nature*, 565(7741):622–626, 2019.

[211] XZ Yu, Yoshinori Onose, Naoya Kanazawa, Joung Hwan Park, JH Han, Yoshio Matsui, Naoto Nagaosa, and Yoshinori Tokura. Real-space observation of a two-dimensional skyrmion crystal. *Nature*, 465(7300):901–904, 2010.

[212] Emily Z Zhang, Li Ern Chern, and Yong Baek Kim. Topological magnons for thermal hall transport in frustrated magnets with bond-dependent interactions. *Physical Review B*, 103(17):174402, 2021.

[213] Hantao Zhang and Ran Cheng. Magnon thermal edelstein effect detected by inverse spin hall effect. *Applied Physics Letters*, 117(22):222402, 2020.

[214] Hongbin Zhang, Kristjan Haule, and David Vanderbilt. Effective j= 1/2 insulating state in ruddlesden-popper iridates: an lda+ dmft study. *Physical review letters*, 111(24):246402, 2013.

[215] Lifa Zhang and Qian Niu. Angular momentum of phonons and the einstein–de haas effect. *Physical Review Letters*, 112(8):085503, 2014.

[216] Lifa Zhang and Qian Niu. Chiral phonons at high-symmetry points in monolayer hexagonal lattices. *Physical review letters*, 115(11):115502,

2015.

[217] Lifa Zhang, Jie Ren, Jian-Sheng Wang, and Baowen Li. Topological nature of the phonon hall effect. *Physical review letters*, 105(22):225901, 2010.

[218] Lifa Zhang, Jie Ren, Jian-Sheng Wang, and Baowen Li. Topological magnon insulator in insulating ferromagnet. *Physical Review B*, 87(14):144101, 2013.

[219] Shu Zhang, Gyungchoon Go, Kyung-Jin Lee, and Se Kwon Kim. Su (3) topology of magnon-phonon hybridization in 2d antiferromagnets. *Physical review letters*, 124(14):147204, 2020.

[220] Xiaoou Zhang, Yinhan Zhang, Satoshi Okamoto, and Di Xiao. Thermal hall effect induced by magnon-phonon interactions. *Physical review letters*, 123(16):167202, 2019.

[221] Xichao Zhang, GP Zhao, Hans Fangohr, J Ping Liu, WX Xia, J Xia, and FJ Morvan. Skyrmion-skyrmion and skyrmion-edge repulsions in skyrmion-based racetrack memory. *Scientific reports*, 5(1):1–6, 2015.

[222] Songrui Zhao, JM Mackie, DE MacLaughlin, OO Bernal, JJ Ishikawa, Y Ohta, and S Nakatsuji. Magnetic transition, long-range order, and moment fluctuations in the pyrochlore iridate eu 2 ir 2 o 7. *Physical Review B*, 83(18):180402, 2011.

[223] Vladimir A Zyuzin and Alexey A Kovalev. Magnon spin nernst effect in antiferromagnets. *Physical review letters*, 117(21):217203, 2016.

Vita

Bowen Ma was born in Anhui, China in November 1994. He received the Bachelor of Science degree with a major in Physics and a minor in Computer Science from the University of Science and Technology of China (USTC) in 2016. Then he was accepted by the physics program in the University of Texas at Austin and started graduate studies there from August, 2016.

Email address: mabowen586@gmail.com

This dissertation was typeset with LaTeX[†] by the author.

[†]LaTeX is a document preparation system developed by Leslie Lamport as a special version of Donald Knuth's TeX Program.